STUDIES OF THE DYNAMICS OF ION_MOLECULE COLLISIONS USING CROSS_BEAM TECHNIQUE

SUBMITTED BY

ISAM AHMED ABBAS

FOR THE DEGREE OF

DOCTOR OF PHILOSOPHY

UNIVERSITY OF EDINBURGH

MARCH, 1989.

ABSTRACT

The work presented in this thesis involved assembling and testing an apparatus designed to observe photon_scattered ion coincidences in crossed beam arrangement. The crossed beams technique has been used to study the scattering of a fast atomic ion of helium (He^+) by argon gas atoms. The results are reported for collision energies between 100_900eV. The data of reduced cross sections show a pure elastic process at energies 100eV and 200eV. At higher energies there is a region of pure elastic process at small angles but at large angles there is a small inelastic component.

The reduced cross section at 600eV is in good agreement with the data extracted from Barat et al(1970)[62] especially in the region of pure elastic scattering (small angles). The deflection function and repulsive potential show reasonable agreement with the deflection function and repulsive potential obtained by processing the data of Barat et al(1970) in the same way that our data were processed.

The coincidence measurement was one of the main objectives of designing this apparatus. Crossed beams of He^+ on N_2 were set up and the time correlation between the scattered ions of He^+ at angle 2.1° and photons of wavelength 337.1nm emitted from transition of $C\ ^3\pi_u \rightarrow B\ ^3\pi_u$ was recorded. The feasibility calculation and the result obtained at a single scattering angle proves that the required result is not far from reach.

Table of Contents

Chapter 1
INTRODUCTION

1.1 GENERAL REMARKS

Soon after the identification of anode rays as positive charge particles by E.Goldstein[1], in 1886, many experiments were under taken to study the motion of ions in gases, attempting to measure the recombination of positive ions with electrons or negative ions to form neutral atoms or molecules. The velocity of positive ions in all these experiments was indefinite. But despite this, these early experiments marked the beginning of the study of ionic collisions. The first experiments on the collisions of charged particles of definite velocity with atoms were carried out in 1911 by Geiger and Marsden[1]. They were studying the scattering of alpha particles by thin foils, to check the prediction of Rutherford's nuclear model of the atom. Most of the experimental work that followed was concerned with the understanding of the bulk properties of atoms. Ever since, collisions have played a fundamental role in physics and chemistry by providing an insight into interatomic dynamics. This resulted in the development of many experimental techniques[2]. Now adays studying the spectroscopy and scattering of particles emerging from ion_atom or molecule collisions is regarded as a very powerful tool for investigating and extracting a great deal of information about the behaviour and structure of both colliding species.

Among collision processes, many are important (for instance, reactive and charge exchange collisions), because they can be used as probes in studies of aggregates of atoms on surfaces of solids. A simple example is the measurement of the thickness of an adsorbed layer of molecules on a surface referred to as the

substrate. The backscattered ions will have a kinetic energy determined by the mass of the target atom and the thickness of the adsorbed layer. Such a technique has been used to determine the sputtering rate of layers of frozen gases, a quantity of interest in astrophysics. Similarly, it could be used to locate the position of adsorbed atoms on a crystalline lattice or to obtain the depth profile of implanted particles. Also some collision processes play a leading role in the atmosphere, for instance ionisation of the constituents of the atmosphere leading to a plasma of ions and fast electrons and more recently many important types of laser use gases as the working medium and operate through processes involving atomic and electron collisions.

1.2 EARLY THEORETICAL CONCEPT OF COLLISION

the very first experimental work of Hasted[3] on cross section measurements was interpreted in terms of Massey's adiabatic criterion. According to this criterion transitions from one state to another are possible only when the collision time and the transition time are comparable. This criterion is a statement of the Heisenberg uncertainty principle as applied to atomic collisions. If $\Delta t = a / v$, is the time of interaction of the atoms, then in this time the internal (electronic) energy is defined only to within $\Delta\varepsilon \simeq 1/\Delta t$. Transitions to states having energies within this range of energy of the initial state may occur with a high probability, but the transitions to other states will be unlikely. Thus from the above, one gets a condition, according to which transitions are improbable unless,

$$a \, . \, \Delta\varepsilon/v \ll 1$$

Here $\Delta\epsilon$ is the separation between the energy states measured in units of frequency, a is an arbitrary interaction distance and v is the relative velocity of the colliding atoms. Hasted[3] used asymptotic atomic energies to calculate $\Delta\epsilon$. Although he successfully accounted for a number of observations this way, such a usage is not always appropriate, because the energies of electronic states can change substantially with internuclear distance, and two states that have quite different energies at infinite separations may become degenerate at finite separation.

1.3 GENERAL CONSIDERATIONS

A single collision between a positive ion and an atom or molecule, considering both collision partners in their ground states, can be described as follows. Let X^i be the ionic particle of charge i and Y be the neutral particle. The interaction between the two partners can be represented by:

$$X^{i+} + Y \rightarrow X^{j+} + Y^{k+} + (j+k-i)e^-$$

The cross section of these processes usually denoted by σ_{ij} where i represents the initial charge of the incident ion and j represents the final charge after collision.

Generally there are many processes which could occur between positive ions and neutral atoms or molecules. These processes are summarized in table_I_. In this table both members taking part in the collision belong to a different species; these type of interactions are called "asymmetric interactions". In the case where both ion beam and target gas are from the same species, then the interaction is

TABLE -I-

PROCESS	TYPE OF COLLISION
$X^+ + Y \longrightarrow X + Y^+$	CHARGE TRANSFER (electron capture)
$X^+ + Y \longrightarrow X^+ + Y^+ + e^-$	IONISATION
$X^+ + Y \longrightarrow X^{++} + Y + e^-$	IONISATION
$X^+ + Y \longrightarrow X^- + Y^{++}$	ATTACHMENT
$X^+ + Y \longrightarrow X^+ + Y^*$	EXCITATION
$X^+ + Y \longrightarrow X^{+*} + Y$	EXCITATION
$X^+ + YZ \longrightarrow X^+ + Y + Z$	DISSOCIATION
$X^+ + YZ \longrightarrow (XY)^+ + Z$	REARRANGEMENT
$\longrightarrow (XZ)^+ + Y$	REARRANGEMENT

called "symmetric charge transfer". symbolically represented by:

$$X^{i+} + X \rightarrow X + X^{i+}$$

The results reported in chapters 5 and 6 of this thesis were obtained from the apparatus which is shown in fig(1.1), and describe in some details in chapters 2,3 and 4 designed to investigate the dynamics of the collisions between atomic ions and various gas targets. A computer program designed to simulate ion lens system was written from a computer programs package called Simion PC/PS2 version 3.1 .It was applied to find the optimum voltages which helped to cure beam instability.

Chapter 5 is concerned with differential cross sections, measured for the collision system $He^{+}\rightarrow$ Ar. The reason for performing this experiment are twofold. Firstly, much experimental work has been done on this system, for example Smith et al[54,56], Barat et al[62] and Lane et al[55]. However, they have left a gap for energies between 600_900eV. Secondly, because this apparatus was newly assembled, this thesis being the first full description of the apparatus, the need was to choose an experimental system about which information already existed, to check and calibrate our apparatus.

The data collected from the $He^{+}\rightarrow$ Ar system took the form of scattering intensities measured at scattering angles from 0_5° and at collision energies between 100_900eV. The calculated values of reduced angle and reduced cross section were compared with the experimental values of Barat et al(1970)[62]. The agreement was good at the region of pure elastic scattering (small scattering angles), as shown in fig(5.10)_chapter 5. The data of Barat were

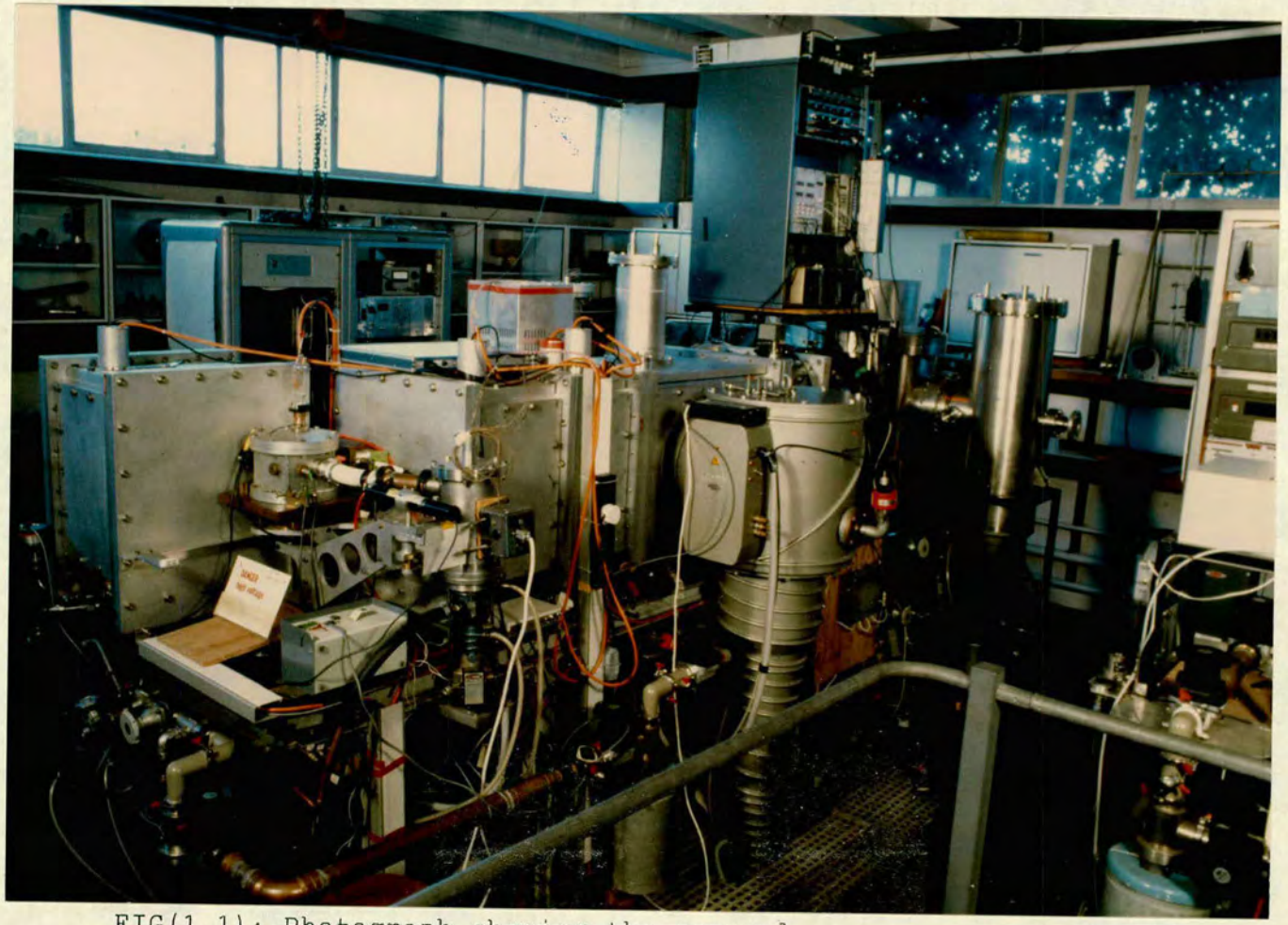

FIG(1.1): Photograph showing the general view of the apparatus.

processed to calculate the deflection function and impact parameter following the same method used in processing our data, and compared with our data as shown in fig(5.11).The agreement was reasonable at large impact parameter, but as b(τ) decreases the drift between the compared values increases. The interaction potential for Barat was also calculated and compared with our potential. The comparison showed a similar behaviour of the deflection function against the impact parameter as shown in fig(5.12).

The correlation in time between ion_photon pairs in what is commonly called "the coincidence technique" was one of the main objectives of building this apparatus. The coincidence technique is one of the very recent generation of collision studies. which should provide a new insight into atoms and molecules. Chapter_6_ is concerned with collisions between two crossing beams, a fast atomic ion beam bringing with it sufficient energy into the collision to open a large number of exit channels, and a slow molecular target beam prepared in its ground electronic state. The fluorescence photons are correlated in time with the arrival of the scattered ions at a suitably remote particle detector by a suitably delayed coincidence to identify the pairs which are originated from a specific collision event. The preliminary results shown in this chapter show that the measurement is feasible, especially if we incorporate the full capacity of the multi_angle particle detector which offers 45 angle elements, allowing a greater range of scattering angles to be investigated and the signal/noise ratio to be enhanced.

Chapter 2
EXPERIMENTAL CONSIDERATIONS

2.1 VACUUM SYSTEM

The most important part in any atomic and molecular collision experiment is quite simply the vacuum in which the beam are formed and their collision studied. As a consequence the development of beam experiments has been closely linked to improvements in vacuum technology. The need to produce a substantial number of events in a well defined region of space inevitably results in an apparatus with very substantial pumping and several differentially pumped vacuum chumbers.

The main requirements of the vacuum system are the following:

(1) Since the mean free path is the average distance traversed by molecules between successive intermolecular collisions, there is a need to provide mean free paths long in comparison with beam path length,thus avoiding significant broadening of the beams. Since the mean free path depends on the size of the molecules as given by the formula,

$$\ell = 1/\{2^{1/2} \cdot \pi \cdot n \cdot d^2\}$$

where d represents the molecular diameter and n the number of molecular per cubic centimeter, it is more difficult to achieve the mean free path required in the case of big molecules.

(2) To keep the density of background gas much lower than the density of the target beam.

The vacuum pumping system which is shown in a schematic

diagram fig(2.1), includes five mechanical pumps type ED250 and ISC450 and nine diffusion pumps, the vacuum achieved is of the order 10^{-6}_10^{-7} torr.

The mechanical pumps are required to reduce the pressure in the vacuum system to about 10^{-1}_10^{-2} torr. This operation is commonly termed roughing; at this pressure condition the diffusion pumps can take over, the mechanical pumps duty is to support and maintain the proper discharge pressure conditions for the diffusion pumps at the foreline connection. The whole roughing system is guarded by six pirani gauges fitted in several sensitive locations to help in controlling and monitoring the backing pressure.

In dealing with diffusion pumps three major points need to be kept in mind:

(1) Efficient pumping can only obtain against a small differential of pressure (less than 10^{-2}_10^{-3} torr).

(2) Cold oil is a better solvent for many gases and vapors than hot oil[4]. Accordingly, the condensed oil should be returned to the boiler at the maximum temperature possible. Otherwise, a certain amount of the exhaust gases and vapors dissolve in the condensed oil and cantaminate it.

(3) The amount of oil decomposed in a given time is proportional to the amount of oil present in the boiler[4]. It is best therefore, to have only a shallow layer of oil in the boiler.

The vapor pressure of vacuum pumping oils,such as "Apiezon B",

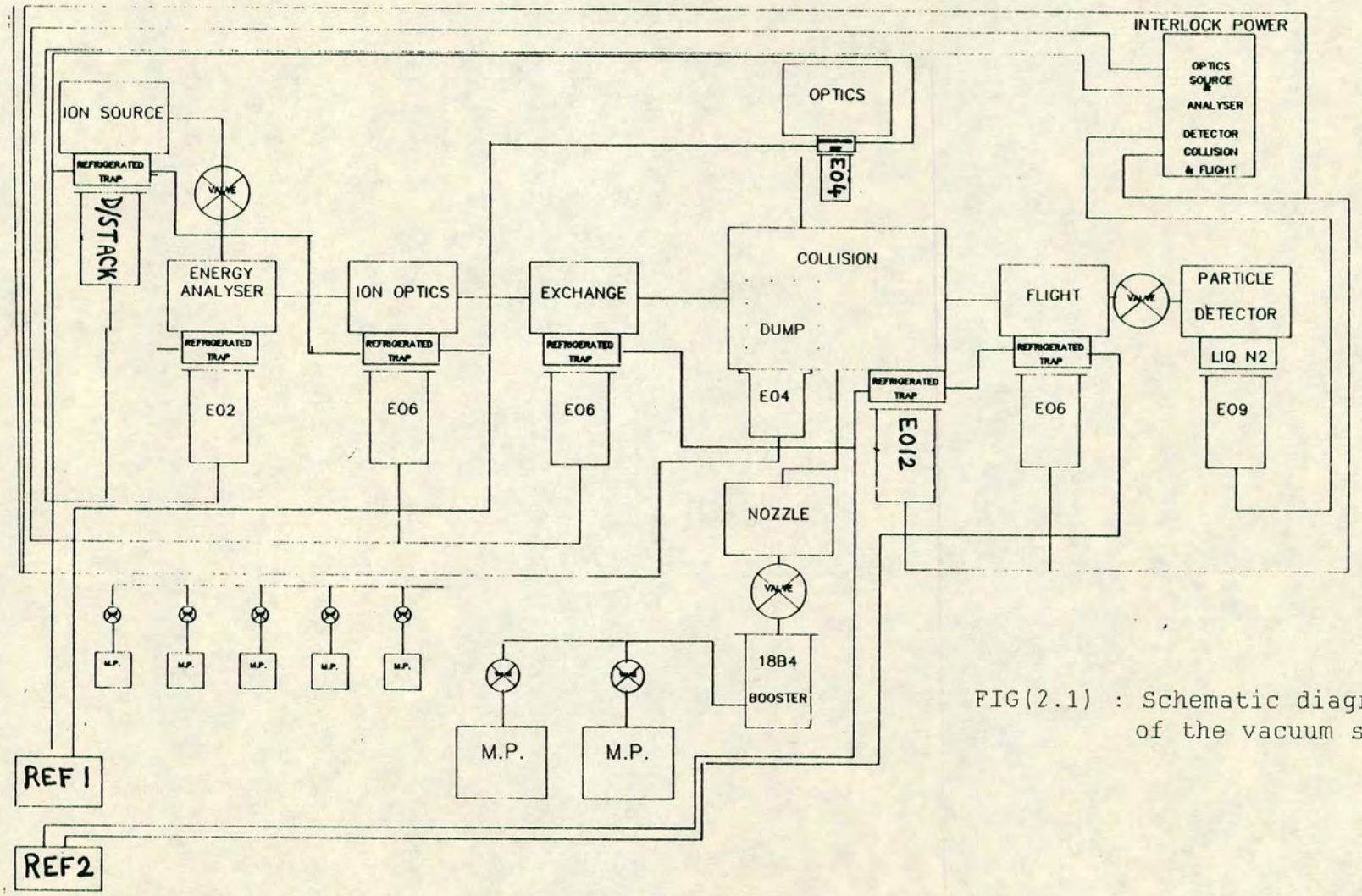

FIG(2.1) : Schematic diagram of the vacuum system.

is very low, but gases produced by thermal decomposition of the oil may give rise to some deterioration of the vacuum and necessitate the use of cold traps.

The liquid nitrogen cold traps are very effective in improving the pumping speed because, liquid nitrogen has normal boiling point 77.4k, therefore the condensibles such as water vapor and pump oils typically from oil charged diffusion pumps and from the roughing pumps, are effectively trapped.

Since our system is large and fairly complex an interlock system, see fig(2.2), was built to protect the apparatus in the events of any failure of some component or of the process underway. The kind of failures the interlock has to deal with are external and internal. The external failures include electric power and water supply,see fig(2.3).The internal failures involve pressure deterioration and excess flow of target gas.

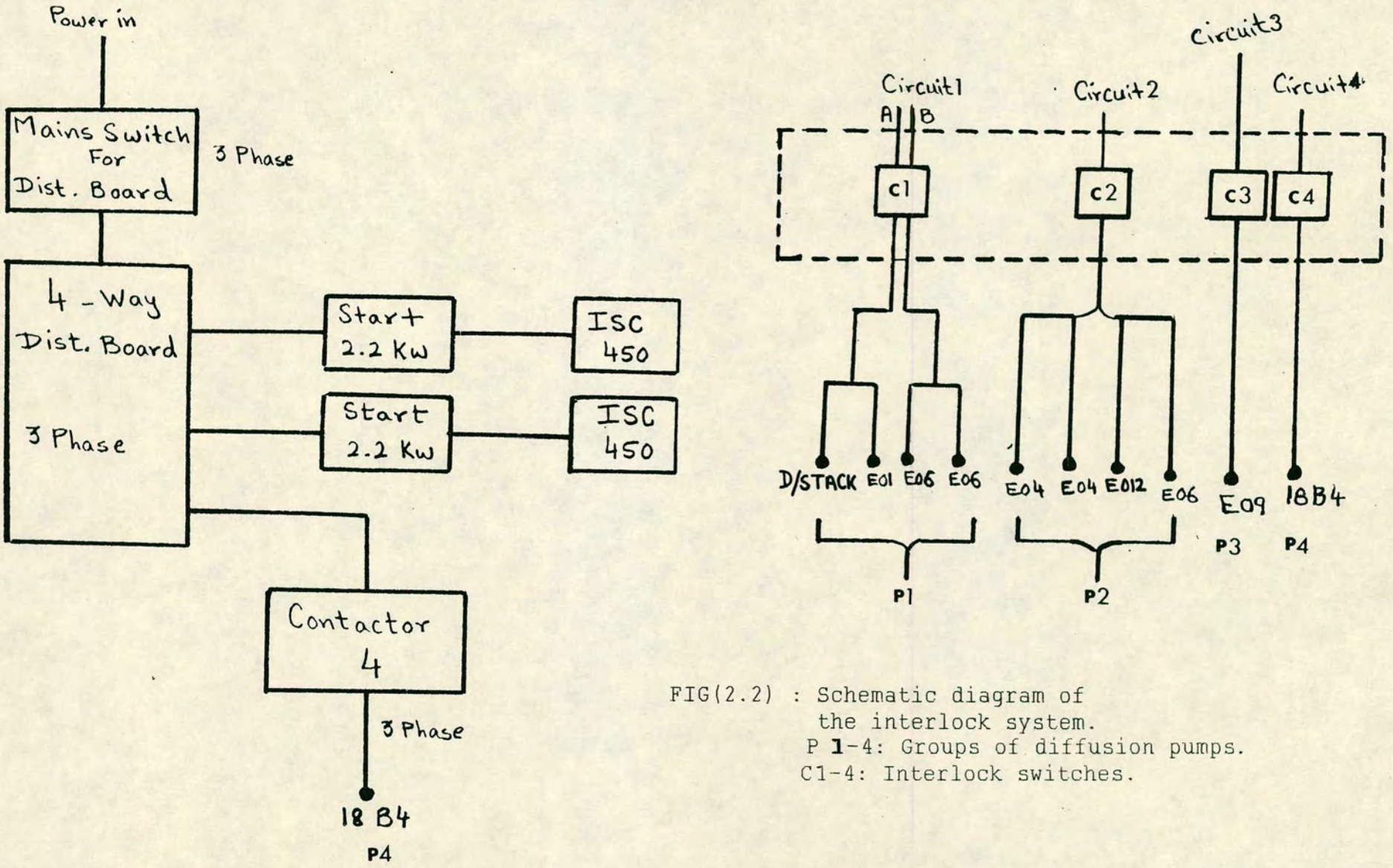

FIG(2.2) : Schematic diagram of the interlock system.
P 1-4: Groups of diffusion pumps.
C1-4: Interlock switches.

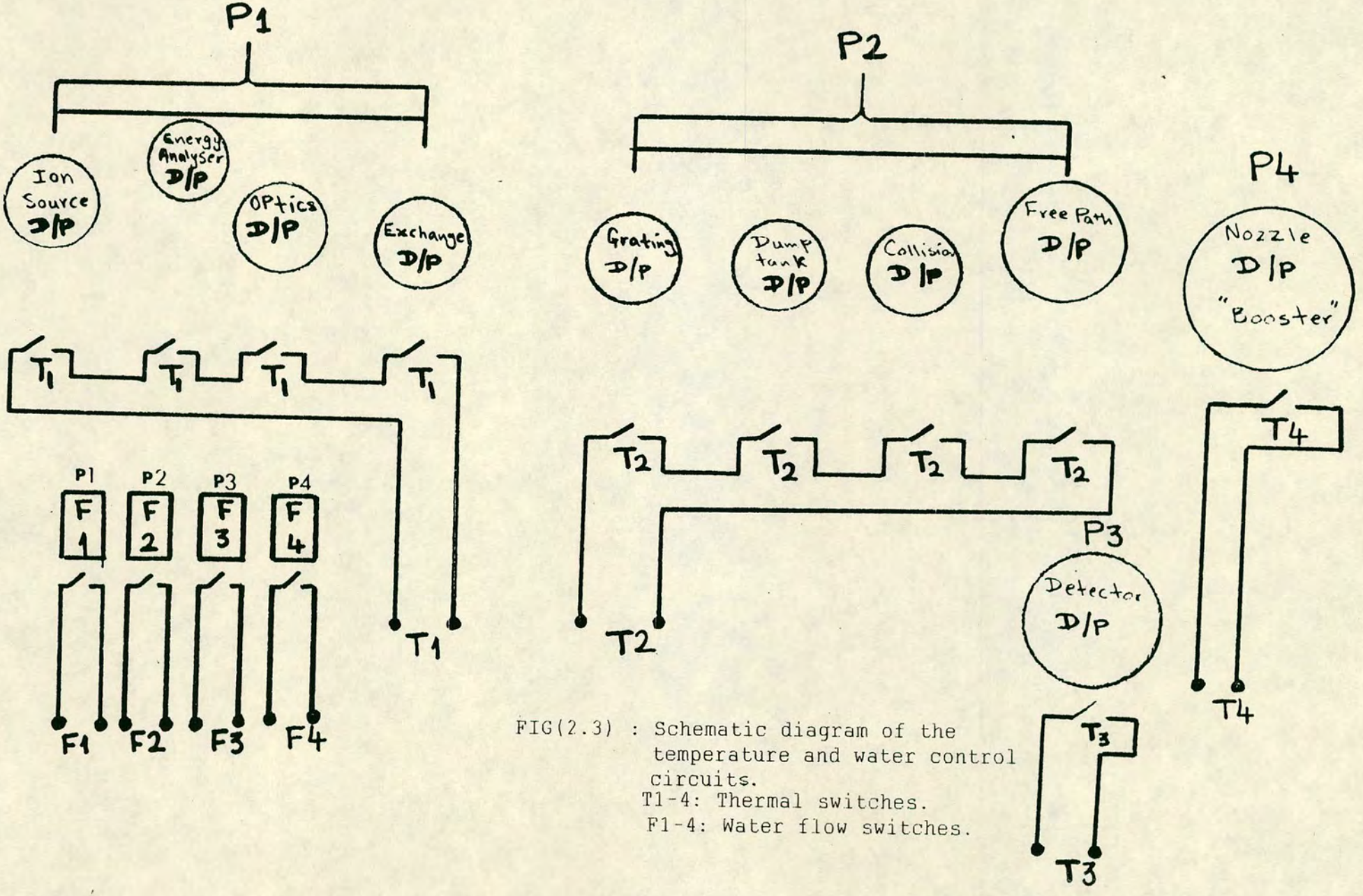

FIG(2.3) : Schematic diagram of the temperature and water control circuits.
T1-4: Thermal switches.
F1-4: Water flow switches.

2.2 ALIGNMENT

The experimental setup described in this work contains many components and each component consists of various elements, which could lead to an experiment being aborted if any element of these components is off center. It is therefore essential to check thoroughly each component and the whole system together before starting the experiment.

Poor alignment leads to losses in the beam intensity due to misfocusing the projectile image. The experimental arrangement, which is shown in fig(2.4), depends on many critical setting, the first and most important being a good alignment of ion source slit, lens electrodes, energy analyser and multi-angle particle detector. This is achieved by aligning each unit separately and then all together.

The alignment was done by using a bench specially designed, to match the aligning arrangement built inside the system. On two sides of the bench (facing each other), two grooves were machined in such away that two horizontal parallel stainless steel bars could be mounted on top of them, allowing each unit to slide freely on the rails. Two alignment pins were made to match the grooves dimension, the pin heads representing the position of the main beam. When they sat on both sides of the unit, a telescope was used to see along the beam path (through the unit), and hence all slits and apertures were aligned exactly. After finishing the external alignment of each component, all experimental component were positioned back in the apparatus. The alignment of the whole system

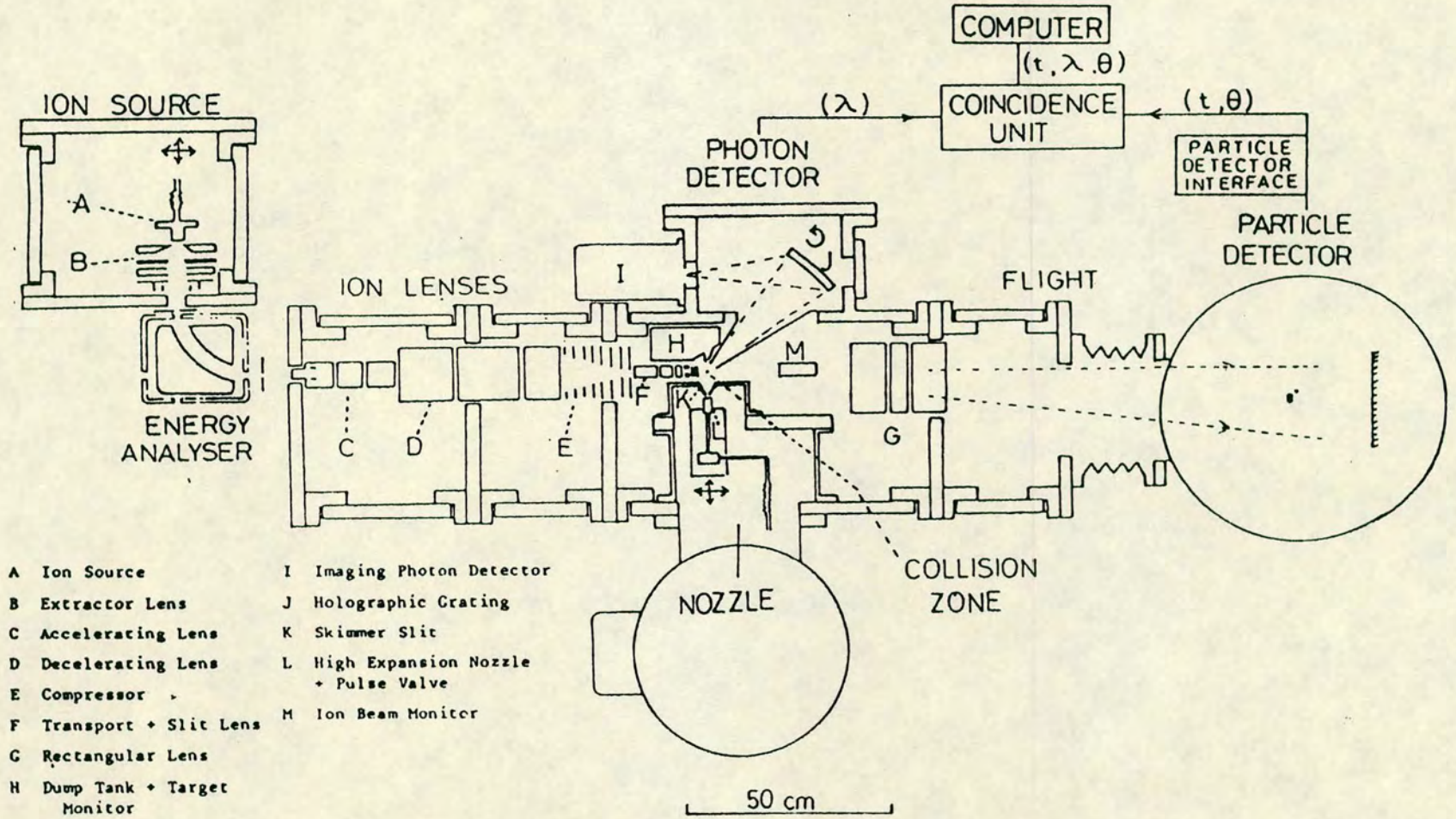

FIG(2.4): Schematic diagram of the experimental setup.

was carried out using, instead of a telescope, a laser beam passing through all the components. This technique has proved to be a most satisfactory method of alignment as it is both accurate and quick to perform.

2.3 ION BEAM PERFORMANCE

The ion beam produced using this apparatus possesses the following characteristics:

1. Monoenergetic and high intensity ion beam.
2. Angular divergence ~0.2°.
3. Energy spread ~0.5 eV.
4. Width of beam at the collision zone 0.3mm and height 10mm.
5. No metastable states or photons in the beam.
6. Good stability and reliability through out the experimental run.

The ion beam was monitored through the apparatus by measuring the ion current at several locations, namely before and after the energy analyser, using a faraday cup of 2mm aperture, at the exit of the accelerating and decelerating lenses, at the collision zone, using an electrode 2mm wide, and at the particle detector. Table_I_ shows the optimum current for a 900 eV beam of He^+.

TABLE - I -

THE COLLECTOR LOCATION	ION BEAM CURRENT μA
ENTRANCE OF THE ENERGY ANALYSER	2 - 2.5
EXIT OF THE ENERGY ANALYSER	1.4 - 1.6
EXIT OF THE ACCELERATING LENS	~1.2
EXIT OF THE DECELERATING LENS	~1.0
AT THE COLLISION ZONE	0.7 - 0.8
AT THE PARTICLE DETECTOR	0.4 - 0.6

Chapter 3
ION BEAM ASSEMBLY LINE

3.1 ION SOURCE

There are four principal type of ion sources[5] :

1. Electron bombardment source.
2. Discharge source.
3. Surface ionization source.
4. Field ionization source.

The discharge source proved very suitable and easy to work with. The properties of this type of ion source are:

1. It provides high beam intensities (2_2.5 μA.).
2. The ion beam can be made stable by regulating the electron emission from the filament and the rate of gas flow, see fig(3.1), as well as by keeping the source power within 1_1.8 watt.
3. The spread of energy is small, because very little kinetic energy is imparted to the ions in the ionizing process.
4. The angular spread of the ion beam is small about 0.1_0.2 °.
5. This type of ion source is ideally suited for gaseous materials[6]

In the past, simple electron impact sources have been used for generating ion beams, but they are limited with respect to beam intensities and source efficiencies. Plasma ion sources are known to provide much higher beam currents due to the larger charge densities in a plasma. However, their energy spreads are commonly thought to be large, with the possible exception of the low_voltage

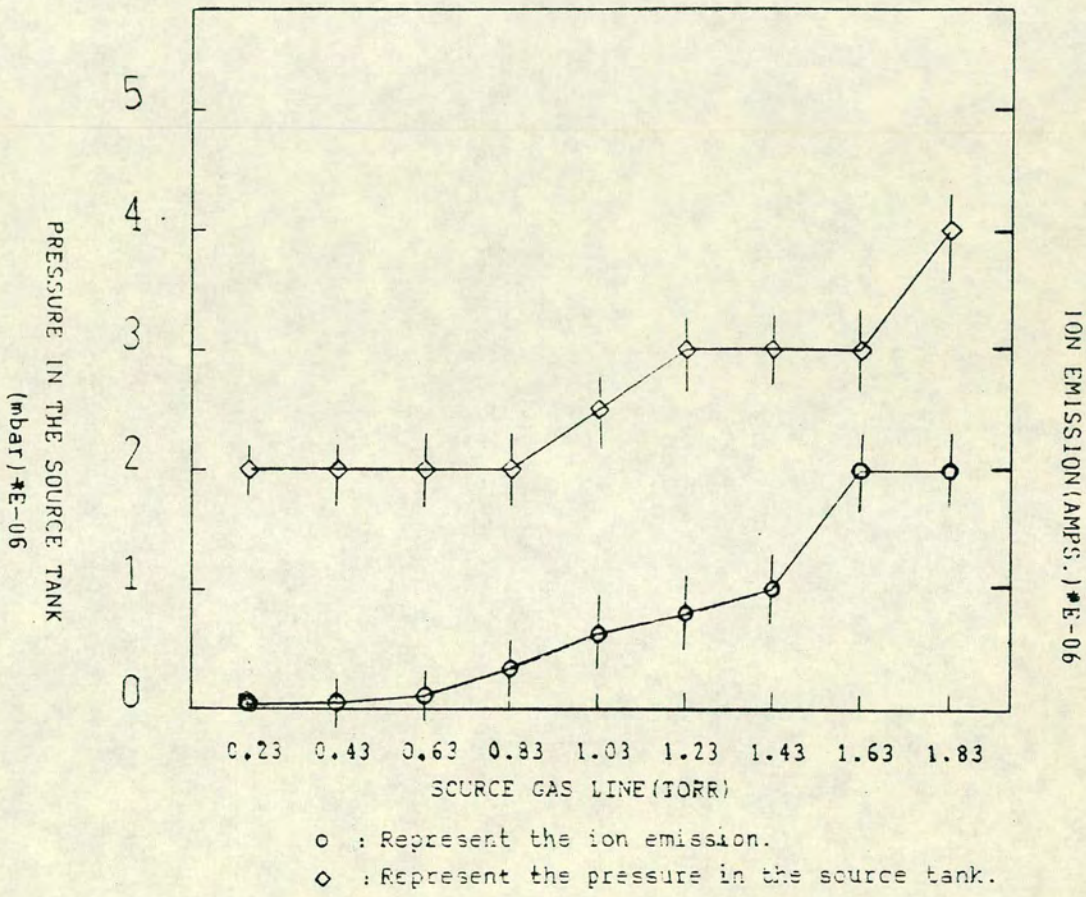
PRESSURE IN THE SOURCE TANK
(mbar)*E-06
ION EMISSION(AMPS.)*E-06
5
4
3
2
1
0
0.23
0.43
0.63
0.83
1.03
1.23
1.43
1.63
1.83
SOURCE GAS LINE(TORR)
o : Represent the ion emission.
◇ : Represent the pressure in the source tank.

FIG(3.1)

arc source[7].

The principle of operation is based on electrons emitted thermonically from the filament, then arranged to pass through a region in which gas is flowing. In passing through the gas filled region (pressure about 0.2_0.8 torr), some of the electrons make inelastic collisions with the gas atoms. A fraction of these collisions are ionising events. These ions can then be extracted by the action of an electric field that is produced by an extraction electrode which causes the ions to migrate to the surface of the extraction slit. The source power (source power= discharge current x anode voltage), was kept all the time within the operating conditions given in table_I_ to ensure that the energy distribution does not broaden.

The technical description of the ion source is illustrated in fig(3.2), and presented in the following main parts:

(i) The anode is a molybdenum cylinder 2.7cm long and 1.75cm outer diameter, which is threaded on one end and has a slit 0.6cm long and 0.1cm width on the other end through which the ions are extracted.

(ii) The filament is made from 0.025cm diameter tungsten wire wound in a tapered spiral and attached to the filament posts of 0.075cm molybdenum wire by means of small spirals of filament wire. The filament to anode distance is 3_4mm.

(iii) A boron nitride filament holder supports both the filament and the anode. The filament leads are fed through 0.075cm holes in

TABLE -I-

SOURCE OPERATING CONDITIONS

SOURCE ELEMENTS	OPTIMUM VALUES
Filament VOLTAGE	4-8 V.
FILAMENT CURRENT	6-8 A.
SOURCE PRESSURE	0.2-0.8 Torr.
DISCHARGE CURRENT	100-200 mA.
ANODE TO EXTRACTION LENS	2-5 mm.
SOURCE CHAMBER PRESSURE	2-4 10 Torr.

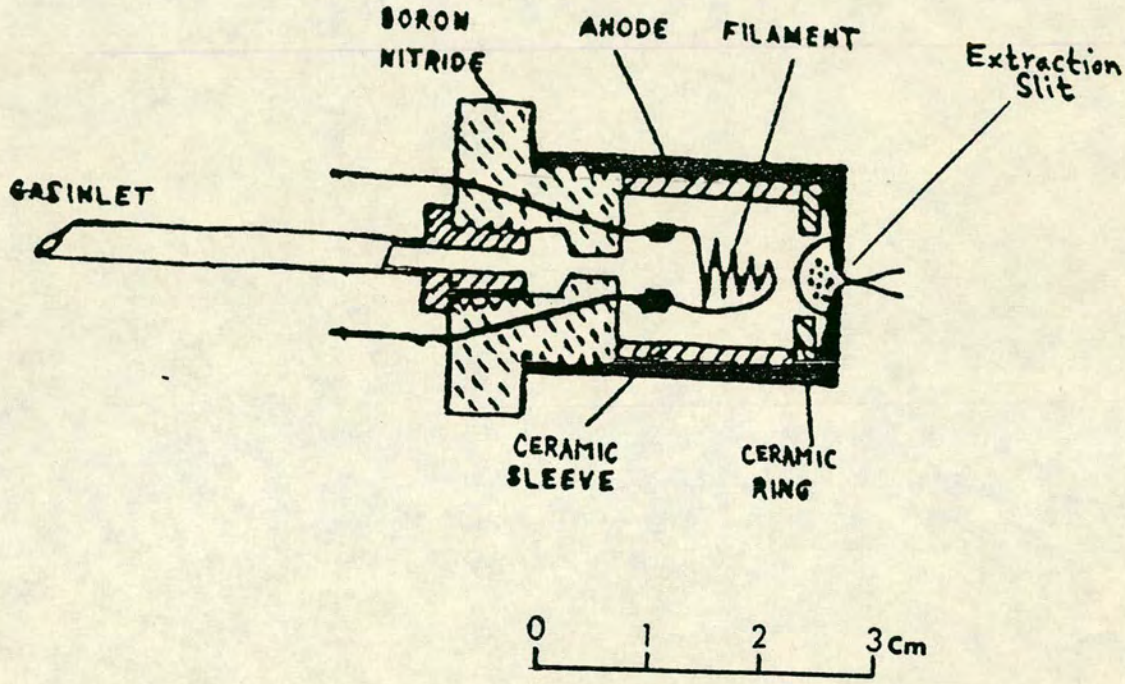

FIG(3.2): Schematic diagram of the ion source assembly.

the boron nitride, while the anode and the stainless steel gas supply tube are screwed on to the boron nitride block to ensure gas_tight connections.

The electrical discharge between the filament and the anode is confined to a small region around the extraction slit by means of a machinable ceramic tube and a washer inside the anode. These inserts insulate the wall of the anode cylinder, leaving only a small portion of the slit at the front end exposed to the cathode.

The ion source and the extraction lens are mounted on separate carriages sliding over two parallel bars, and the source can be moved forward and backward by a stepping motor. In this way the distance between the anode and the extraction lens can be adjusted so that the extraction field strength and the angular spread of the ion beam can be varied.

The temperature of the ion source is maintained below 70c° by water cooling.

It is found that the useful lifetime of the ion source filament is around 300 hours under the filament operation conditions, see fig(3.3).

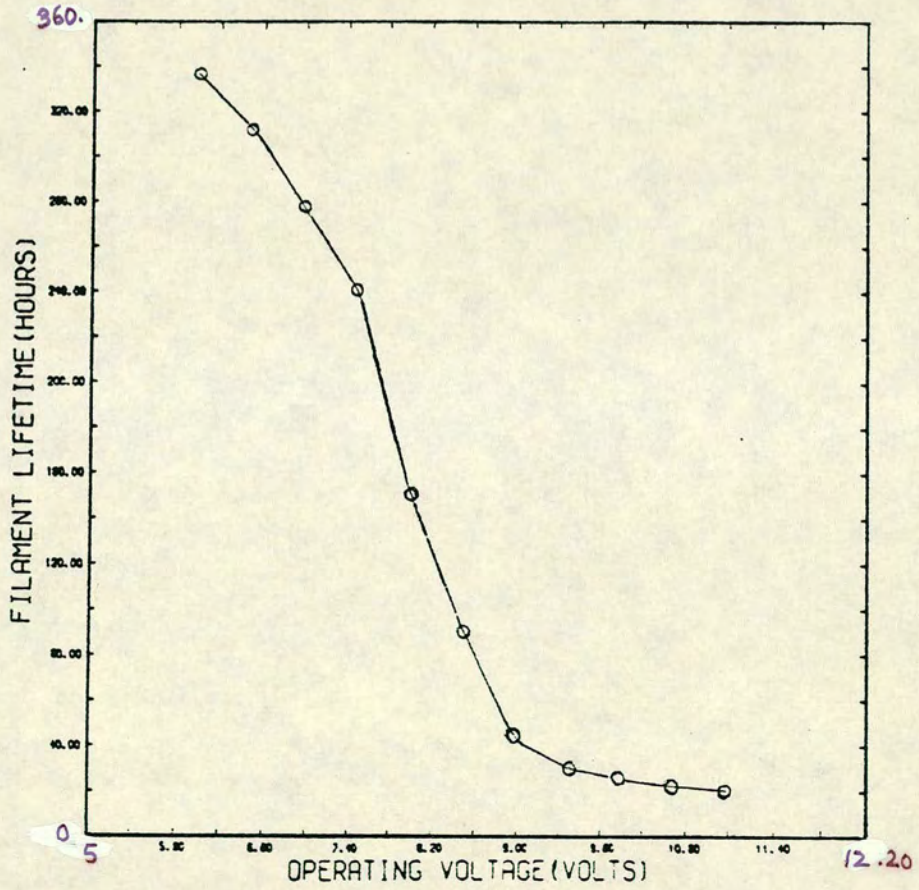

FIG(3.3): Filament lifetime.

3.2 ELECTROSTATIC LENSES

The motion of electrons and ions had been studied in many experimental and theoretical investigation which dealt with the propagation and focusing of beams of ions or electrons. The birth of electron optics may be said to have occurred in 1931_1932 when C.J.Davisson and C.J.Calbick[8,9], and independently E.Bruche and H.Johannson recognized that the action of axially symmetrical electrostatic fields on electron rays was similar to that of a glass lens on light rays. The use of electrostatic lenses for the projection of extended electron images was developed first by E.Bruche and his collaborators (1934), who worked mainly with electrostatic lenses. Up to 1968_1969 electrostatic lenses experienced a rapid development induced by a strong experimental need specially in nuclear, atomic and molecular physics and in electron microscopy. In this work two approaches were used to understand the ions behaviour in the electrostatic field and the performance of the electrostatic lenses. First, the initial designs were developed using the extensive tabulation of Harting and Read[10]. These preliminary results were then later refined using a package of computer programs to calculate the electrostatic potentials and the trajectories in the lens system.

3.2.1 INVESTIGATION OF ION LENS SYSTEM USING A COMPUTER

In an experiment involving the use of ion beams, it is necessary that the behaviour of such particles is fully understood in order to assess the optimum working conditions.

In this experiment the ions are controlled by electrostatic lenses, comprising a series of slits, apertures and cylinders held at certain fixed potentials, which focus the particles to a desired region, whilst at the same time effectively fixing their energy. The theories of geometrical ion optics give a good starting point in studing ionic behaviour, but these theories break down, especially when used in lenses consisting of several electrodes, because these electrodes do not act independently.

Harting and Read[10] method of finding the potential is based on the same method used by C.Weber (1967)[11], in which the potential is expanded in terms of Bessel functions, and the well known relaxation method used by Lanczos (1957)[12,13], which is based on solving the Laplace's equation. There is another method of solution (E.Weber 1950)[14], in which the potential is expanded in terms of Bessel functions, but this seems to have been used in only a small number of cases, namely those in which the boundaries consist of cylinders of the same diameter, with very small gaps between them.

The programs package used in this work is called SIMION PC/PS2 version 3.1 .

SIMION is a lens analysis and design program originally developed by D.C.McGilvery at Latrobe University, Department of Physics and Chemistry, Australia 1977. The SIMION PC/PS2 version, developed at the Idaho National Engineering Laboratory, is an extensively revised version. Version 3.1 is an update of the second major release of SIMION PC/PS2. Extensive algorithm modifications have dramatically improved this version's computational speed and

accuracy.

SIMION PC/PS2 version 3.1, adopted the relaxation method in solving the Laplace's equation to determine the potential distribution. The principle of the so_called relaxation method[15,16,17,18], is by setting boundary conditions, given by the potentials of the electrodes of the lens. Arbitrary potential values are assumed first at all points of a network covering the axial plane between the electrodes. These values are then adjusted systematically and repeatedly to bring them into agreement with the given values of the electrodes.

3.2.2 THEORETICAL CONCEPT OF CALCULATION

The calculation of the potential field is done by solving the Laplace equation:

$$d^2V/dx^2 + d^2V/dy^2 + d^2V/dz^2 = 0 \qquad (3.1)$$

where V is the potential and x,y,z are the cartesian coordinates.

The above equation for an axially symmetric field may be expressed in cylindrical coordinates as:

$$\partial^2V/\partial r^2 + (1/r) \cdot \partial V/\partial r + \partial^2V/\partial z^2 = 0 \qquad (3.2)$$

Where r is the radial distance from the z_axis of a point with a potential V.

For points on the axis, where both r and $\partial V/\partial r$ are equal to zero, using the fact that,

$$L_{r\to 0}(1/r) \cdot \partial V/\partial r = (\partial^2V/\partial r^2)_{r=0} \qquad (3.3)$$

Equation (2) can be written as:

$$2\,\partial^2V/\partial r^2 + \partial^2V/\partial z^2 = 0 \qquad (3.4)$$

Equations (2) & (4) are solved using the relaxation method.

The ion trajectory is calculated from the elementary equations of the motions of charged particles through a potential field V:

$$m\,(d^2x/dt^2) = -e\,(\partial V/\partial x)$$

$$m\,(d^2y/dt^2) = -e\,(\partial V/\partial y)$$

$$m\,(d^2z/dt^2) = -e\,(\partial V/\partial z)$$

where x,y,z are the cartesian coordinates of the position of a particle of charge e and mass m at time t.

Making the transformation into cylindrical coordinates and eliminating the time, the equation of motion becomes,

$$2V(d^2r/dz^2) + [1 + (dr/dz)^2]\,(\partial V/\partial z \,.\, dr/dz - \partial V/\partial r) = 0 \qquad (3.5)$$

This equation is solved for r and dr/dz using a standard fourth order Runge_Kutta integration method[19] with an outomatic step length adjustment.

3.2.3 ION EXTRACTION LENS

The function of this unit were:

1. To extract maximum ion current from the ion source.
2. To focus the ion beam as a narrow slit image on the entrance slit of the analyser.

The unit consists of four electrodes V_0,V_1,V_2, and V_3, see fig(3.4). The first two electrodes V_0,V_1 form a double slit lens. This lens acts as a Pierce gun to form a parallel beam.

The effective source of the ion beam is located at the focal point of this lens, fig(3.5). The geometrical lengths of these two electrodes are measured in terms of two characteristic units of length, the slit height, 30mm, and the separation between the two slits, 1.8mm. Since the lens dimensions are not listed in the Harting and Read tables, only the values of the experimental voltages of V_0 and V_1 plotted against the beam energies, and compared with the computer prediction of the voltage ratio for a beam energy of 600eV, see fig(3.6).

The second two electrodes V_2, V_3 form a double cylindrical aperture lens of equal diameter aperture and having rotational symmetry about the central axis.

The ions inside the lens travelling parallel to the z_axis (transmitted through the slit) , accelerated from the lower potential V_2, to the higher potential V_3, and in passing through the electric field they are also focused to a point making an image of the ion

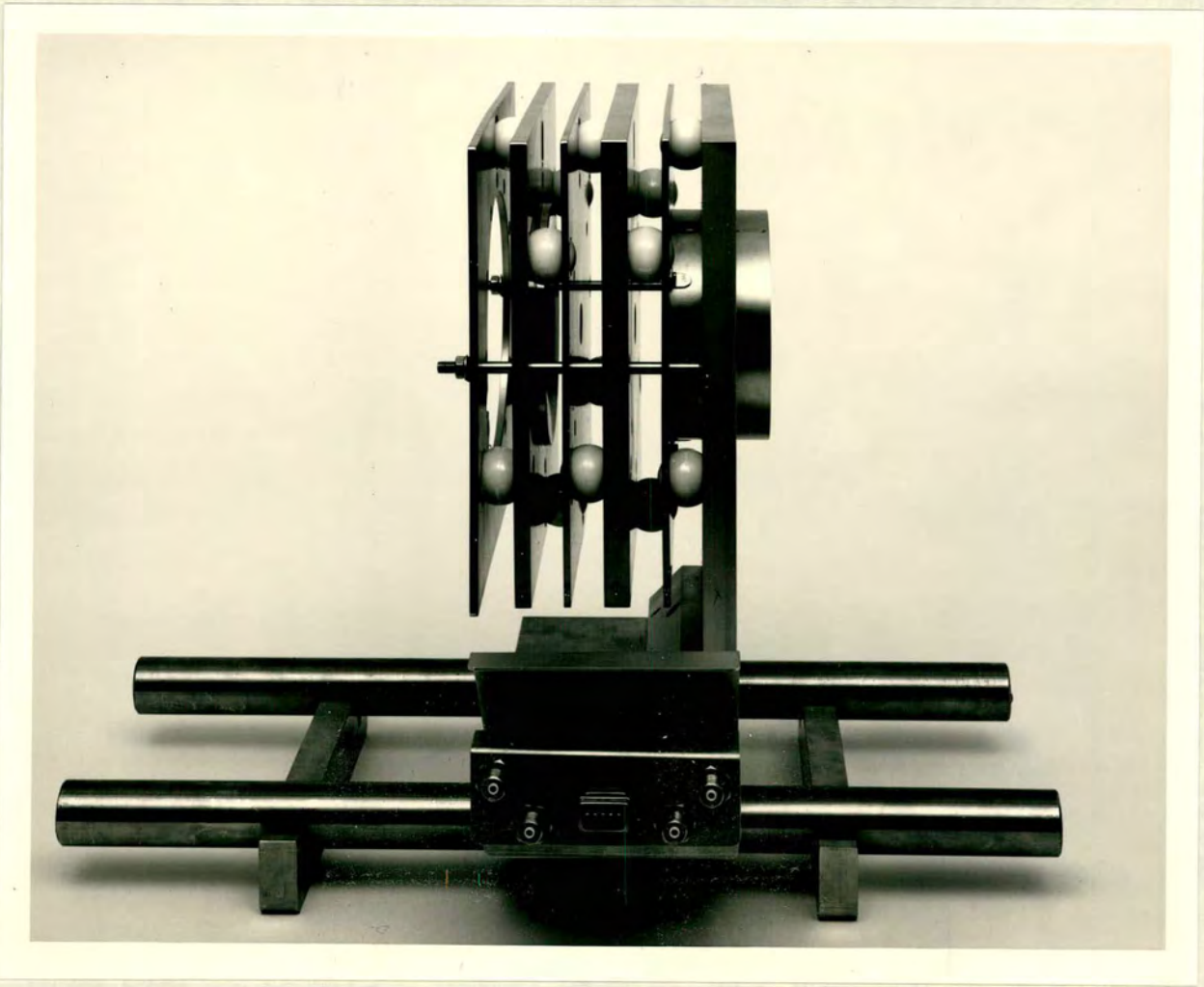

FIG(3.4): Photograph showing the side view
of the ion extraction lens.

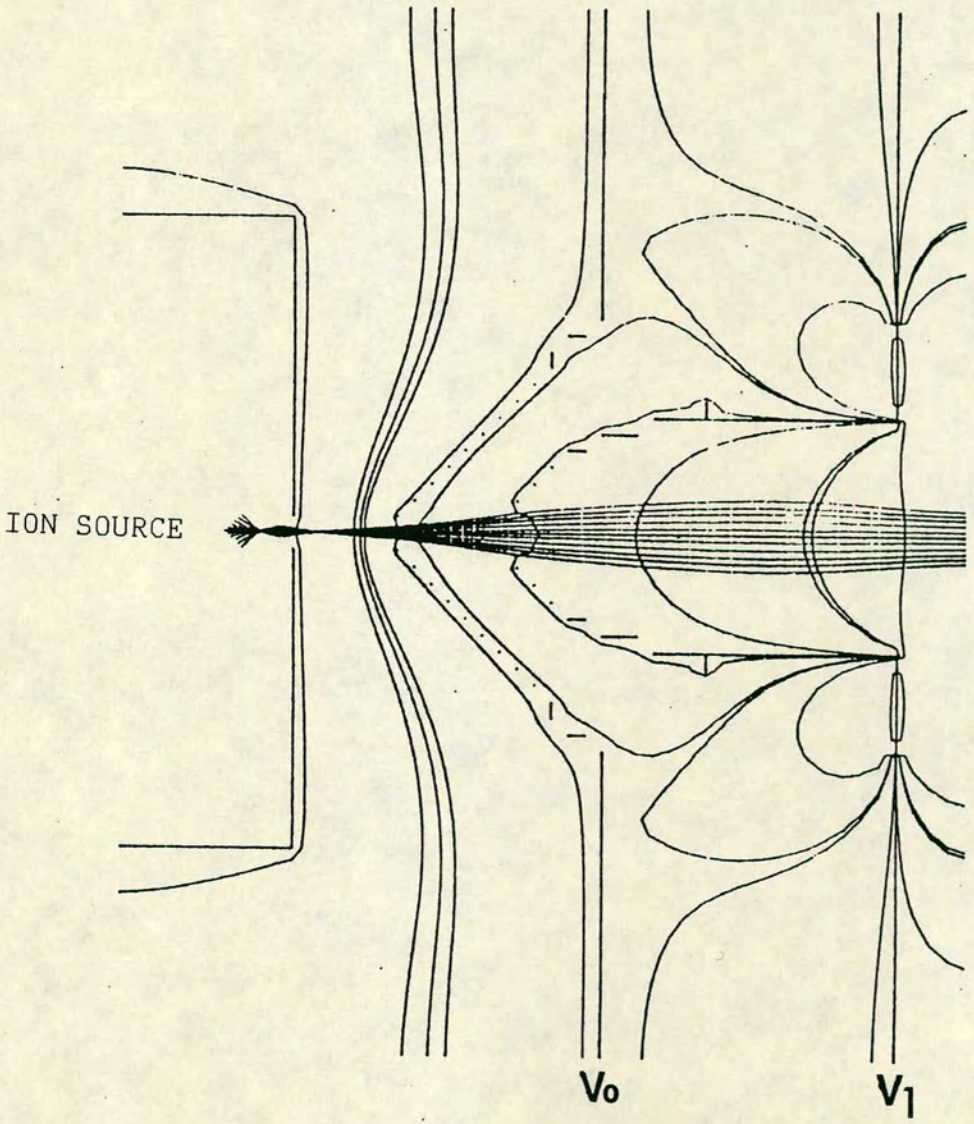

FIG(3.5): Schematic representation of
the object and image formation.

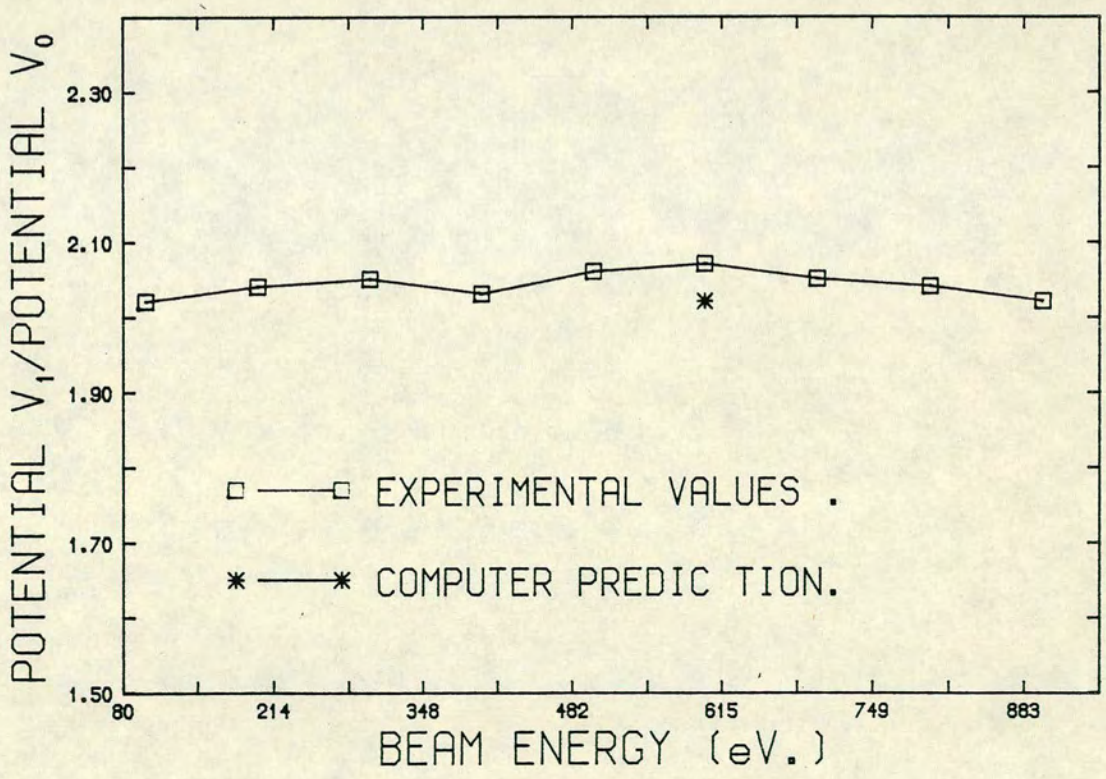
POTENTIAL V_1/POTENTIAL V_0
2.30
2.10
1.90
1.70
1.50
80
214
348
482
615
749
883
EXPERIMENTAL VALUES .
COMPUTER PREDIC TION.
BEAM ENERGY (eV.)

FIG(3.6)

emitter, as shown in fig(3.7).

The characteristic units of length are the aperture diameter,15mm, and the space between the two apertures, 14mm (Harting & Read_ A1.42)[10]. The lens performance represented by the ratios of the voltages V_2 and V_3 taken from Harting and Read, showed good agreement with the experimental voltage ratios and the computer prediction at beam energy 600 eV, fig(3.8).

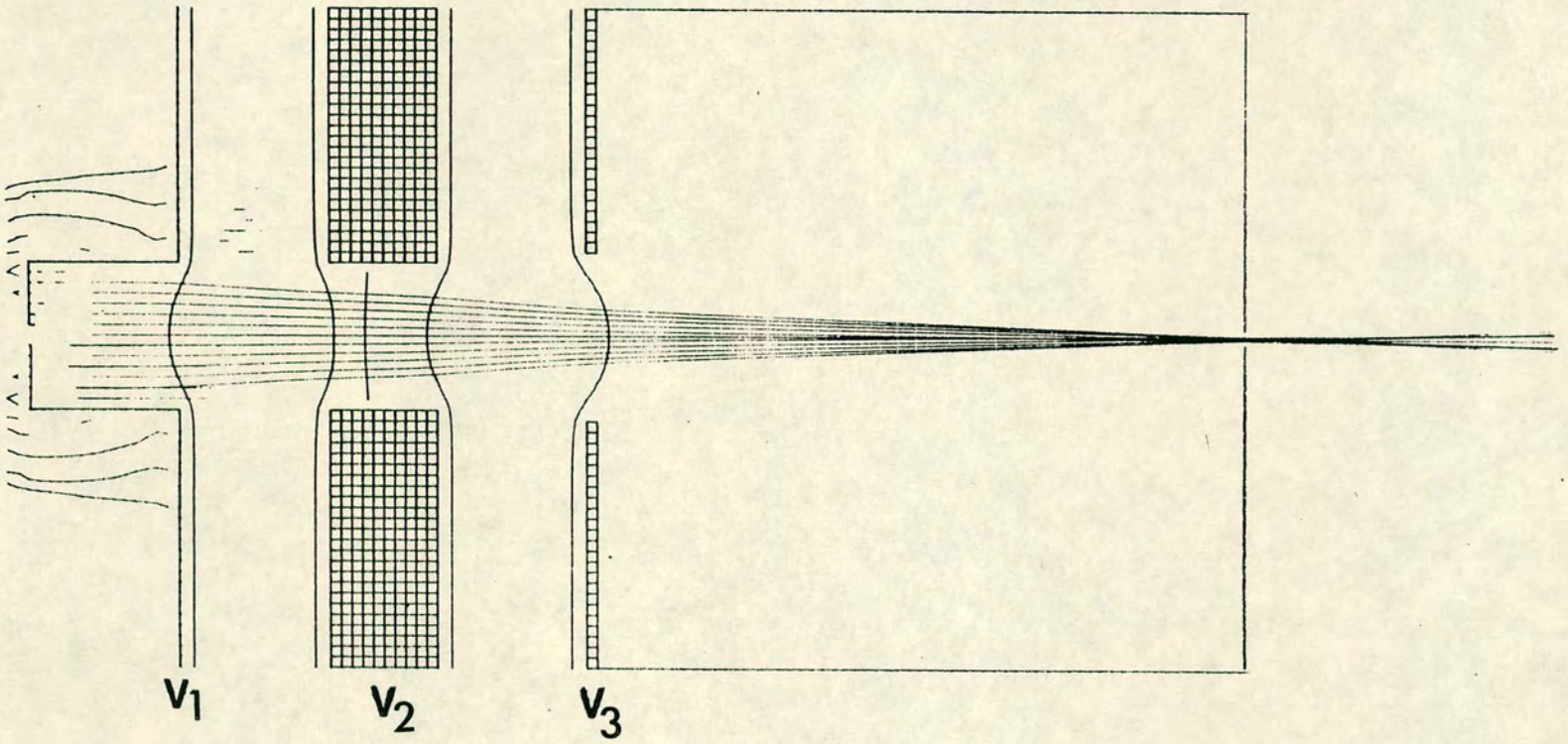

FIG(3.7): Schematic representation of
the object and image formation.

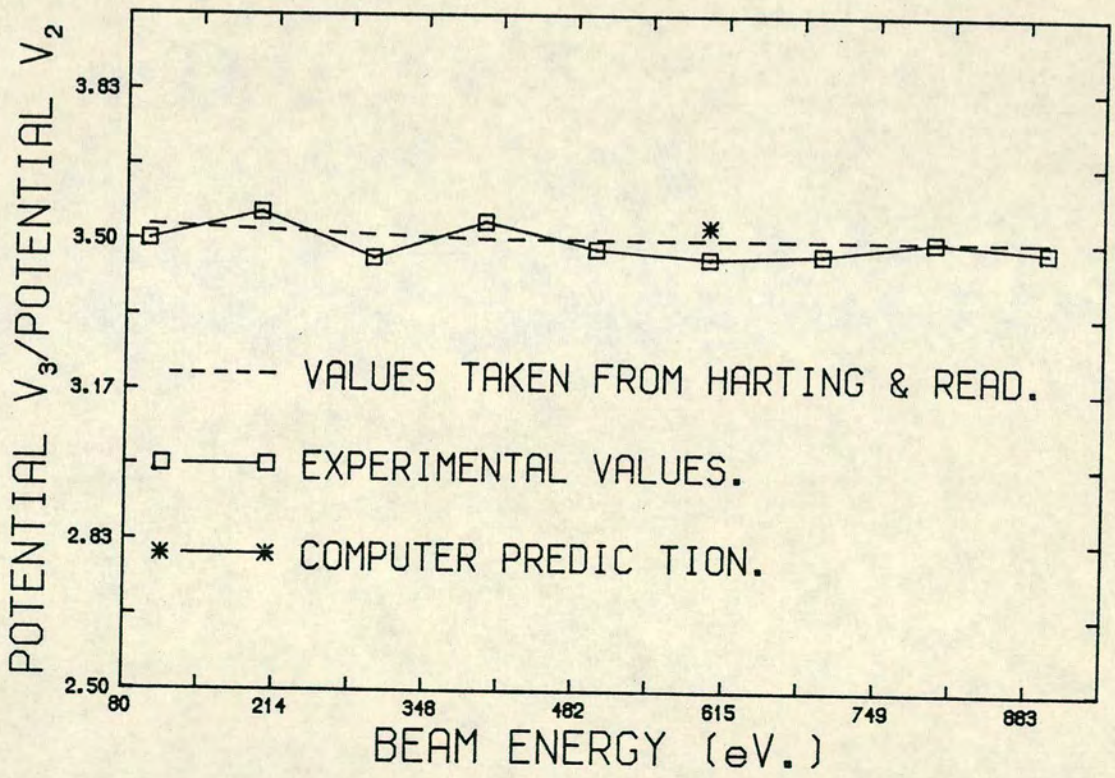
POTENTIAL V_3/POTENTIAL V_2
3.83
3.50
3.17
2.83
2.50
80
214
348
482
615
749
883
BEAM ENERGY (eV.)
----- VALUES TAKEN FROM HARTING & READ.
EXPERIMENTAL VALUES.
COMPUTER PREDIC TION.

FIG(3.8)

3.2.4 ACCELERATING LENS

The function of this lens were:

1. To collect ions from the exit slit (2mm wide), of the spherical energy analyser.
2. To focus these ions on an intermediate slit which serves as an object for the deceleration lens (next lens), and as a differential pumping slit.

The unit consists of three cylindrical electrodes V_3,V_4 and V_5, see fig(3.9), of equal diameter and having rotational symmetry about the central axis.

The triple electrode lens with the central element being of adjustable voltage is also called a saddle_field lens, because the potential distribution becomes saddle_shaped, as shown in the field plot of fig(3.12_case1). The advantage of this type of field is that the focal length can be shortened gradually as the voltage V_4 of the intermediate electrode either increases beyond V_5 or decreases below V_3 (V_3,V_5 are the outer electrodes). Thus the focal length of the lens can be controlled within a very large range by varying V_4.

It is more convenient to take the required geometrical lengths in terms of two characteristic units of length, namely the cylinder diameter, 64mm, and the space between them, 6mm,(Harting and Read_ A3.40).

The exit slit of the energy analyser (the object) is located 216mm from the reference plane (reduced distance 3.4). The image formed

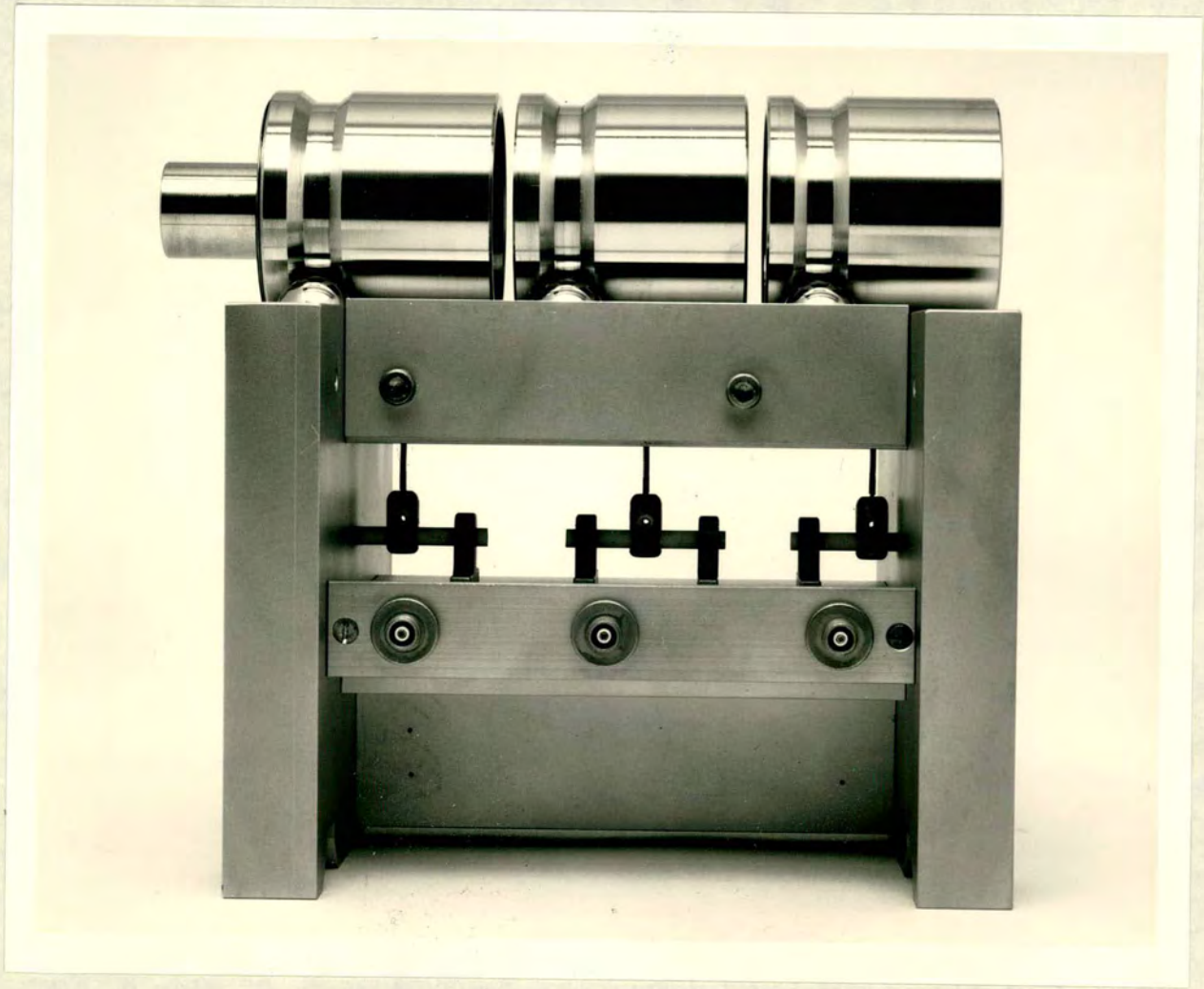

FIG(3.9): Photograph showing the side view of the accelerating lens.

at the differential pumping slit is 106mm from the reference plane (reduced distance 1.6), fig(3.10).

The lens performance represented by the ratios of the voltages V_4 and V_3 taken from Harting and Read showed good agreement with the experimental voltage ratios and the computer prediction for a beam energy of 600eV, see fig(3.11).

The electrodes of this lens as shown in fig(3.9) are mounted on an aluminum bed and supported on six ceramic balls. Each electrode is held down separately to the base of the aluminum bed by a single spring (2mm dia., 25mm long), which acts also as a connection to the voltage supply. The whole carriage slides on two parallel stainless steel bars.

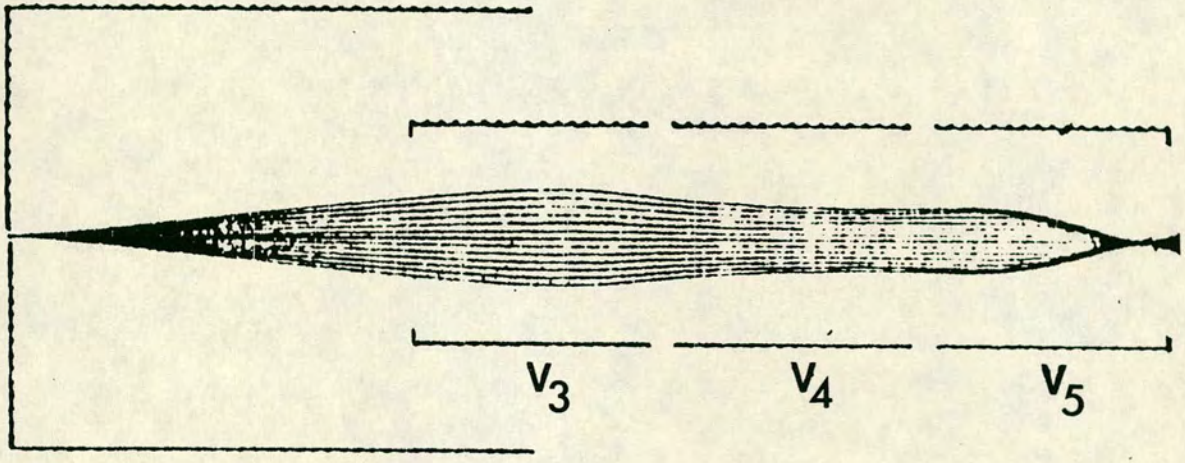

FIG(3.10): Schematic representation of the object and image formation.

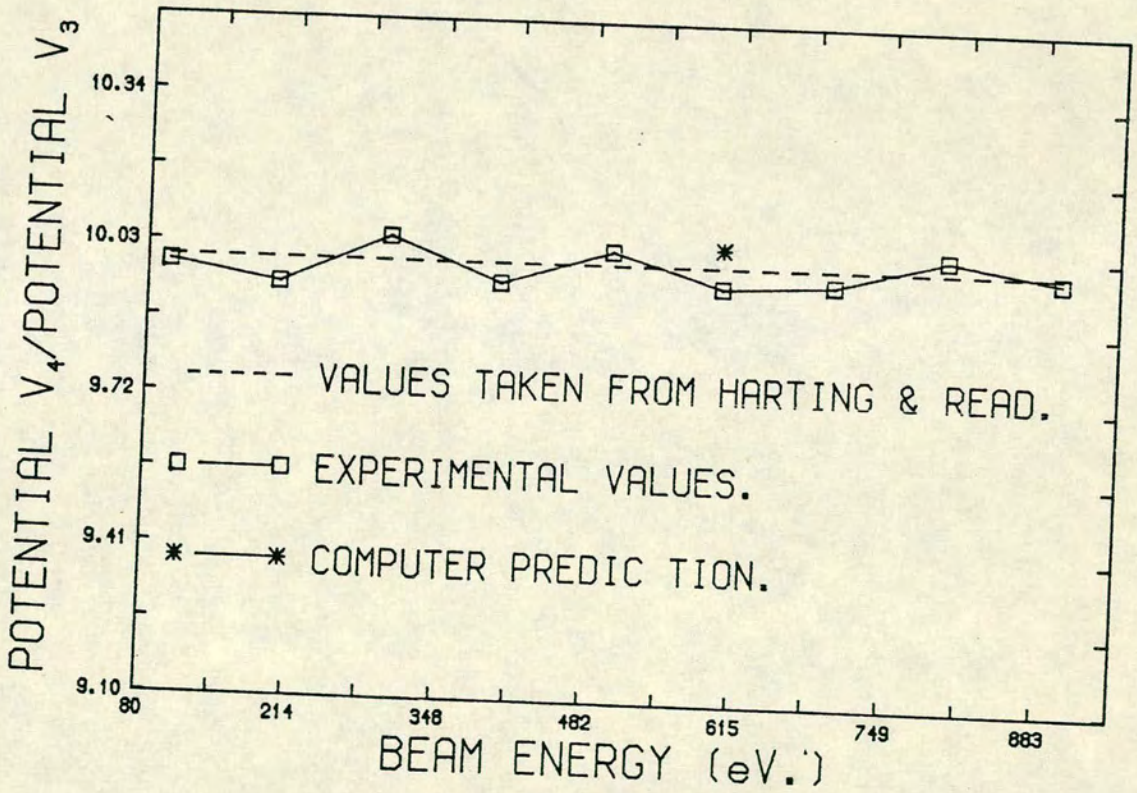
POTENTIAL V_4/POTENTIAL V_3
10.34
10.03
9.72
9.41
9.10
80
214
348
482
615
749
883
BEAM ENERGY (eV.)
----- VALUES TAKEN FROM HARTING & READ.
EXPERIMENTAL VALUES.
COMPUTER PREDIC TION.

FIG(3.11)

3.2.5 DECELERATING LENS

The function of this lens were:

1. To focus the ions on an intermediate slit (2mm wide) which serve as an object for V_8, the einzel lens (next unit), fig(3.12_case1&2)
2. To decelerate the ions coming out of the accelerating lens to focus and form a real image.

This unit consists of three cylindrical electrodes V_5,V_6 and V_7, of diameter larger than the accelerating lens. The characteristic lengths of this lens are taken in terms of the diameter, 135mm, and the space between them, approximately 14mm (Harting & Read_A3.44).

The object is located at the differential pumping slit 270mm from the reference plane (reduced distance 2.0). There are two possible solutions, yielding images at different positions. First, using the intermediate electrode V_6 (3540 volts relative to beam energy 600eV), to form an image beyond V_8(the einzel lens), at approximately 400mm from the reference plane (reduced distance 2.96), fig(3.12_case1). The second solution yield by using a powerful intermediate electrode V_6 (9400 volts relative to beam energy 600eV), to form an image in front of the outer electrode V_7 (at ground potential), approximately 243mm from the reference plane (reduced distance 1.8), fig(3.12_case2). The lens performance was checked by comparing the voltage ratios of V_6 and V_5 taken from Harting and Read with the experimental voltage ratios and with the computed solution for a beam energy of 600eV, as shown in fig(3.13).

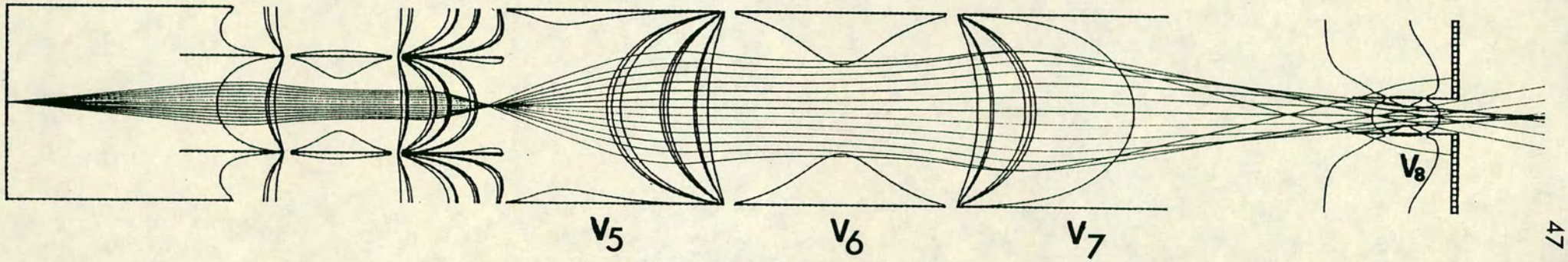

FIG(3.12_case1): Schematic representation of
the object and image formation.

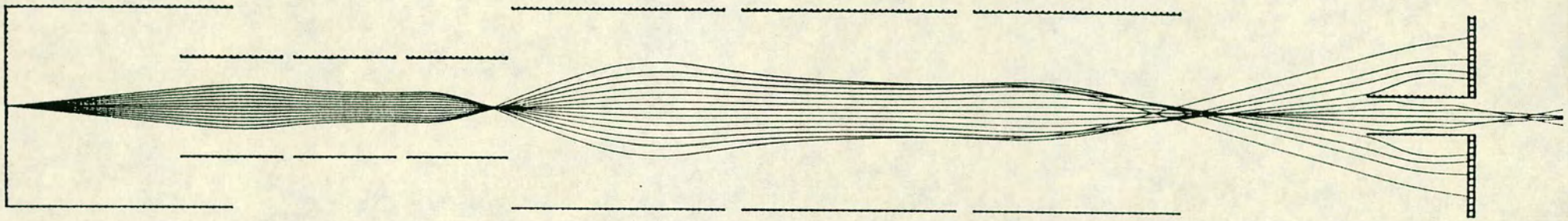

FIG(3.12_case2): Schematic representation of
the object and image formation.

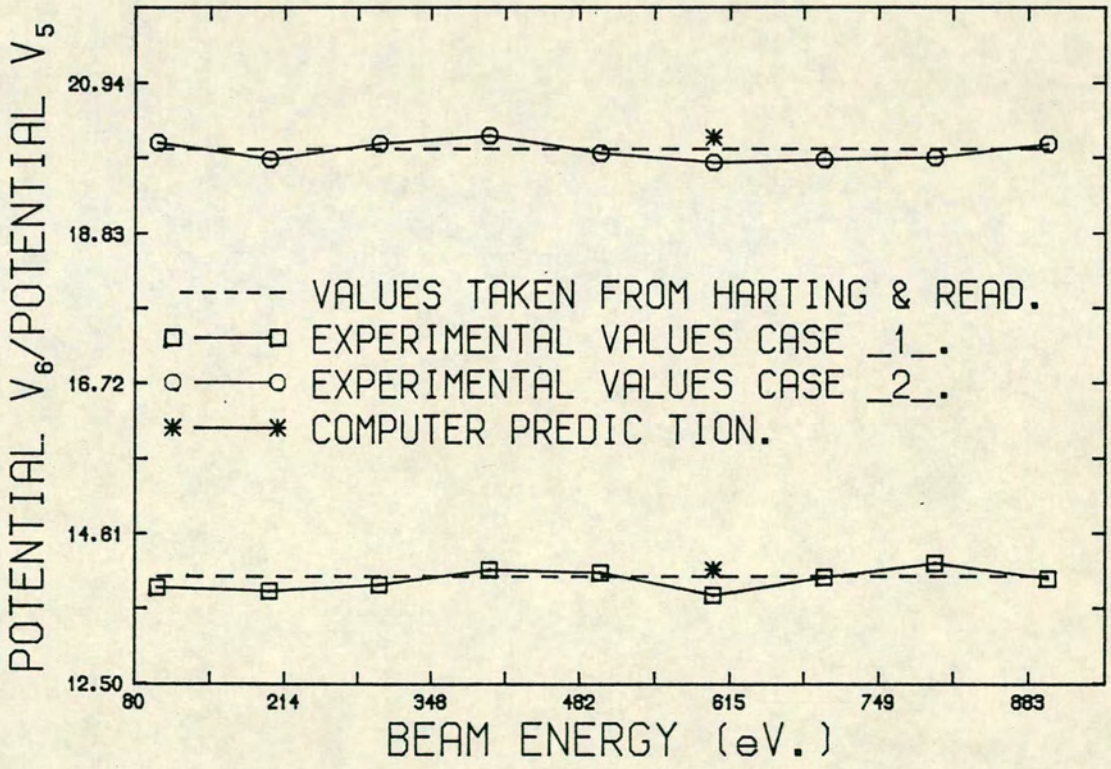
POTENTIAL V_6/POTENTIAL V_5
20.94
18.83
16.72
14.61
12.50
80
214
348
482
615
749
883
BEAM ENERGY (eV.)
----- VALUES TAKEN FROM HARTING & READ.
EXPERIMENTAL VALUES CASE _1_.
EXPERIMENTAL VALUES CASE _2_.
COMPUTER PREDIC TION.

FIG(3.13)

3.2.6 TRANSPORT LENS

The function of this lens was, to adjust the image thrown by the decelerating lens to suit the slit lens V_9 (next unit) by acting as a weakly convergent einzel lens.

Since this lens act as an einzel lens, the ion velocity inside the lens is initially accelerated or decelerated according to the choice of the potential V_8 (the intermediate electrode), but in both cases a converging lens is obtained.

The ions pass through the lens nearer to the z_axis when $V_8-V_{outer}>0$, than when $V_8-V_{outer}<0$; this means that the image position can be adjusted by varying the voltages of V_8.

Figure(3.12_case2), shows the need to apply high voltage on V_8 (1.9 x beam energy, which is equal to 1140 volts for beam energy 600eV), to ensure that the image forms at the focal point of the next unit (V_9). On the other hand figure(3.12_case1), shows how the intermediate electrode V_8 needs less voltage (0.5 x beam energy, which is equal to 300 volts for beam energy 600eV), to focus and converge the ion through it. The case1, found more convenient in respect of the electrode dimensions and lens voltages.

Thiis lens is constructed from three cylindrical electrodes of equal diameter, approximately 20mm, and spacing 2mm (Harting and Read_ A3.25). The first electrode is extended to 64mm and the final electrode is shortened to 8mm.

The lens performance represented by the ratios of the voltages

V_8 and V_{outer} taken from Harting and Read, showed good agreement with the experimental voltage ratios and the computer prediction of beam energy 600eV, as shown in fig(3.14).

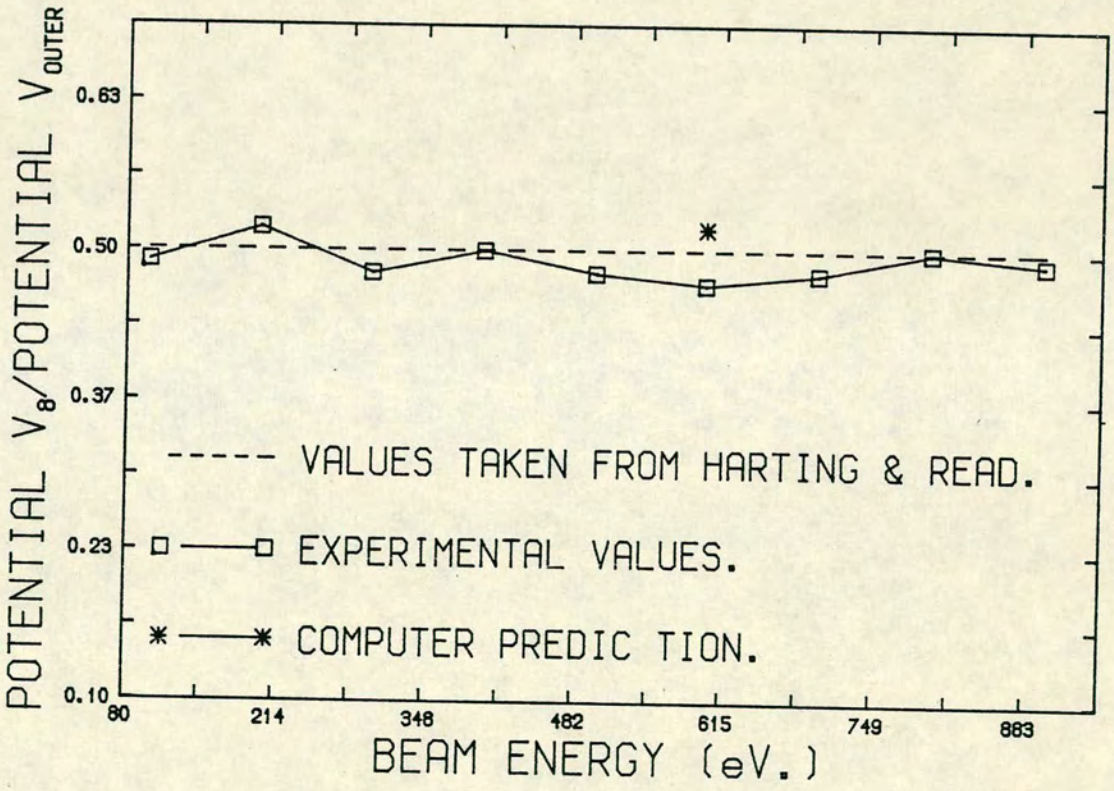
POTENTIAL V_8/POTENTIAL V_{OUTER}
0.63
0.50
0.37
0.23
0.10
80
214
348
482
615
749
883
BEAM ENERGY (eV.)
VALUES TAKEN FROM HARTING & READ.
EXPERIMENTAL VALUES.
COMPUTER PREDIC TION.

FIG(3.14)

3.2.7 SLIT LENS

This lens was designed to produce a parallel beam of ions 0.3mm in width, 10mm tall.

The unit acts as an einzel lens with the two outer electrodes at ground potential. The exit slit of the lens can be adjusted; it was set to 0.7mm, giving an ion beam 0.3mm wide.

The object for this lens is a real image thrown by the decelerating and transport lenses. This object is positioned at the focal point, about 4mm from the reference plane to produce a parallel beam matching the dimensions required of the collision zone, fig(3.15). The voltage required 0.1 x beam energy, which is equal to 60 volts for beam energy 600eV.

The unit was constructed from three rectangular slit electrodes, of equal width, 2mm, and height, 14mm, with reflection symmetry about the central plane.

It is convenient to measure the geometrical lengths of the lens in units of the slit height and the space between them, 2mm (Harting and Read_ A6.28).

The lens performance represented by the ratios of the voltages V_g and V_{outer} taken from Harting and Read showed good agreement with the experimental voltage ratios and the computer prediction at beam energy 600eV, as shown in fig(3.16).

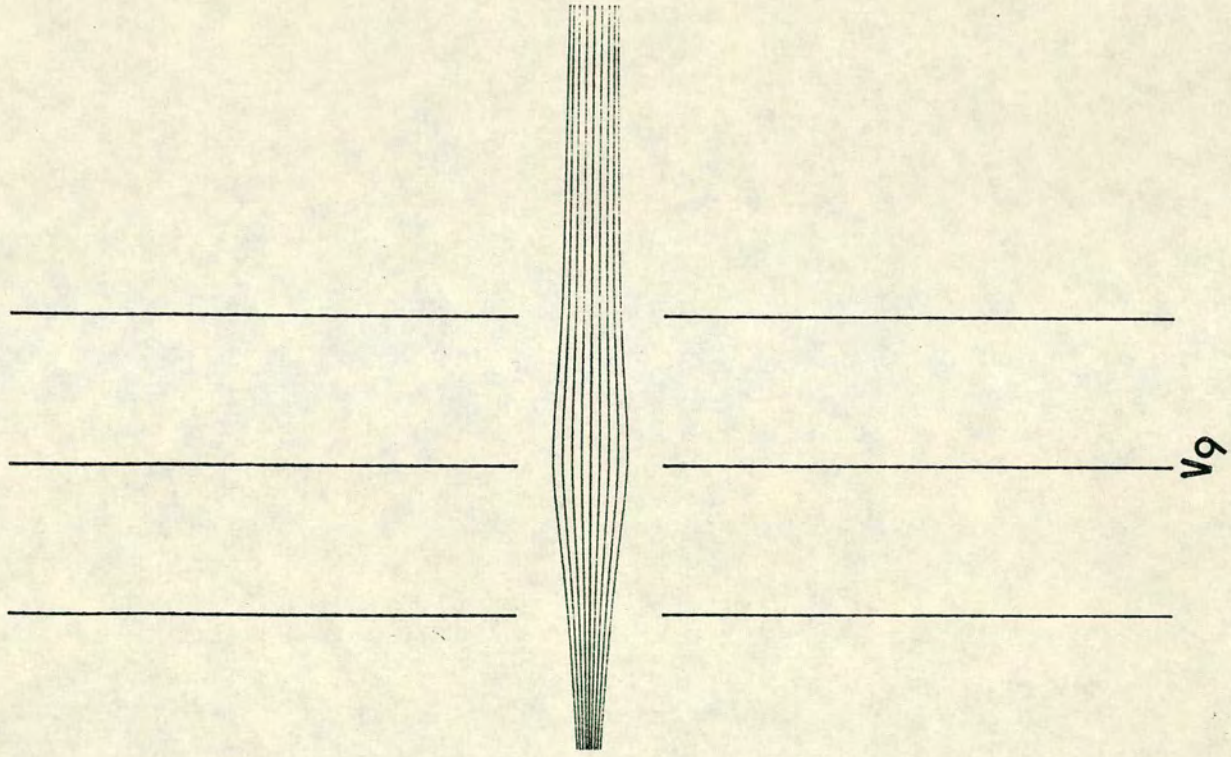

FIG(3.15): Schematic representation of
the object and image formation.

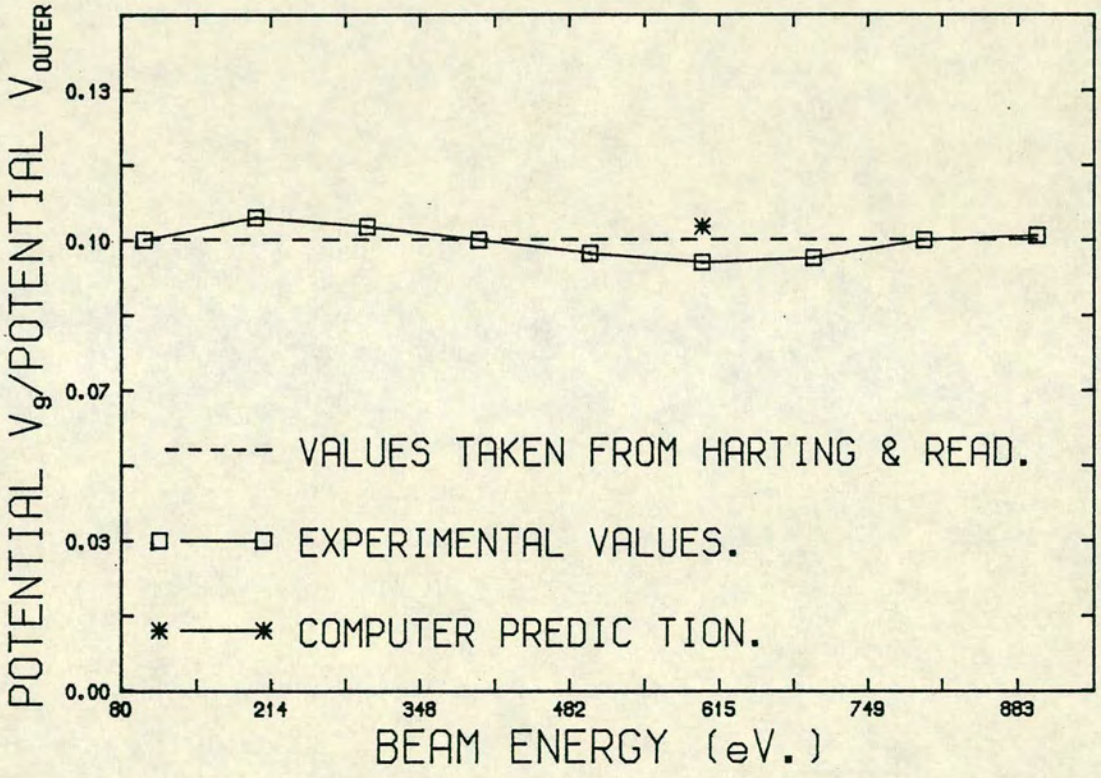
POTENTIAL V_g/POTENTIAL V_{OUTER}
0.13
0.10
0.07
0.03
0.00
80
214
348
482
615
749
883
BEAM ENERGY (eV.)
----- VALUES TAKEN FROM HARTING & READ.
EXPERIMENTAL VALUES.
COMPUTER PREDIC TION.

FIG(3.16)

3.3 SPHERICAL ENERGY ANALYSER

This type of energy analyser has found application in the spectral analysis of ions and electrons over a wide range of energies. Generally the spherical energy analyser has been used to select a beam energy with a narrow energy spread and good intensity, which helped greatly in the measurement of elastic and inelastic scattering in gases leading, for example, to the discovery of resonance effects in both elastic[20,21,22] and inelastic[23,24,25] scattering and new energy levels in the rare gases[26].

The spherical energy analyser has the following advantages:

1. All ions entering into the acceptance solid angle will again be focused after leaving the analyser. This double focusing property is extremely useful in preserving the maximum beam intensity.
2. It prevents any light emitted from the ion source from getting through to the collision region.
3. It defines a beam energy with a resolution of ~0.5eV.

The side view of the analyser is shown in fig(3.17). The two concentric quarter sphere deflectors are made of dural of 10cm in height, with radii 74mm and 96mm for R_1 and R_2 respectively, with mean radius 85mm. The separation between them is 22mm. The inner surfaces of the plates were polished manually using dialap diamond compound, to have no signs of uneven surface or scratches and have a mirror finish. The deflectors fitted inside a tank of aluminum, the whole tank can be adjusted around the vertical axis

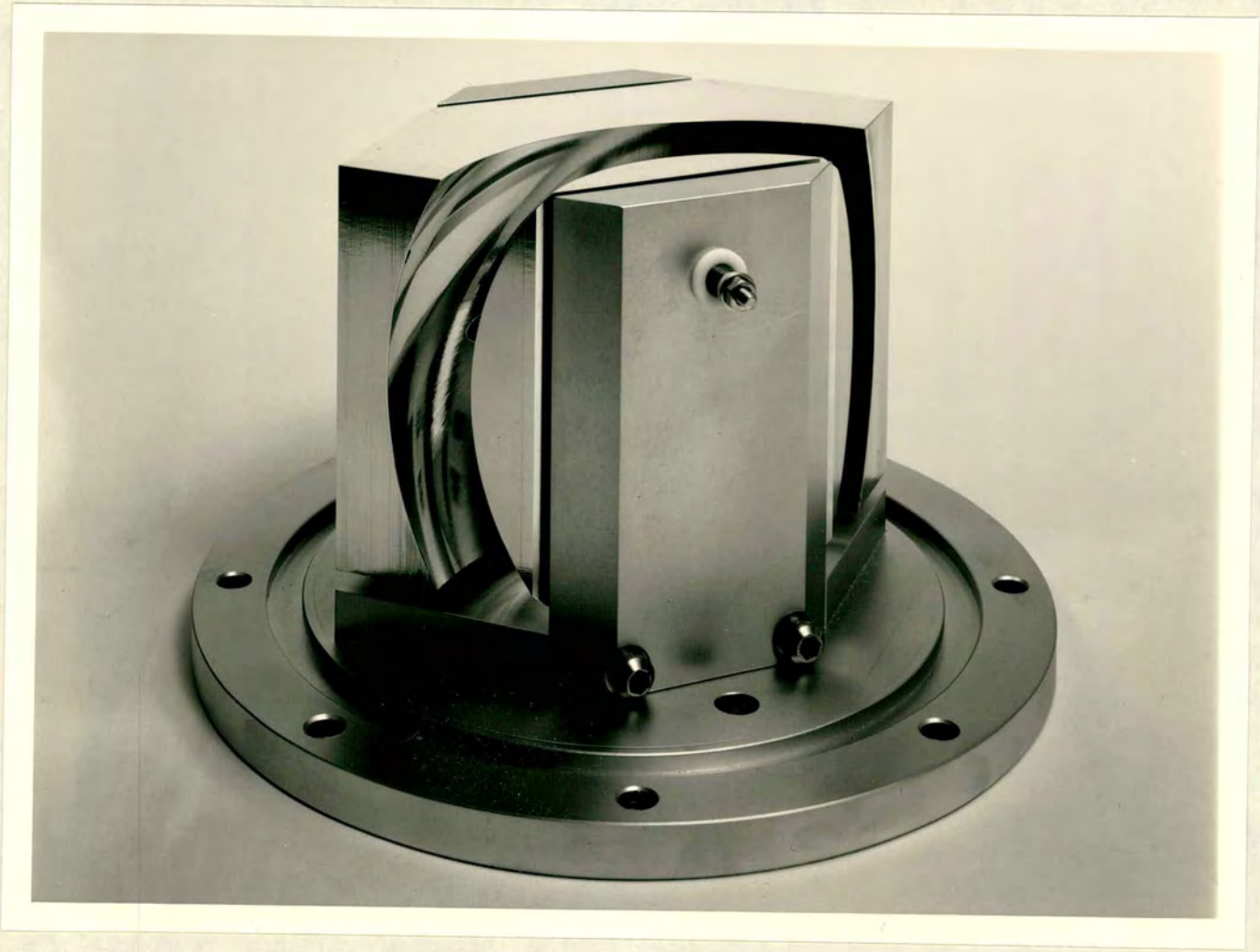

FIG(3.17): Photograph showing the side view of the electrostatic energy analyser.

by means of two aluminum arms and four adjustable screws. The high voltage supply to the deflecting plates is arranged by passing two electrodes through two threaded PTFE plugs, attached to the base of the analyser tank.

The basic theory of electrostatic analysers has been presented by Purcell[27], Rogers[28], Ritchie et al[29], Birkhoff et al[30] and Hubbell et al[31], who have given solutions for the electric field between open spherical segments.

The electrostatic field is produced by the potential difference between the two quarter spheres of radii $R_2 > R_1$. Ions enter the deflectors near the center of the space between the spheres, and exit after being deflected by 90°.

$$E = V_3 + \Delta Q$$

is the kinetic energy in electronvolts of ions which travel in a circular orbit of radius R_0, where ΔQ is the energy spread produced from the ion source, The potential difference V_g between the spheres (the electric field is practically confined to the gap between the plates), is given by[32] :

$$V_g = E\,[(R_2/R_1) - (R_1/R_2)] \qquad (3.6)$$

$$V_g = 0.526\ .E$$

For a normal path lying in the center of the gap,

$$R_0 = (R_1 + R_2)/2$$

Then the potential of the inner sphere is given by :

$$V_{inner} = 2\ .\ E\,[1 - R_0/R_{inner}] \qquad (3.7)$$

The potential of the outer sphere is given by :

$$V_{outer} = 2 \cdot E [1 - R_0/R_{outer}] \qquad (3.8)$$

The energy resolution of the energy analyser is given by :

$$\Delta E/E = (S_1+S_2) / 2 \cdot R_0 \qquad (3.9)$$

Where R_0 is the mean radius of the analyser. Thus, at a given average radius of curvature R_0 for the ion path through the analyser, the resolution is proportional to (S_1+S_2) where S_1,S_2 are the entrance and exit slit_widths respectively. The resolution can be made as good as is compatible with adequate beam intensity simply by adjusting S_1 and S_2.

Chapter 4
DETECTION SYSTEMS

4.1 PHOTON DETECTION SYSTEM

This system was designed and assembled as a tool to study the properties of fluorescence emitted from cross_beam collisions. This study is justified by the fact that it enables us to draw detailed conclusions about the nature of the collision dynamics. The optical system was designed to provide wavelength resolution of about 1nm.

The photon detection system can be divided into the following :

4.1.1 CONCAVE HOLOGRAPHIC GRATING

The complexity of the ruling process has led many people to search for alternative ways of making gratings. In 1927 Michelson suggested the possibility of photographing interference fringes, but was prevented from making gratings in this way by the lack of high_resolution photographic plates. In 1961 Burch and Palmer made grating by photographing interference fringes using a low_pressure mercury lamp as a light source and high_resolution photographic plates as the recording medium. Gratings made in this way were mainly intended for astronomical telescope purposes. The development of holography in the early 1960's, were presented by making transparent replicas of the surface relief pattern in gelatin, in this way efficiencies of up to 30% were achieved. These developments were carried further by several workers(George and Matthews 1966[33], Rigler and Vogl 1966[34], Rosen 1967[35]). The spectroscopic value of these gratings was limited by the granularity of the silver halide photographic process which gave rise to a generally unacceptable level of scattered light. However, in about

1967 Labeyrie[36] in France overcame this problem by using photoresist as the recording medium. Photoresists have higher resolution than photographic emulsions.

4.1.2 RESOLUTION

In our spectroscopic system, radiation enters through a narrow slit, is dispersed, and the spectrum is then brought to a focus. The spectrum consists of a series of displaced images of the entrance slit, one for each wavelength present, and the resolution is the ability to separate closely spaced spectral lines. The resolving power of a grating is defined as:

$$\text{Resolving Power} = \lambda/\Delta\lambda$$

Where $\Delta\lambda$ is the smallest wavelength interval that can be resolved at a wavelength λ, and on the basis of the Rayleigh criterion it may be shown that,

$$\text{Resolving Power} = m \cdot N$$

$$R \cdot P = m \cdot w/d$$

Where m is an order number, N is the total number of grooves, d is the grating period and w is the width of the grating, see table_I_.

Hence $R.P \simeq 222{,}600$

TABLE _I_

CONCAVE HOLOGRAPHIC GRATING CHARACTERISTICS

Grooves per mm.	1484
Dispersion (nm/mm)	2.2
Grating dimension/mm	150
Aperture	f/2
Coating	Alu+MgF_2
Spectral range	200-800 nm
Absolute efficiency	25%
Relative efficiency	32%

4.1.3 EFFICIENCY

The efficiency defines in two terms, the absolute and the relative. The absolute efficiency is the percentage of incident energy of a given wavelength that is diffracted into the order of interest, i.e

Absolute efficiency=(Monochromatic light diffracted by the grating)/

(monochromatic light impinging on the grating)

Absolute efficiency depends on three factors; the groove shape, the reflectivity of the grating surface, and the amount of energy scattered. The relative efficiency which the manufacturers often use, is the ratio of diffracted energy of a given wavelength in the order of interest to that reflected by a mirror of the same material, for the same incident energy, i.e.

Relative efficiency=(Absolute efficiency)/(reflecting power of a mirror)

Gratings have an aluminium coating which absorbs less than 10% of the incident energy. The reflectivity of an aluminium surface normally falls off below 280nm, but if the surface is coated with a thin layer (25nm) of magnesium fluoride (MgF_2), adequate reflectivity is maintained for wavelengths down to 180nm.

4.2 IMAGING PHOTON DETECTOR (I.P.D)

The I.P.D finds applications in many spheres. Primarily developed for very low light level imaging in astronomy and spectroscopy. The I.P.D is ideally suited to most imaging applications in which the photon arrival rate is less than 10^5 detected events per second for the whole device. This count rate limitation is imposed by the dead_time of the processing circuitry. Another count rate limit is imposed by the local dead_time of the channel plates.

4.2.1 PRINCIPLE OF OPERATION

A photoelectron liberated by the photocathode is drawn to the micro_channel plate (MCP), by the electric field applied across the gap. The high electric field causes the electrons to reach the MCP before they have time to drift any considerable distance laterally, and the cathode is said to be proximity focused to the MCP. The channel plate input is covered with a thin membrane of aluminium oxide, which prevents the feedback of ions, generated in the channel plates, to the cathode. A minimum voltage of about 200 volts is required between the cathode and the channel plate to give the electrons sufficient energy to penetrate the ion barrier film. On entering a channel, the primary photoelectron strikes the wall, liberating secondary electrons which are all accelerated down the channel, hitting the wall and producing a large shower of electrons.

There are four channel plates employed, the electron multiplication achieved overall being $\sim 10^7$. These electrons are drawn by a weak electric field (in the order of fifty volts), to a sheet of

resistive material forming the anode. When a charge cloud strikes the anode, a fraction of that charge leaves via each of the four corners which are connected to virtual earth.

The pulses are amplified by fast preamplifiers (one for each corner of the anode), shaped and then fed via cables to the processing unit, fig(4.1). At this stage the pulses are fed into hold circuits and a summing circuit. For the four anodes signals A ,B ,C ,D the following algorithms are then performed internally,

$$X = A + B - (C+D)/A + B + C + D$$

$$Y = A + D - (B+C)/A + B + C + D$$

These values of X and Y are each fed to 10_bit analogue_to_digital converters (A.D.C), the output of which are buffered and then brought out on the front panel to two 15_way D_type connecters. When the A.D.G.s have completed their conversion (the data ready), a pulse of 1μsec duration is generated, this being available on both multi_way connectors and on a separate BNC socket.

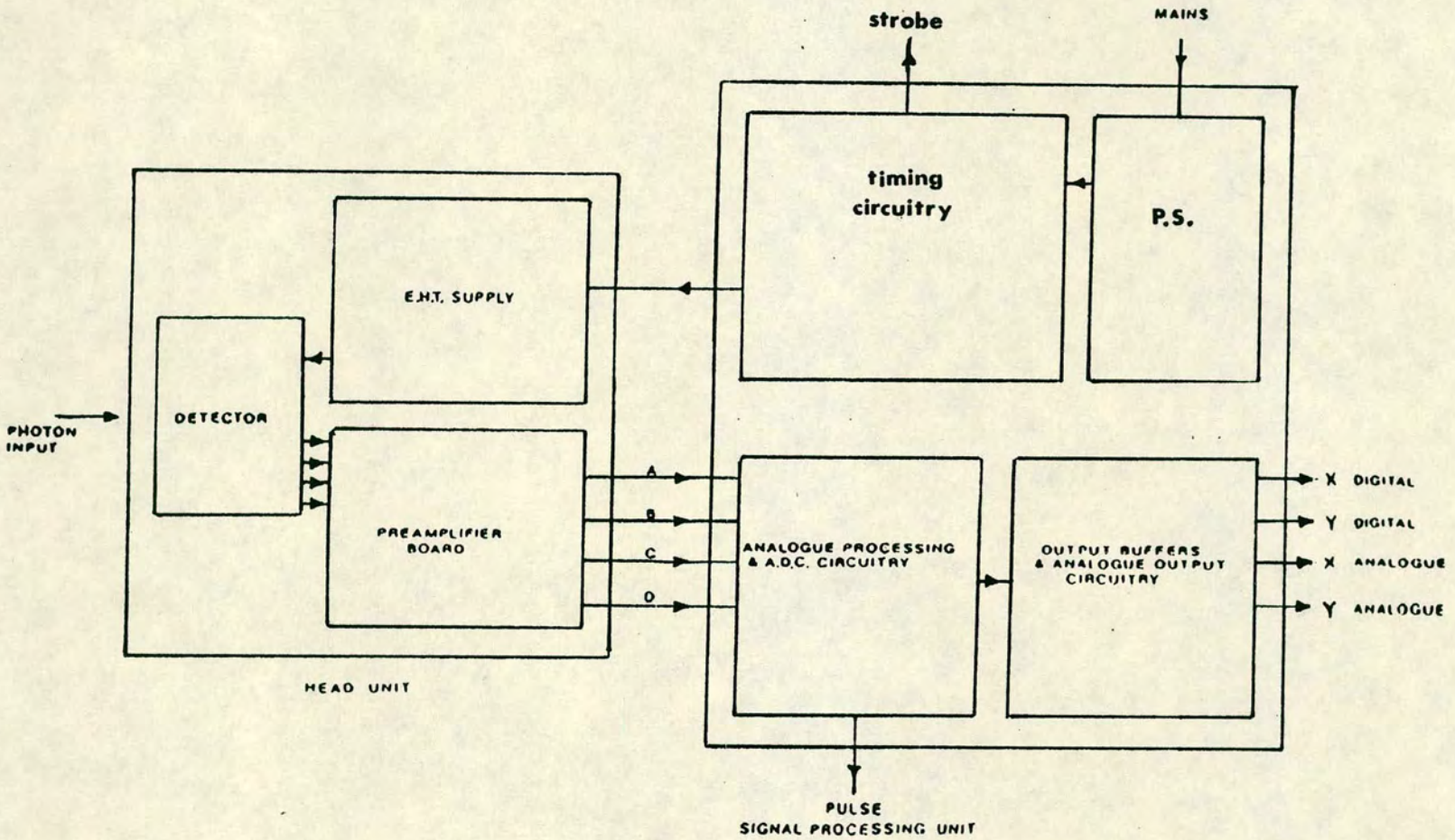

FIG(4.1): Schematic diagram of the head and processing unit of the I.P.D.

4.2.2 RESPONSE TIME

Some modifications have been carried out inside the head unit of the I.P.D . A fast amplifier was built to increase the sensitivity and speed up the response time for coincidence measurements, see fig(4.2). This resulted in an improvement to the response time from typically 80ns to 20ns, the electronic setup used in this test is shown in fig(4.3).

The jitter of the I.P.D strobe was checked using the binary coincidence technique as shown in the schematic diagram(4.4), by imposing a suitable time delay on the signals leaving the pulse output to arrange sequences of correlation in time between the two branches.

The correlation peak which is shown in fig(4.5), shows clearly the time delay required between the two branches is very crucial to get the correlation events.

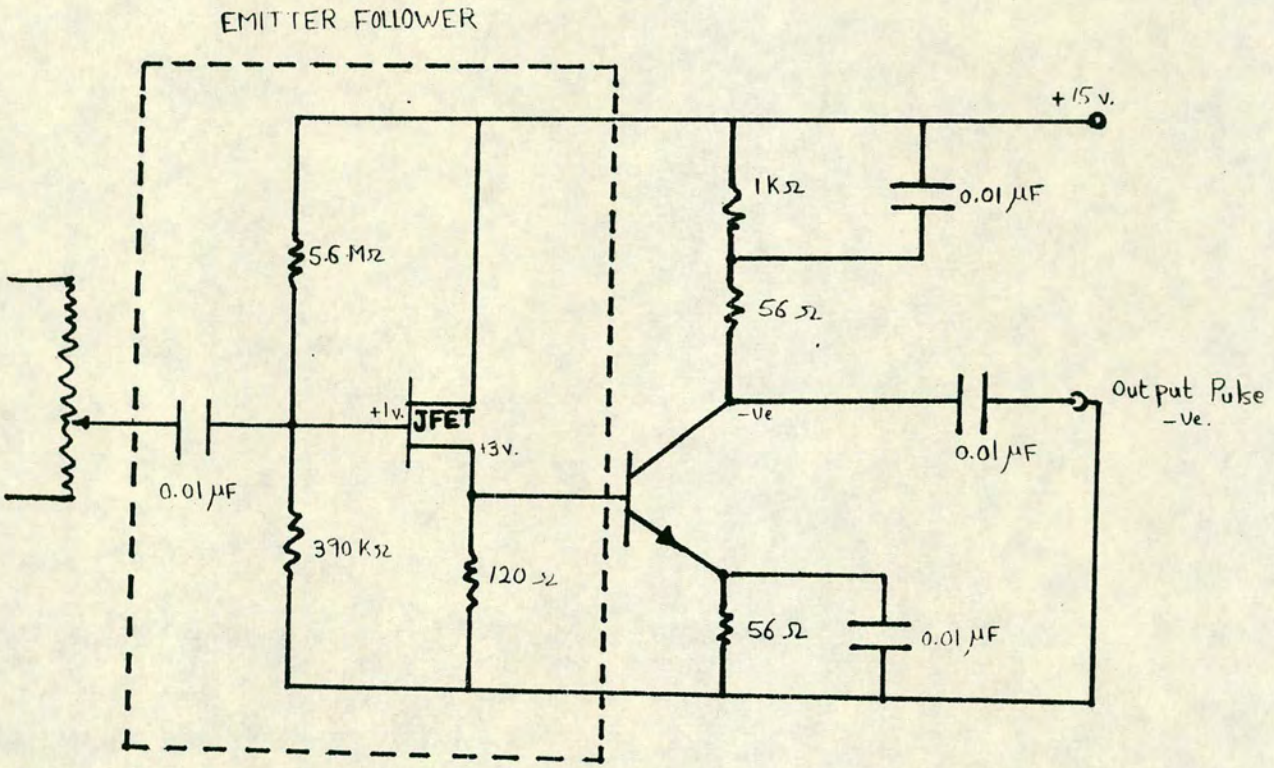

FIG(4.2): Schematic diagram of the modification circuit which was added to the I.P.D head unit.

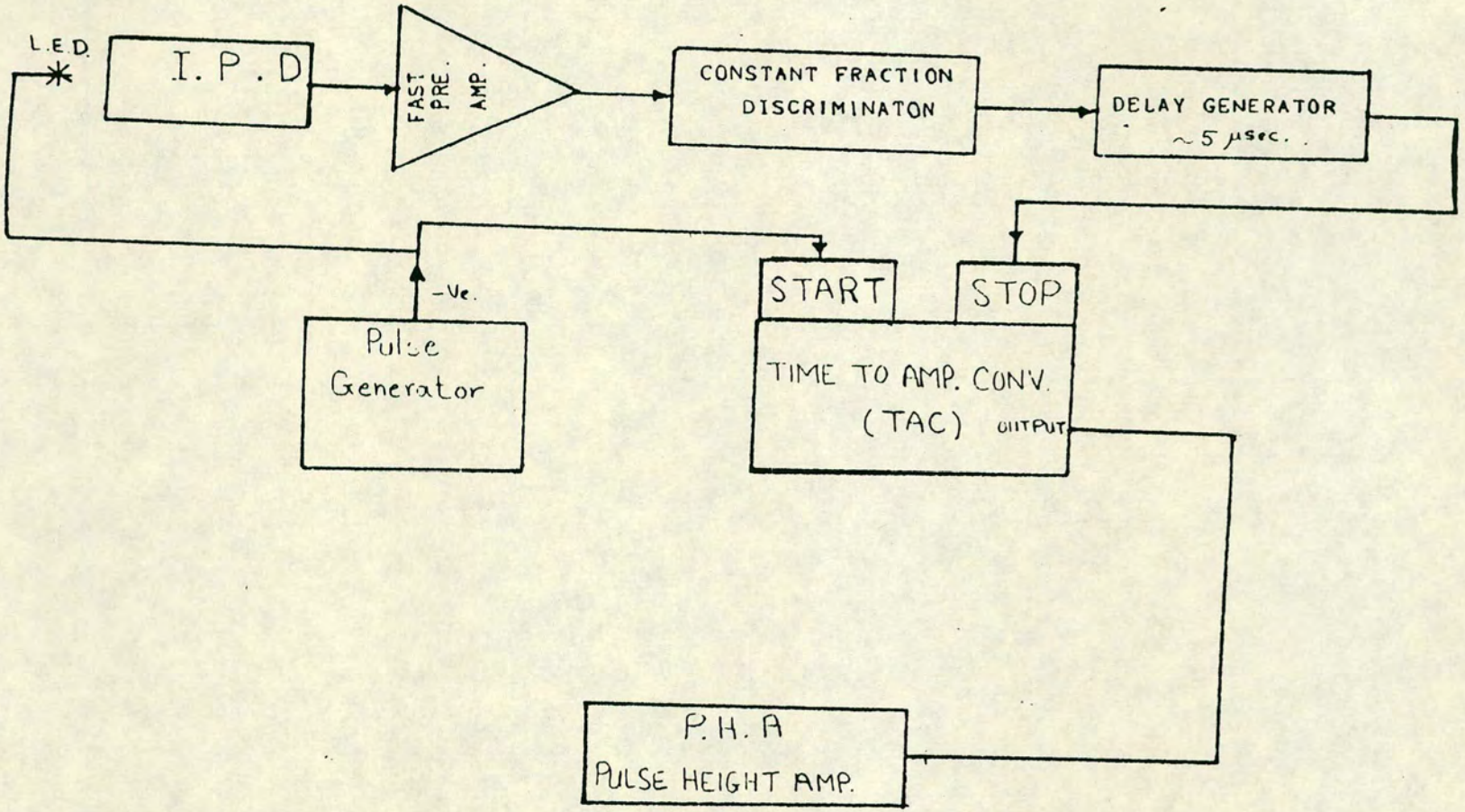

FIG(4.3): Schematic arrangement used for checking the I.P.D response time.

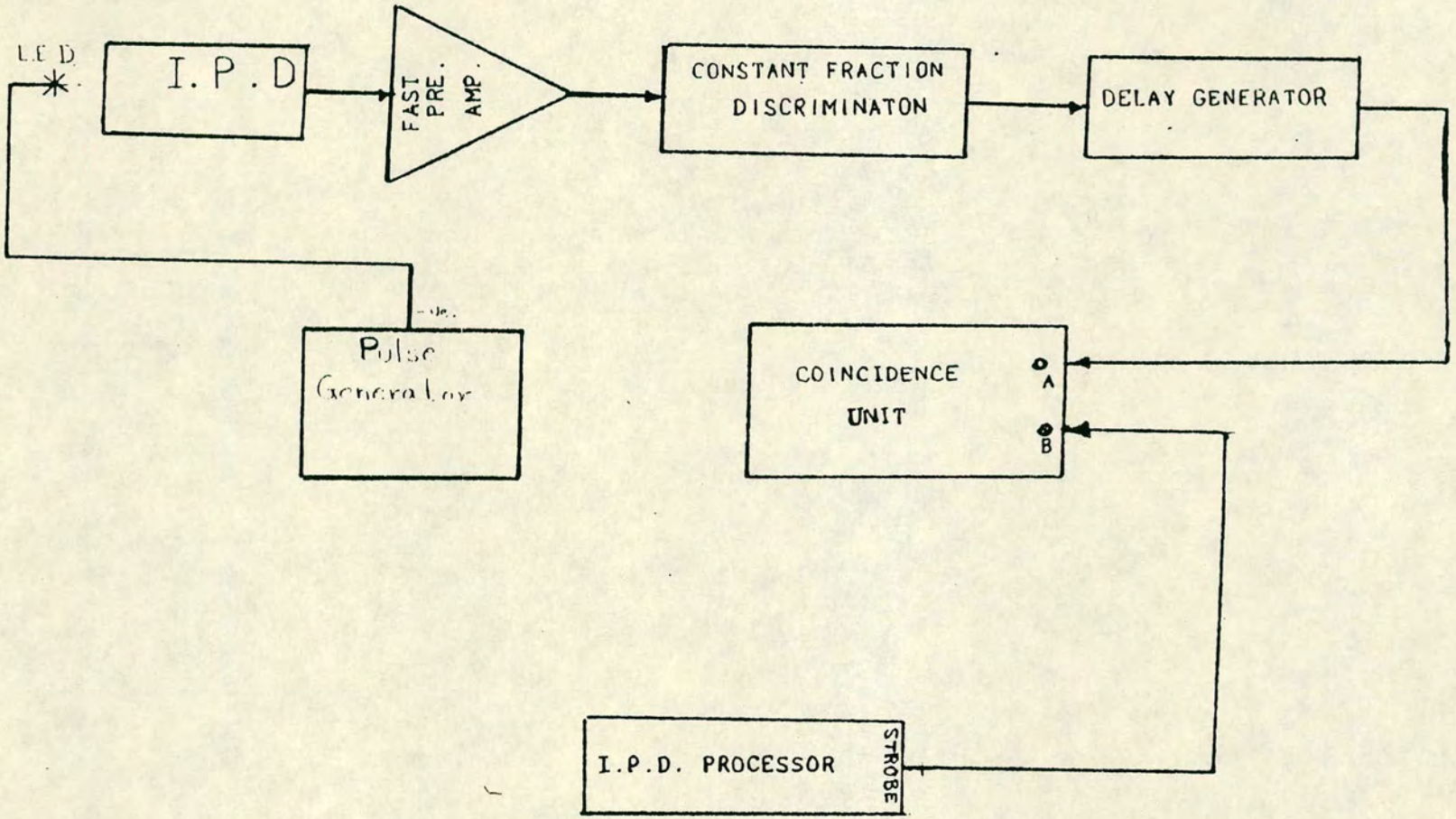

FIG(4.4): Schematic arrangement used for checking the jitter of I.P.D strobe.

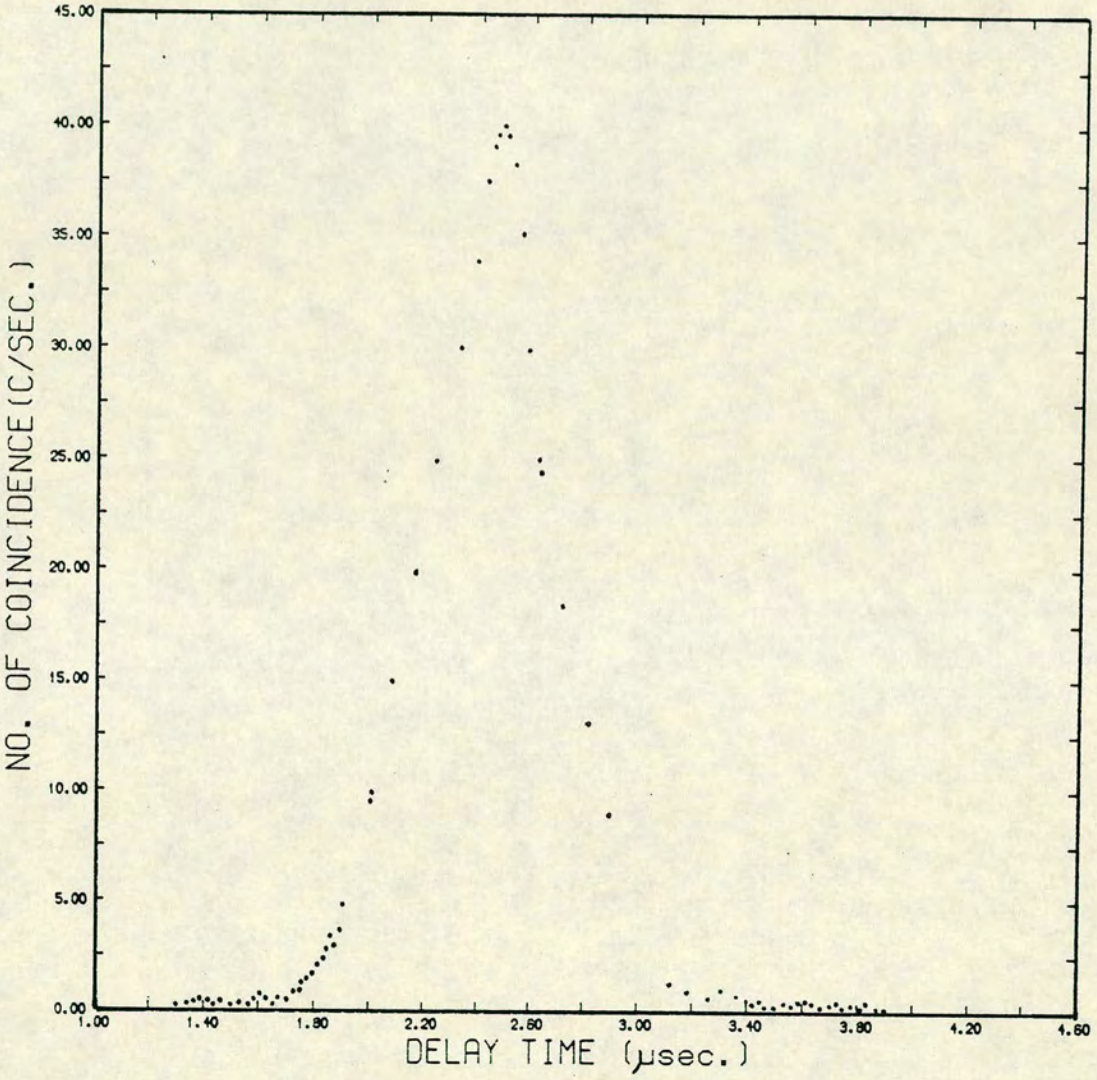

FIG(4.5): Graph of the forced coincidences between the pulse and strobe output of the I.P.D processing unit.

4.3 TARGET BEAM

The target system which is shown in fig(4.6), was designed to produce beams of gases as cross_beam material to intercept the main beam in an effective collision volume, defined by the intersection region. It is convenient to explain the target system in the following sections :

4.3.1 TARGET SOURCE CONSTRUCTION

In recent years a wide range of techniques has been used to produce collimated molecular beam targets. These techniques have been reported in a number of papers (J.B.Fenn et al 1966[37], and K.Bier et al 1966[38]). In designing the target source the major emphasis has been on the following factors:

(1) A target beam density sufficient to produce 10% attenuation. For a single fast particle moving through a small distance dx in a gas, the probability P of making a collision in this distance is given by:

$$P = dx/l = n \cdot \sigma \cdot dx$$

where l is the mean free path, n is the number density and σ is the cross section.

A flux of N projectile particles per unit area moving at velocity V is reduced in distance dx by,

$$dN = n \cdot N \cdot \sigma \cdot dx$$

by integrating the above equation, one obtains,

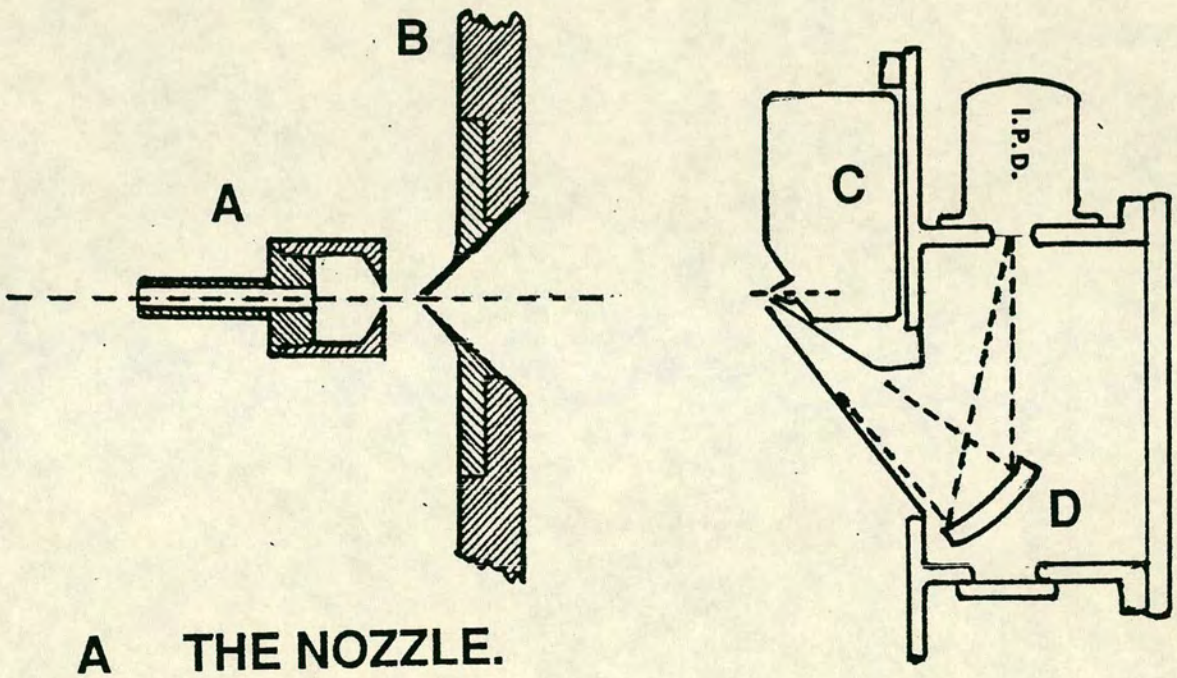

A THE NOZZLE.

B THE SKIMMER

C THE DUMP TANK & TARGET MONITOR.

D A HOLOGRAPHIC GRATING.

FIG(4.6): Schematic diagram of the target assembly.

$$N = N_0 \cdot \exp(-n.\sigma.x)$$

For the flux density N after passing a distance x, and if the particles carry a single charge the current,

$$I_0 = N_0 \cdot V$$

Is reduced through the gas target to a value I

Where $$I = I_0 \cdot \exp(-n.\sigma.x)$$

If $n \cdot \sigma \cdot x \ll 1$, then

$$I/I_0 \simeq 1 - n \cdot \sigma \cdot x$$

For x=0.3mm, $\sigma \simeq 10^{-16} cm^2$ and I/I_0=0.9, the density in the collision region would be ~$3 .10^{16}$ $mol.cm^{-3}$. This density has been produced using up to 8 bar gas_line pressure at pulse rates of up to 45 pulse per second and a nozzle open time 1.5ms.

(2) Achieving a cross_section at the collision zone of 0.3x10mm.

(3) The ratio of forward gas intensity through the skimmer to the total gas leaving the nozzle high enough to control the residual gas in the nozzle chamber.

The nozzle is arranged to slide on a dural mount, so that the nozzle can be positioned remotely in two axes. Thus the distance from the skimmer can be varied during operation as can the transverse alignment of the nozzle relative to the skimmer, see fig(4.7,4.8).

The flow of gas from the nozzle orifice of 86 $.10^{-3}$cm diameter (area ~$5.8 .10^{-3} cm^2$), is given by:

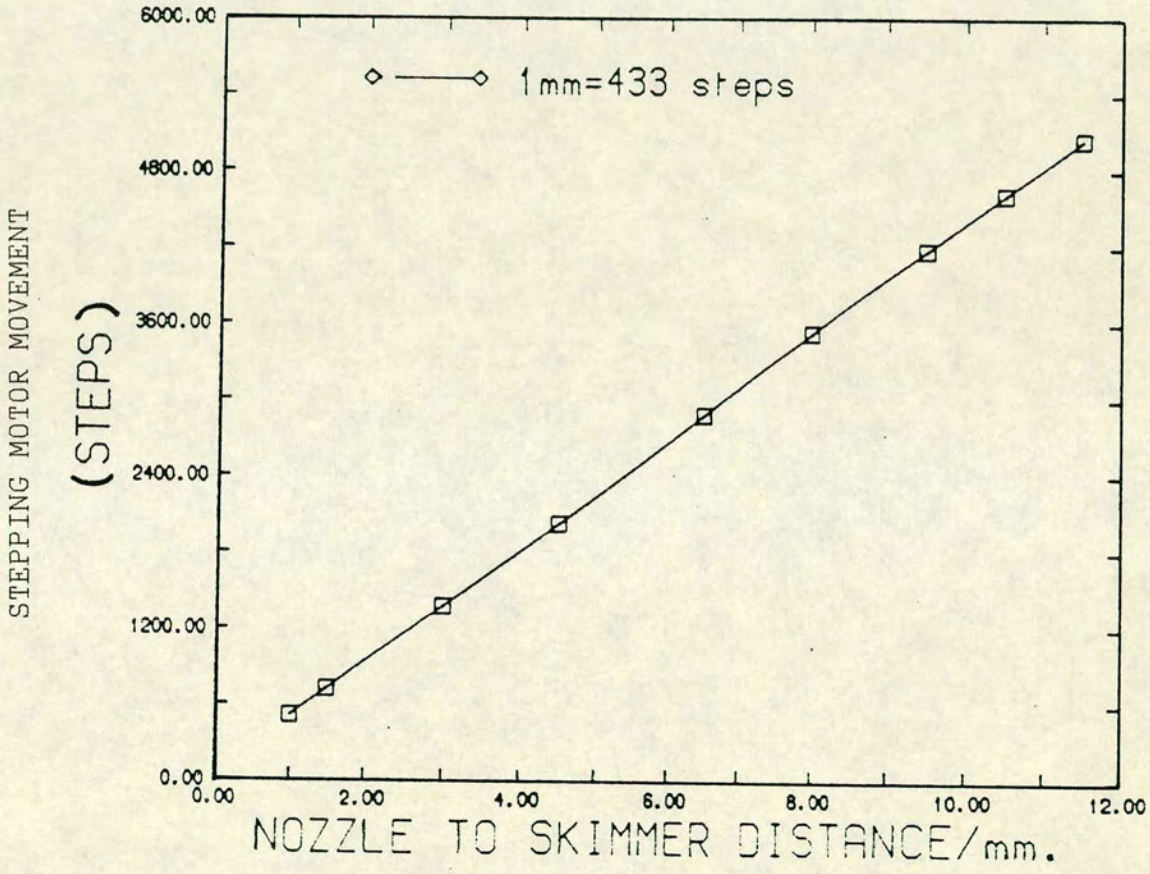

FIG(4.7): CALIBRATION OF THE NOZZLE DRIVING MOTOR.

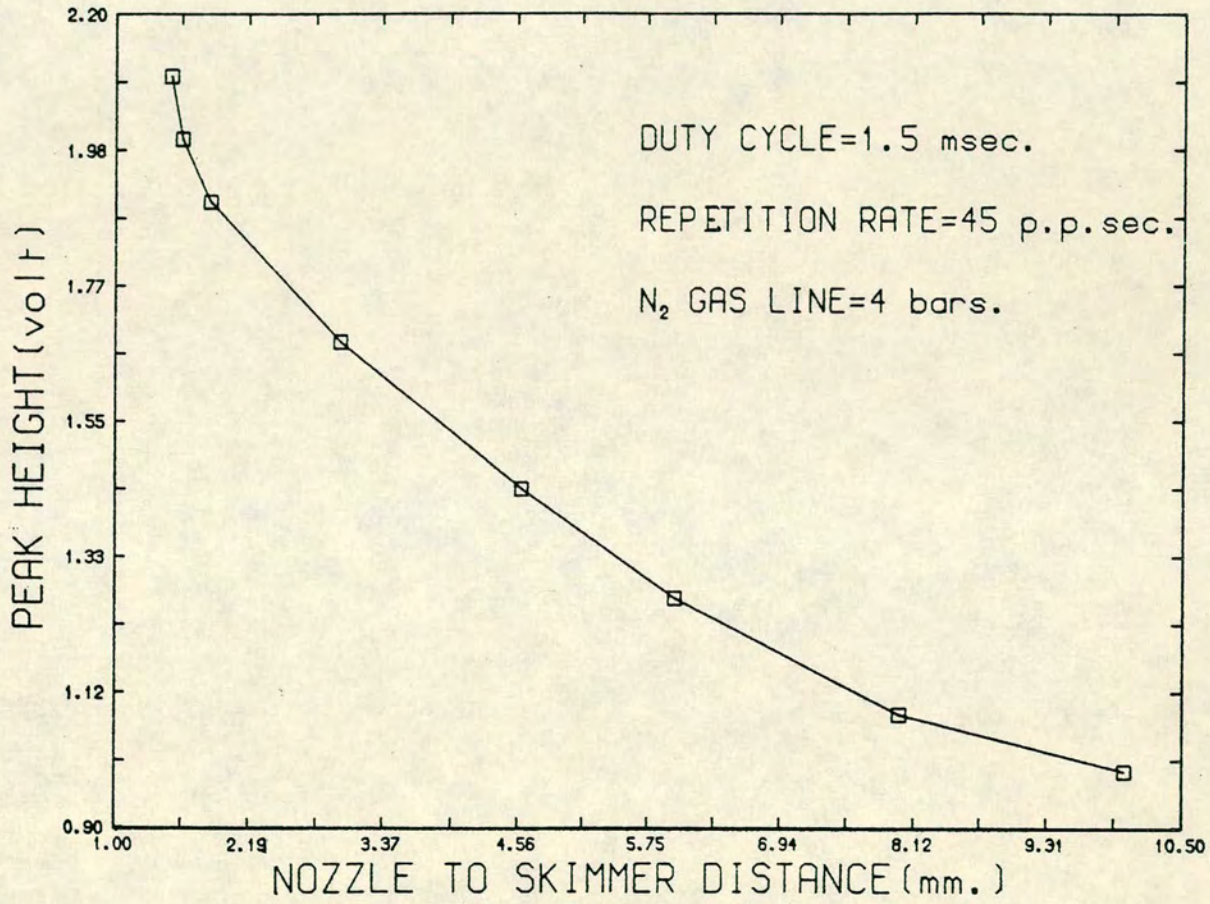

FIG(4.8): Monitoring the collimation
of the target assembly.

$$\text{Gas Flow} = 1/4 \,.A\,.\,V\,.\,D$$

$$\simeq 0.43\,.10^{19}\ \text{mol/sec}$$

where A is the orifice area, V is the target velocity and D is the target density.

The gas flow through the nozzle can conveniently be modulated by an electrically driven fuel injector valve with an operating time 1_2ms, so that measurements can be taken in the free expansion period before saturation of the vacuum plant. The skimmer slit is 0.04mm wide with external angle 60° and internal angle 58°. The nozzle chamber was pumped by a 40cm oil diffusion pump. The target beam was monitored by a device mounted inside the dump tank (across the chamber). It consists of a double ion_gauge, one element of which samples the target beam as it enters the dump tank, while the other element samples the background pressure in the dump tank. The output from these two gauges is connected to an oscilloscope.

4.4 TARGET PERFORMANCE

The target beam is produced by free expansion from a slit nozzle. The expanded beam is collimated by a skimmer, crosses the collision zone and finally collected in a dump tank.

The required target density implies a gas_load in the collision chamber given by:

$$\text{Gas\_Load in collision chamber} = D \cdot V \cdot A \cdot \text{Valve open time(1.5ms)}$$

$$\simeq 13.5 \cdot 10^{16} \text{ molecule/sec}$$

where D is the target density, V is the target velocity and A is the area of the collision zone.

The gas load in the collision chamber depends on how effective the dump tank is in capturing the target beam and how much of the background gas in the nozzle chamber after a pulse leaks through the skimmer slit (4.9,4.10). The permitted open period (duty cycle) is roughly equal to the flight time from the collision to the chamber walls and back about 1_2ms. see fig(4.11). The apparatus then recovers and the cycle repeats. The fuel_injector valve was capable of a repetition rate of around 100Hz; in practice 1.5ms was about the best operating open period with a repetition rate of 45 pulses per second, see fig(4.12).

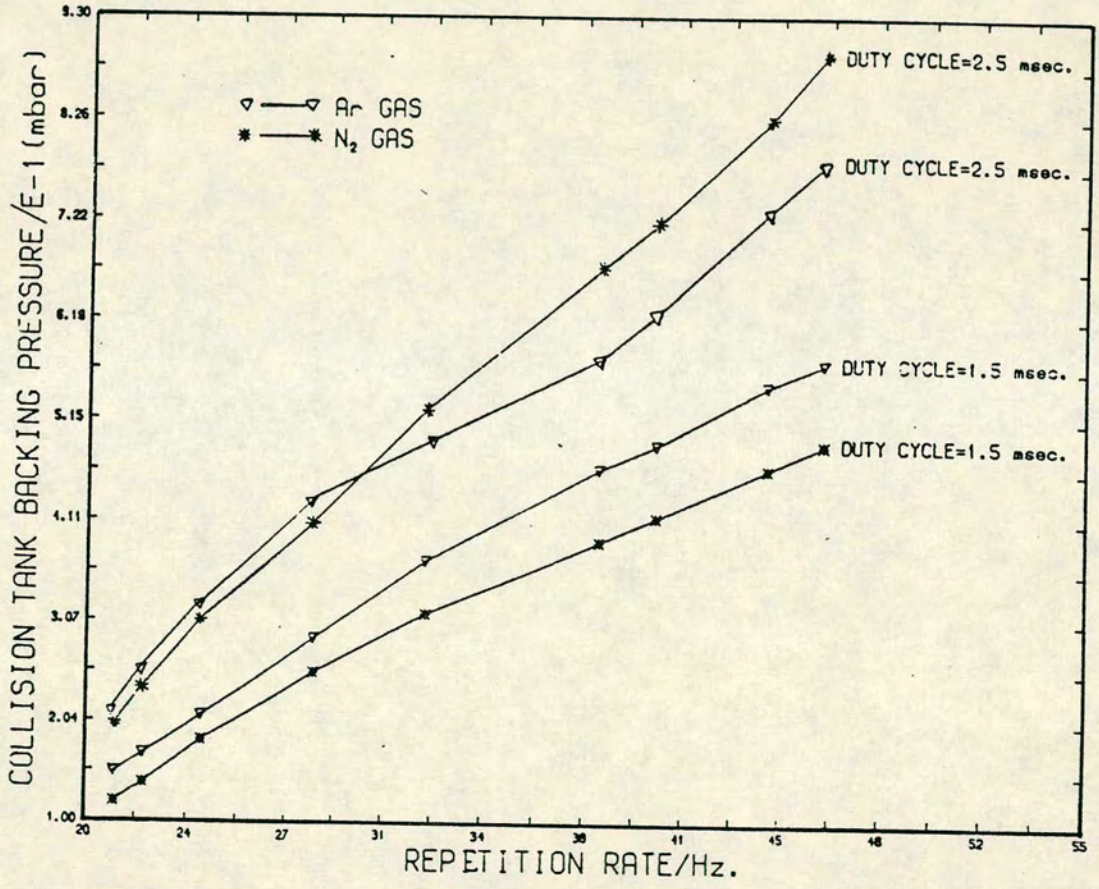

FIG(4.9): Response of the collision tank backing pressure to the nozzle repetition rates.

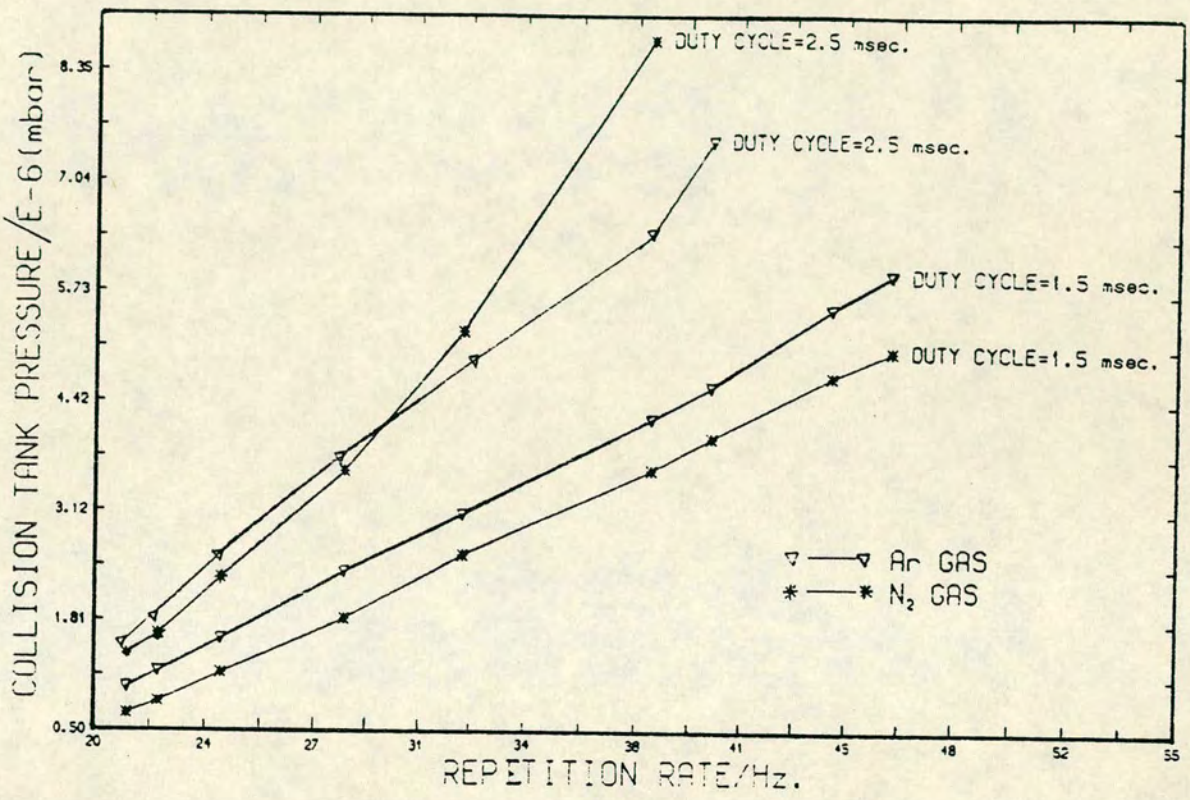

FIG(4.10): Response of the collision tank pressure to the nozzle repetition rates.

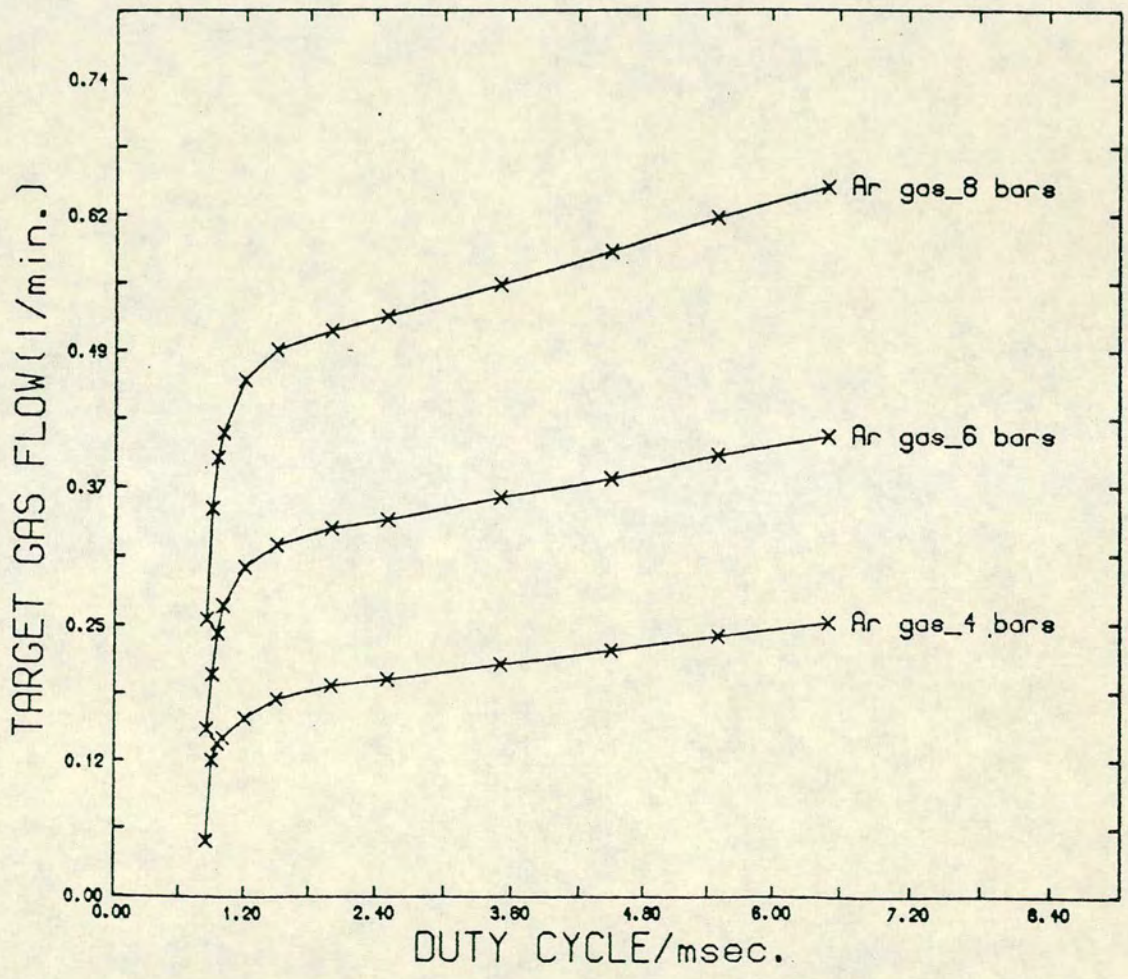

FIG(4.11): Performance of the nozzle duty cycle.

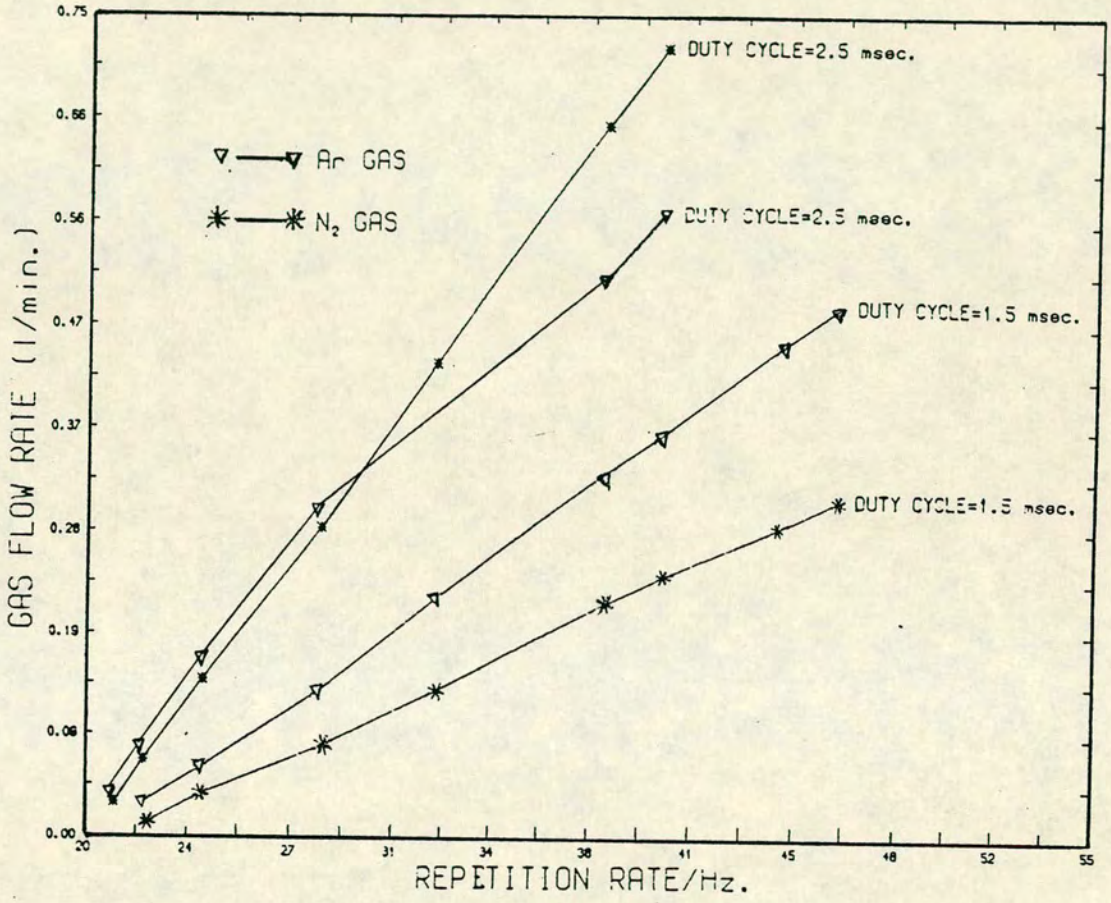

FIG(4.12): Performance of the nozzle repetition rates.

4.5 POSITION SENSITIVE PARTICLE DETECTOR

This detector, figure(4.13,14), designed to be used in experiments involving the scattering of atoms or ions, uses a rather novel optical fiber technique, with capability of recording particles at 45 angular location simultaneously, covering angular range of approximately 0_8°, with resolution of 0.1_0.2°. For full details of the detector, see appendix_publication.

4.5.1 ADVANTAGES

This detector able to provide the following advantages:

1. Since the measurements at all scattering angles are carried out simultaneously, beam fluctuations have equal effects at all scattering angles.
2. The detector provide a response time about 10ns.
3. The signal_to_noise ratio is increased greatly because of the binary coincidence technique used in the detection system.

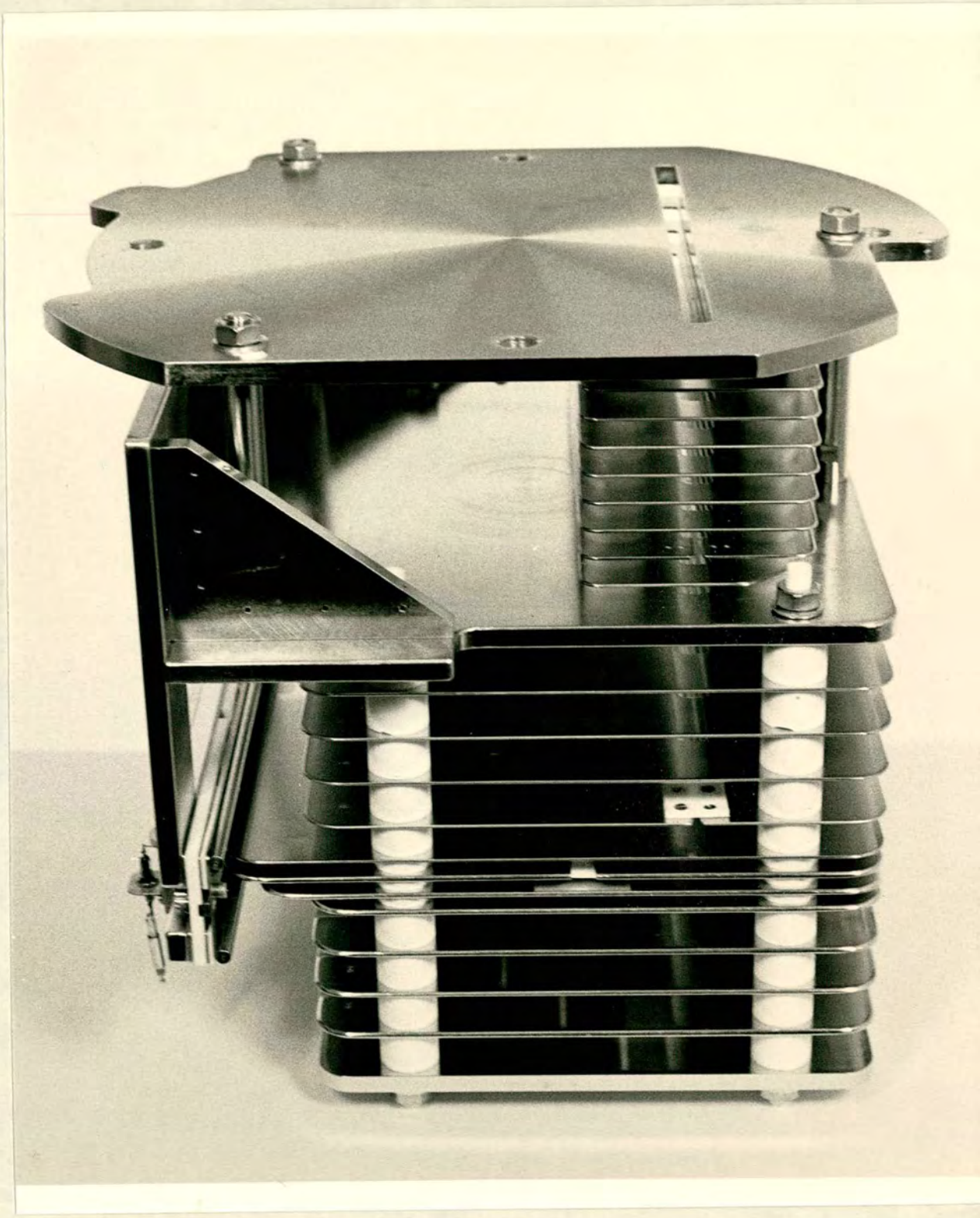

FIG(4.13): Photograph of the multi_angle particle detector.

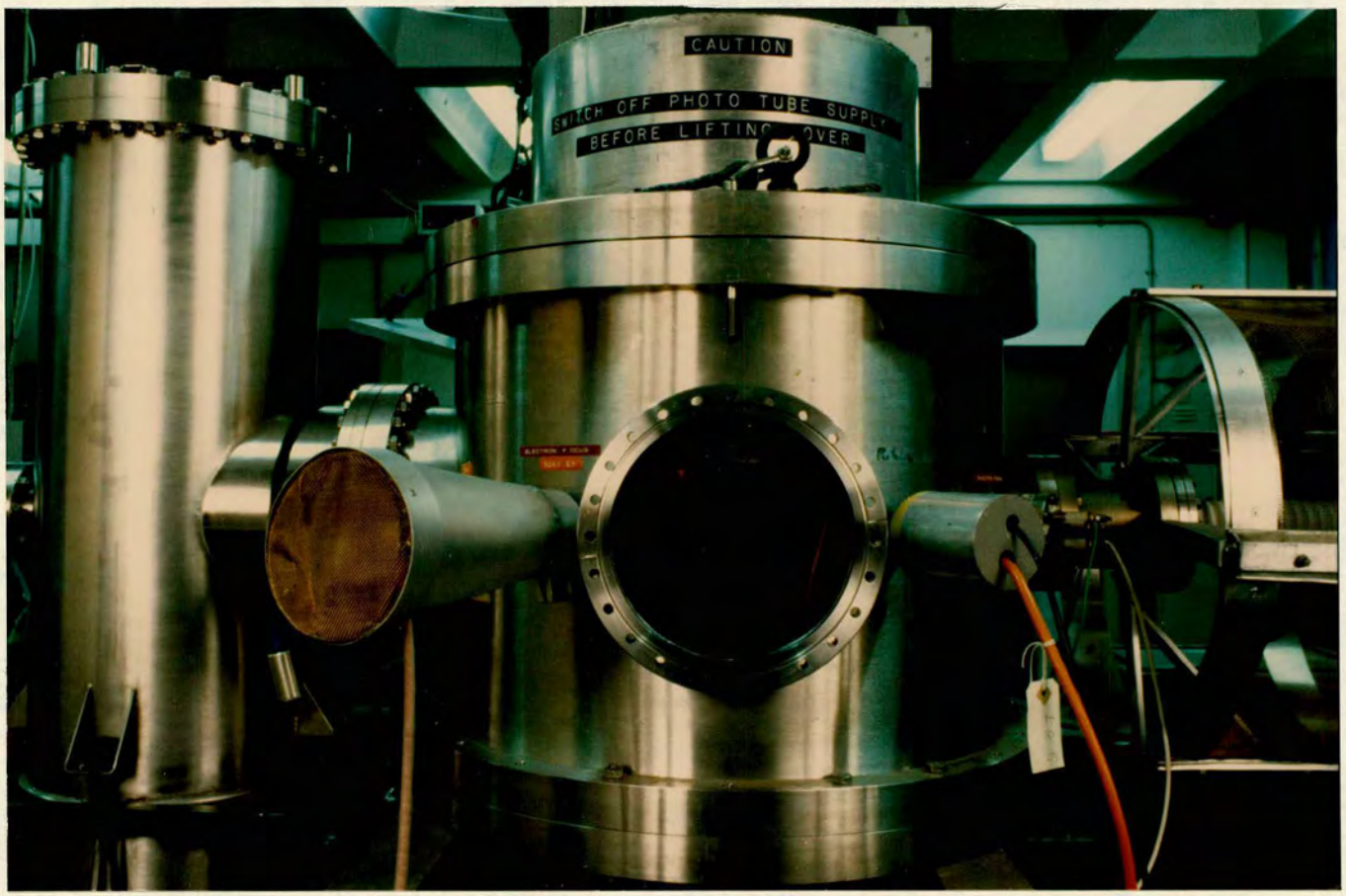

FIG(4.14): Tank containing multi_angle particle detector with (a), on left, feedthrough for electron focus voltage (b), on right, feedthrough for the accelerating voltage(EHT) (c), on top, the photomultipliers bank and scintillators.

4.5.2 PRINCIPLES OF OPERATION

A simplified diagram of the detector is shown in fig(4.15). The device is based upon a successfully operating Daley type[39]. single channel particle detector, using a binary coincidence technique to determine the position of an event. The ions enter a modified Pierce gun[40], designed to produce a parallel sheet of ions. The entrance slit of the Pierce gun is arranged to intersect a wide range of scattering angles following the collision of the positive ions with atoms or molecules in the crossed beam experiment. The ions are injected into a region of strong, constant vertical electric field and fall in a parabola on to an Al_2O_3 plate. Secondary electrons ejected from this plate are focused through an electric field to form an image of the initial scattering pattern on an array of scintillators. The location of a scattering event in angle and time is then coded by a bank of photomultipliers multiplexed via optical glass fibres to individual elements in the scintillator array. Each scintillator produces about 250 photons per electron at 50kv[41]. Each angular element is connected to two photomultipliers, an arrival event signalled by an electron burst on a specific scintillator element produces simultaneous signals in both photomultipliers. If this coincidence is detected, the arrival time can be determined directly while the angular location of the event is coded by noting which specific pair of photomultipliers are involved in the coincidence. Thus a bank of 10 photomultipliers could encode by this binary coincidence method $^2C_{10}$, i.e. 45, individual angular elements.

The final section of the apparatus thus consists of a network of fibre optic bundles which connect the individual scintillator elements

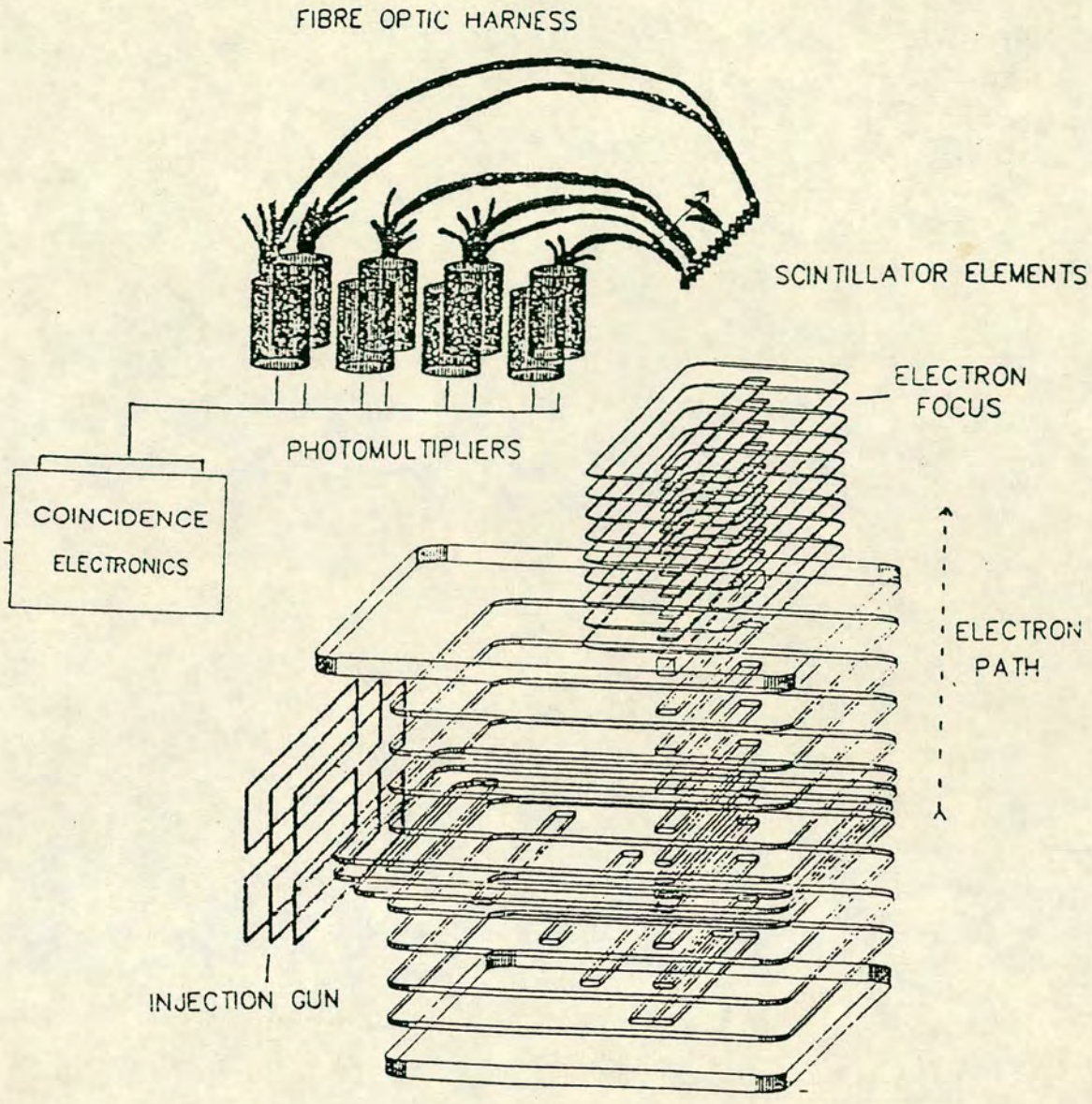

FIG(4.15): Schematic diagram of the multi_angles particle detector.

to a bank of photomultipliers, each photomultiplier being connected to 9 different scintillators. the signals from these multipliers are processed by a high speed electronic interface (10ns). The correlation between the photomultiplier signals, determines the address of the scintillator element responsible and outputs both time and angular information to a micro_computer.

4.5.3 SENSITIVITY

The sensitivity of this detector can be checked in two ways. First, by measuring the emission of ions from a KCl coated tungsten wire located approximately at the collision zone, then the efficiency is obtained from the ratio R between the normal coincidence count rate P_2 of a single channel at any angle and the non_coincidence count rate P_1, under the same conditions.

$$R = P_2/P_1$$

Second, by calculating the detection probability P_R of registering an event by R_fold coincidence which is given by:

$$P_R = P_C.t\ [1 - (1 - rd)^{ljpe/2}]^R$$

The estimates of the parameters mentioned above are given in table_II_.

Because there are many uncertainties in using the second method, mainly in the optical collection efficiency and the number of photons produced, the first method was preferred.

Measurements using the first method are shown as a function of the device operating voltage in fig(4.16).The comparison between the measurements using the first method (the solid curve), with the second method (the dotted curve), showed satisfactory agreement at e=0.05 . It can be seen on the same graph that the desired operating region on the plateau can be established at voltages greater than ~53kv .

TABLE -II -

PARAMETER	ESTIMATED VALUE	REPRESENTS
Pc	$\sim$ 0.9	Probability of producing an ion from neutral incident atom.
t	$\sim$ 0.95	Transmission probability for the ion to the Al_2O_3 surface.
L	$\sim$ 0.9	Transmission probability for an electron from the Al_2O_3 surface to the scintillator.
P	$\sim$ 250 photons at 50kv	Number of photons produced per electron in the type 102A scintillator.
J	11 electrons at 50kv.	Number of secondary electrons produced per ion.
r	0.2	The photomultiplier counting efficiency.
d	0.5	The fibre transmission.
e	0.02	The collection efficiency from scintillator to fibre.

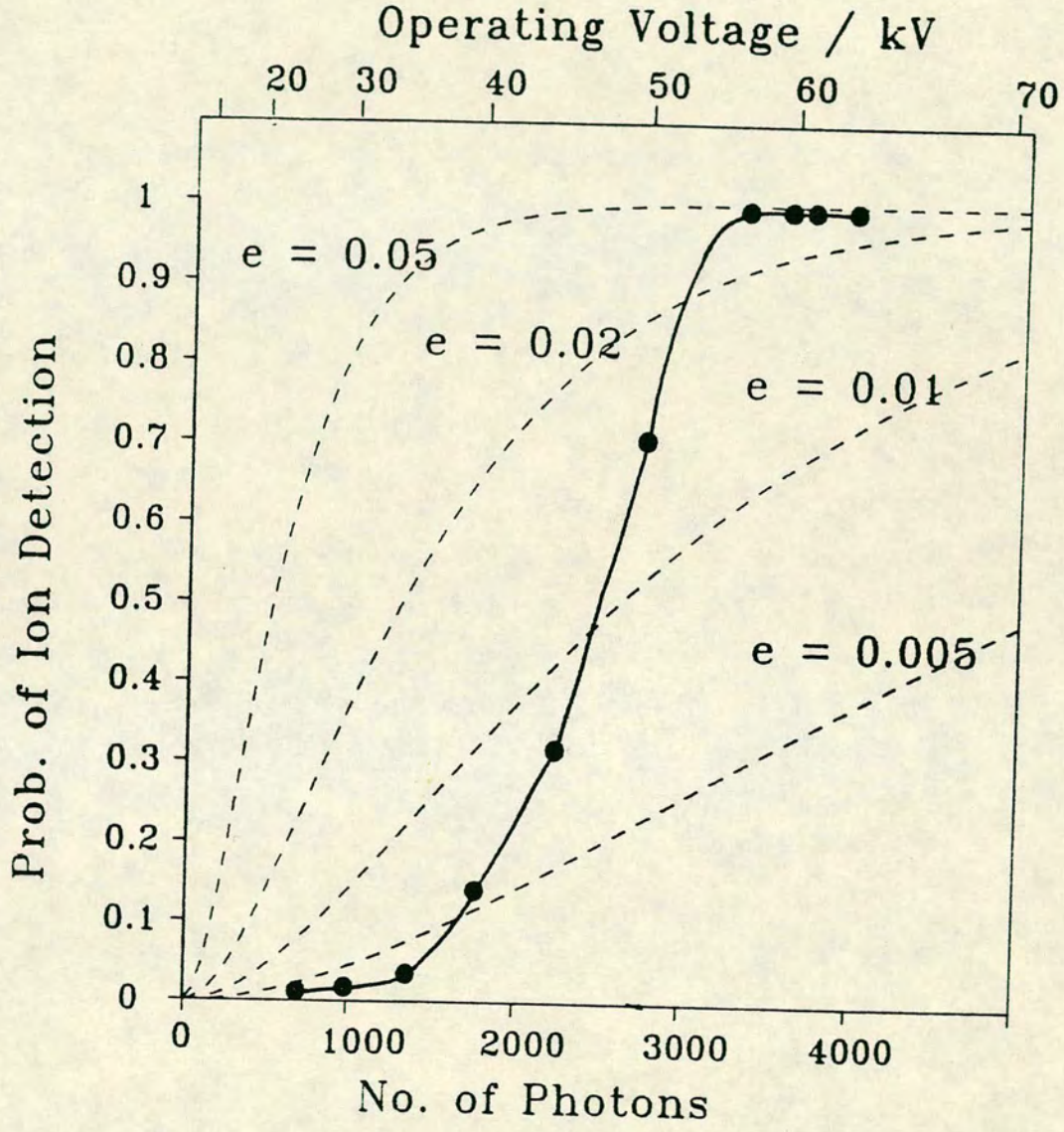

FIG(4.16): The detection sensitivity of the multi_angle particle detector.

Chapter 5
ANGULAR DISTRIBUTION OF ELASTIC SCATTERING FOR He^+/Ar

A great wealth of information on angular distribution has continued to accumulate during the last twenty years, due to experimental developments in the fields of atomic and molecular beams and of spectroscopy of colliding species. This in turn has motivated a number of theoretical contributions, some of which are designed to interpret experimental results, others to isolate concepts and methods of predictive value. Throughout most experimental works the angular distribution is regarded as the most direct probe of the collision dynamics.

The basic requirement for understanding many physical and chemical phenomena is knowledge of a potentialenergy curve. It is through the elastic scattering the potential energy curve can be constructed. But it has to be said that this method cannot compete with the spectroscopy method concerning the precision of the potential determined; however the beam scattering method is in principle more universal than spectroscopy and covers the entire energy range.

5.1 GENERAL BACKGROUND

The scattering was first observed in α_particle collisions with atoms which led Rutherford early in this century to suggest the model of the atom where the positive charge is concentrated in a small central nucleus.

The experimental side of the elastic scattering field has been carried out principally in the forties and fifties by Amdur and his colleagues[42,43], who studied fast atom scattering. Simons and his co_workers[44,45] studied ion beam scattering. In the sixties and seventies extensive developments led to observing and understanding most of the important phenomena (Bernstein and Muckermann 1967[46]; Pauly and Toennies 1965[47]; Pauly 1974[48]). As a result elastic scattering has emerged as an almost routine laboratory tool for measuring potential curves.

The theoretical side of the elastic scattering is very well understood. For most atomic species the wavelength of the relative motion is small compared to a characteristic distance of the potential. Thus classical mechanics (Firsov 1953[49]) is a good approximation for describing the dynamics of the collision. However, the results of molecular beam measurements show a number of important features of the cross section which require a quantum mechanical treatment (Rosen and Yennie 1964[50]). The semiclassical treatment, which is based on replacing the classical particles by wave packets, proves to be a good compromise between an exact description of the process and an intuitive understanding of the physical picture (Ford and Wheeler 1959[51]).

5.2 AVAILABLE METHODS FOR THE DETERMINATION OF THE POTENTIAL

5.2.1 FITTING PROCEDURES

This method is widely used; it is based on the assumption for the interaction of a specific functional form and then calculating the deflection function and the cross section. These calculations are compared with measured properties. The actual potential is derived by varying parameters inserted in the potential by trial so as to obtain the best fit to the measured cross section.

In concept this method suffers from the drawback that the parameters determined in this way are dependent on the potential model. Thus the most important task in applying such a method is to find a model potential which is flexible enough to fit the data (Siska et al 1971[52]. Another way is to use special functions only over a restricted range for which they are assumed to be the right description (Gegenbach et al 1972[53]).

5.2.2 INVERSION PROCEDURES

All the difficulties of a fit procedure mentioned previously can be avoided by applying the inversion procedure which has proved to be applicable for most atomic and molecular collisions. The advantages of this method are:

First, only data which can be experimentally measured are used to built the potential curve without being influenced severely by the parametrisation used to construct the potential curve; second, there

are no restrictions imposed by the set of functions to calculate the cross section, the deflection function and the potential; third, it allows us to compile into one picture data taken at widely varying energies. For these reasons this method is used to determine the potential curve in this chapter.

The method used the reduced variable technique (angle and differential cross section) introduced by Smith et al 1966[54], as a starting point to calculate the deflection function which leads to construction of the interaction potential.

5.3 METHOD

Firsov[49] developed a method of obtaining the potential energy function by direct manipulation of the data from scattering experiments carried out at a single energy. This was further developed by Lane and Everhart[55]. Their method allowed results from various energies to be used and hence a fuller picture of the potential to be built up. The main improvement on Firsov's method was the introduction of the small angle forward scattering approximation[56] in terms of the reduced scattering angle, i.e.

$$\tau = E \cdot \theta \qquad (5.1)$$

where τ = Reduced scattering angle.

E = Impact energy (laboratory system).

θ = Scattering angle (laboratory system).

The two_particle collision problem is reduced to a one_particle problem by transformation to the center_of_mass system. Lehmann and Leibfried[57,58] had shown that, in a small angle limit τ may be expressed as a power series in reciprocal energy in which the coefficient of each term is a function of b (impact parameter) alone, i.e

$$\tau(E,b) = \tau_0(b) + E^{-1} \cdot \tau_1(b) + \ldots\ldots \qquad (5.2)$$

Where the first term of the series is given by :

$$\tau_0(b) = -b \int_b^\infty (dV/dr) \cdot dr \,/\, (r^2 - b^2)^{1/2} \qquad (5.3)$$

Inverting equation (5.2) gives b as a function of τ and E in a similar

series.

$$b(\tau,E) = b_0(\tau) + E^{-1} \cdot b_1(\tau) + \ldots\ldots \qquad (5.4)$$

Using equation (5.4) and the classical expression for the differential cross section, i.e

$$\sigma(\theta) = b \,/\, [\sin\theta \cdot (d\theta/db)] \qquad (5.5)$$

one can construct the appropriate reduced cross section $\rho(\tau,E)$. This may be written as a similar power series in reciprocal energy.

$$\rho(\tau,E) = \theta \cdot \sin\theta \cdot \sigma(\theta,E) \qquad (5.6)$$

$$= 1/2 \cdot |\partial b^2/\partial \mathrm{Ln}\tau| \qquad (5.7)$$

$$= \rho_0(\tau) + E^{-1} \cdot \rho_1(\tau) + \ldots\ldots \qquad (5.8)$$

The small angle approximation is:

$$\rho(\tau,E) = \rho_0(\tau)$$

omitting all but the first term in equation (5.8).

This scaling procedure allows information from experiments performed at various energies to be used simultaneously. Integrating equation (5.7) in the small angle limit gives[56] :

$$b_0^2(\tau) = 2 \int_\tau^\infty \rho_0(\tau) \cdot d\mathrm{Ln}\tau \qquad (5.9)$$

This gives an estimate of impact parameter as a function of reduced scattering angle. From this, one may obtain the reduced deflection function $\tau_0(b)$, and the potential energy curve is then found by the integration,

$$V(r) = 2/\pi \int_r^\infty \tau_0(b) \cdot db \,/\, (b^2 - r^2)^{1/2} \qquad (5.10)$$

5.4 EXPERIMENTAL PROCEDURE

The schematic diagram of the apparatus setup is shown in fig(2.4) chapter_2_. The He^+ ions produced in the source (low voltage discharge), are extracted and focused through a spherical energy analyser, a series of ion_optical lenses then focuses and transports the beam to the collision region to yield a ribbon beam 0.3x8mm. The target beam is generated by a pulsed nozzle and skimmer arrangement and collimated to 0.3x8mm cross section. The multi_angle particle detector provides 45 separate angle elements over a span of about 8°. The response time is less than 10ns. The collisions (beam crossing) were arranged between $He^+(1s) \rightarrow Ar(3p^6)$, the scattered He^+ ions at a particular angle θ_{ion} with an intensity $I(\theta_{ion})$ being recorded in the particle detector using the optical fibre technique. The attenuated beam was monitored throughout the experimental run by a specially designed Faraday cup, see fig(5.1), and the beam current was recorded on a chart using a pen_recorder.

5.5 RESULTS AND DISCUSSION

The experimental data of the $He^+ \rightarrow Ar$ system were obtained at laboratory energies 100_900eV. The intensity I, of the elastically scattered He^+ ions was measured as a function of scattering angle, θ, and is presented in fig(5.2). The figure shows the raw data. Several corrections were applied to these data.

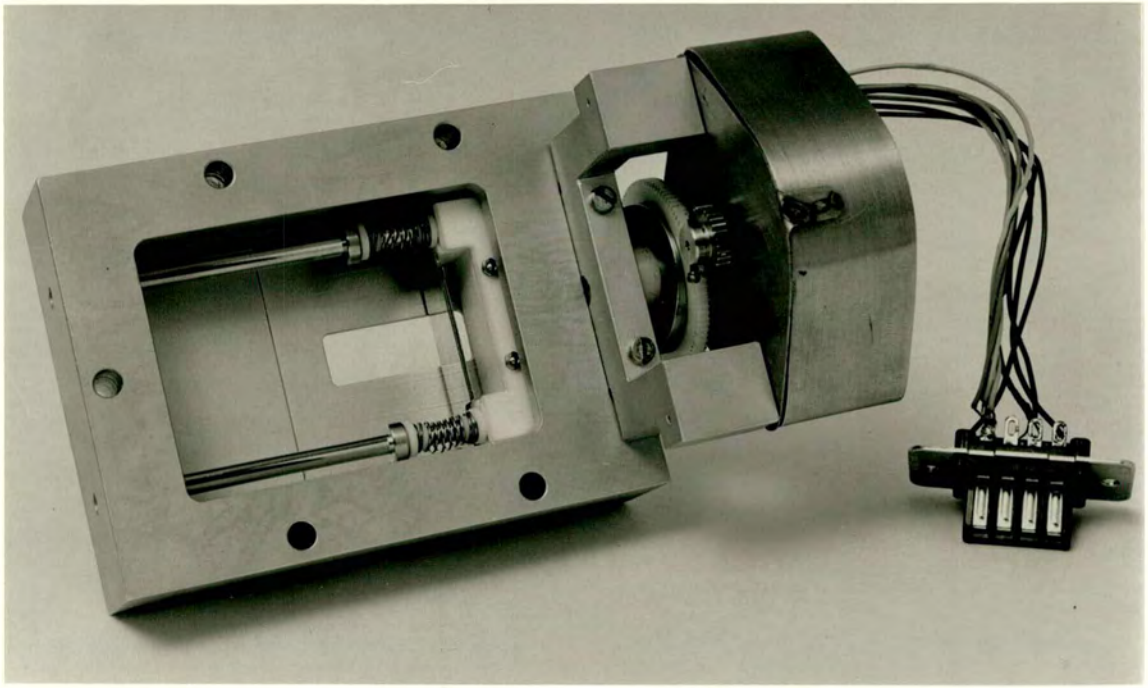

FIG(5.1): Photograph showing the side view of the post collision zone beam monitor(Faraday cup).

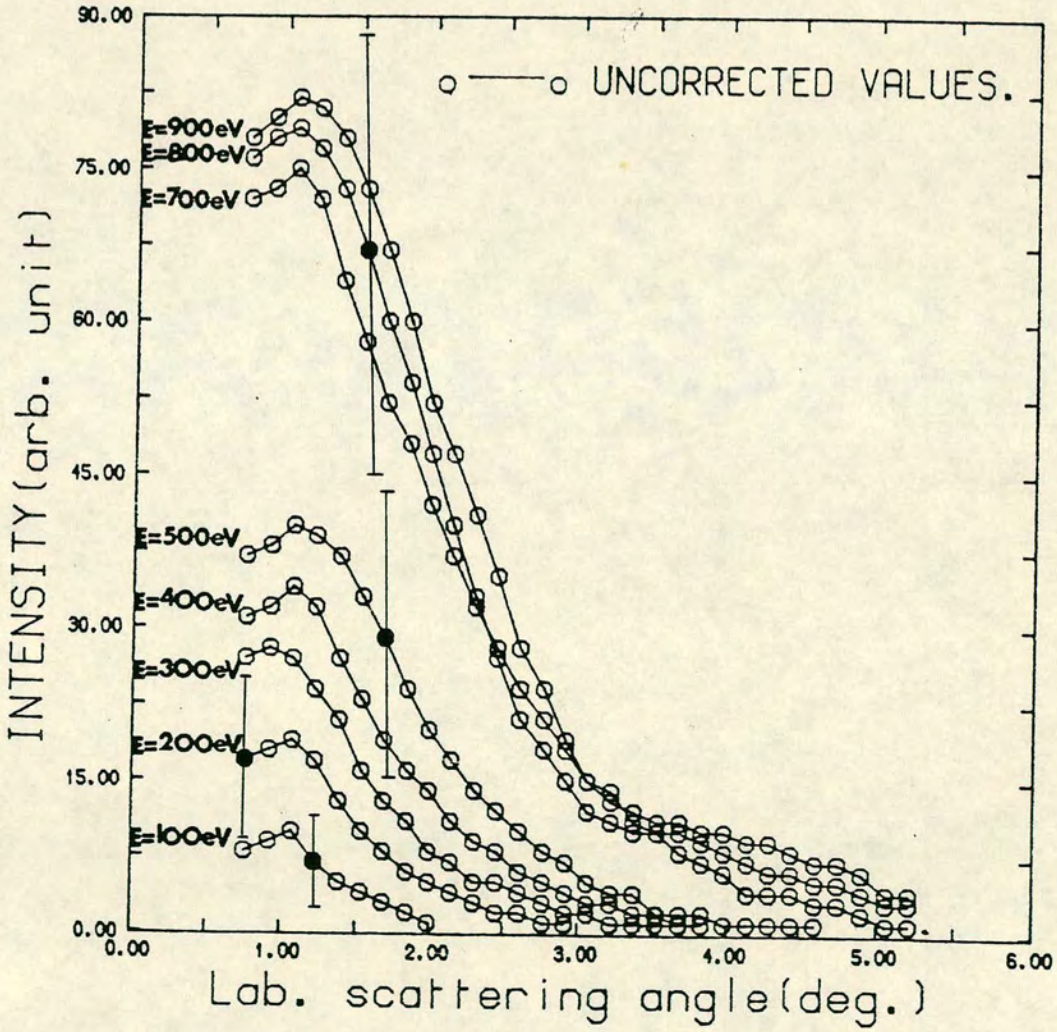
UNCORRECTED VALUES.
E=900eV
E=800eV
E=700eV
E=500eV
E=400eV
E=300eV
E=200eV
E=100eV
INTENSITY(arb. unit)
Lab. scattering angle(deg.)
90.00
75.00
60.00
45.00
30.00
15.00
0.00
0.00
1.00
2.00
3.00
4.00
5.00
6.00

FIG(5.2)

5.6 TREATMENT OF THE EXPERIMENTAL DATA

To make our data a comparative measurement the following treatment was carried out:

5.6.1 CORRECTION FOR REFRACTION IN THE PARTICLE DETECTOR

Following the collision the scattered ions enter a modified Pierce gun, see fig(5.3), with entrance slit arranged to allow a wide range of scattering angles, designed to produce a parallel sheet of ions. The ions are then injected vertically into a region of constant electric field and fall on to an Al_2O_3 plate (i.e in this region the scattered ions are accelerated above the kinetic energy of the beam). Secondary electrons ejected from this plate are focused to form an image of the initial scattering pattern on scintillators. The corrections were carried out as follows, see fig(5.4A): The velocities involved are, V_1 in $L_{c.z}$, and V_2 in $D_{g.s}$

$$\sin\theta/\sin\alpha = V_2/V_1 \Rightarrow \sin\alpha = (V_1/V_2) \,.\, \sin\theta \qquad (5.11)$$

$$\tan\theta_a = x \,/\, (L_{c.z} + D_{g.s}) \qquad (5.12)$$

$$\tan\theta = (x - q)/L_{c.z} \qquad (5.13)$$

$$q = D_{g.s} \,.\, \tan\alpha \qquad (5.14)$$

Using equations (5.13) & (5.14) we get,

$$\tan\theta = (x - D_{g.s} \,.\, \tan\alpha)/L_{c.z} \qquad (5.15)$$

From equation (5.11) we get,

$$\alpha = \sin^{-1}[\, (V_1/V_2) \,.\, \sin\theta] \qquad (5.16)$$

Using equations (5.15) & (5.16) we get,

$$\tan\theta = [x - D_{g.s} \cdot \tan[\sin^{-1}(V_1/V_2 \cdot \sin\theta)]] / L_{c.z} \qquad (5.17)$$

If θ is small, α is also small, then $\theta=\sin\theta=\tan\theta=$etc. Then equation (5.17) can be written as,

$$\tan\theta \simeq x/(L_{c.z} + D_{g.s} \cdot V_1/V_2)$$

$$\text{or} \quad \theta = \tan^{-1}[x/(L_{c.z} + D_{g.s} \cdot V_1/V_2)] \qquad (5.18)$$

$$V_1 = (2 \cdot E/m)^{1/2}$$

$$V_2 = [2 \cdot (E + EHT)/m]^{1/2}$$

Where E is the beam energy in eV and EHT is the acceleration voltage applied at the entrance of the detector, kept at 25keV throughout the experimental run.

$$V_1 = (2 \cdot E \times 1.602 \cdot 10^{-19} / M \times 1.66056 \cdot 10^{-27})^{1/2}$$

$$V_1 = 1.389 \cdot 10^4 \, (E/M)^{1/2}$$

$$\text{While} \quad V_2 = 1.389 \cdot 10^4 \, [(E + EHT)/M]^{1/2}$$

$$\text{Then} \quad V_1/V_2 = [E/(E + EHT)]^{1/2} \qquad (5.19)$$

Using equations (5.18) & (5.19) one gets,

$$\theta = \tan^{-1}[x / (L_{c.z} + D_{g.s} \cdot [E/(E + EHT)]^{1/2})] \qquad (5.20)$$

Where $L_{c.z}$ is the path length from the collision zone to the detector entrance 130cm, and $D_{g.s}$ is the distance from the Pierce gun to the centre of the Al_2O_3 plate, 20cm.

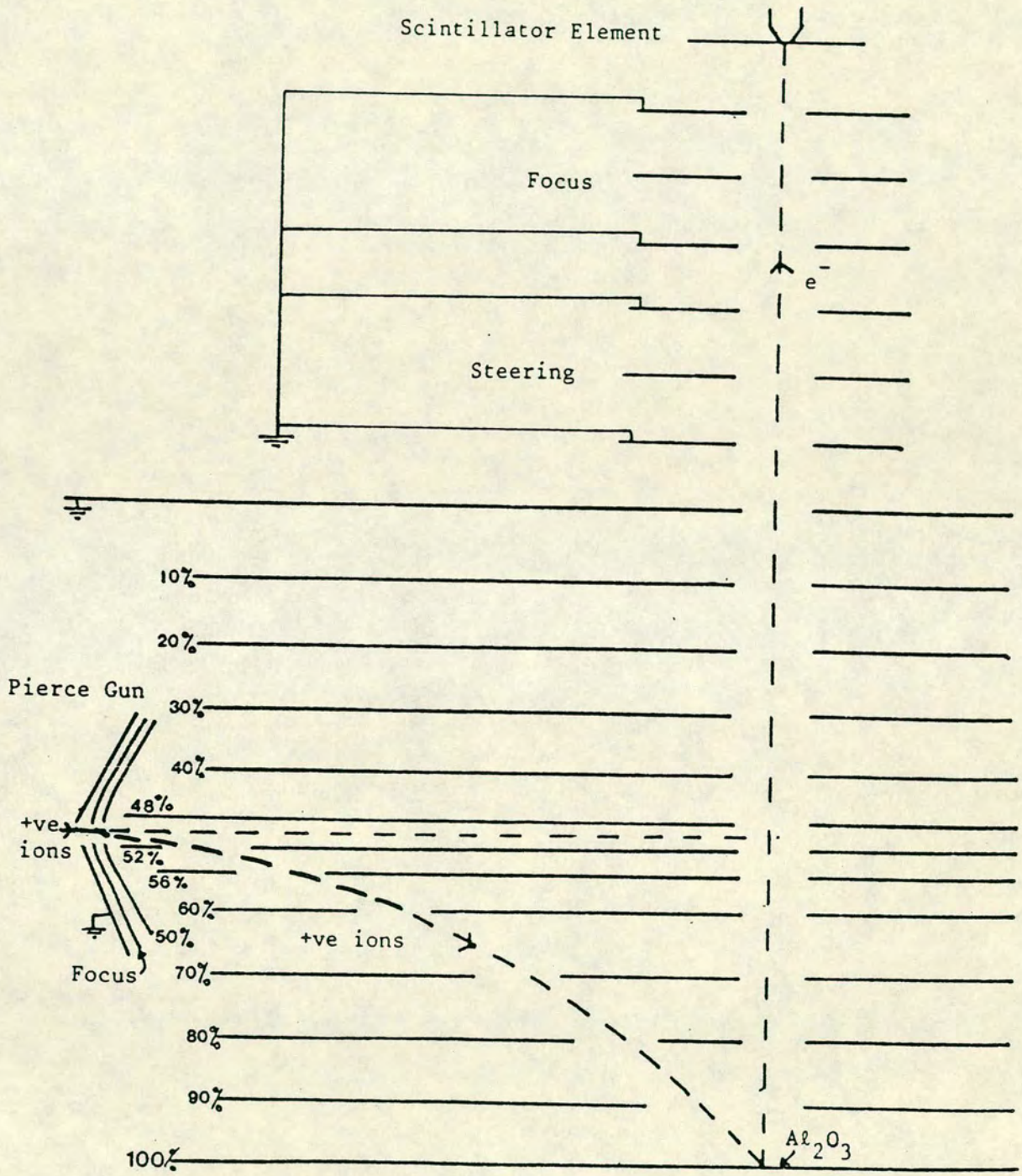

FIG(5.3) : THE ELECTROSTATIC LENS SYSTEM
OF MULTI_ANGLE PARTICLE DETECTOR

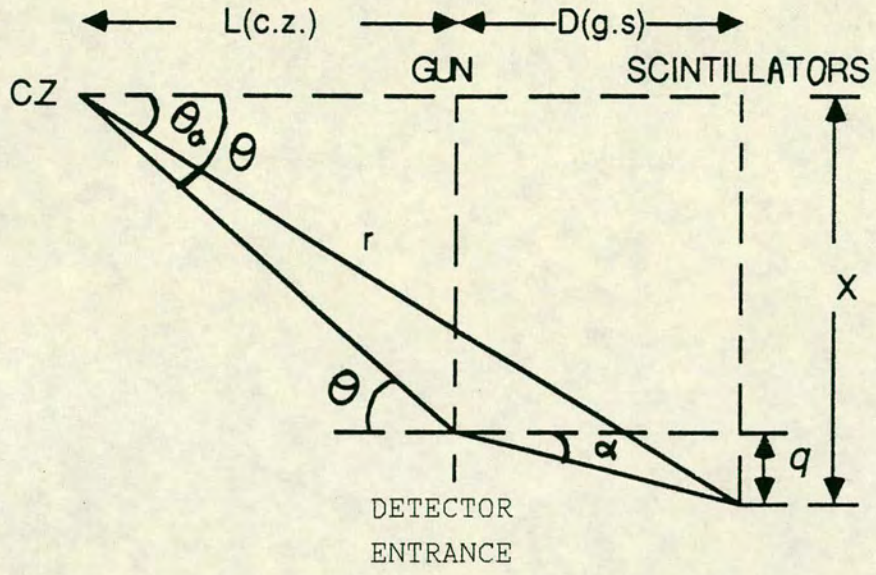

FIG(5.4A)

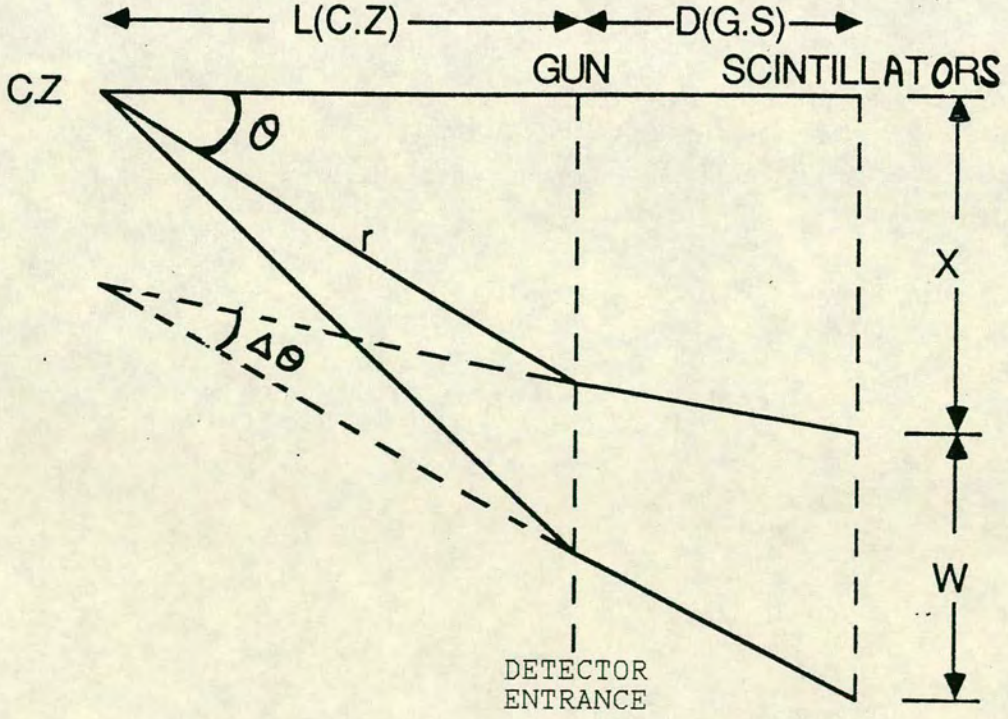

FIG(5.4B)

5.6.2 CORRECTION FOR SOLID ANGLE

Because the scintillator elements are mounted on a straight line, each scintillator subtends a different solid angle at a different position. The number of scattered particles must therefore be adjusted along the line of scintillators. The corrections were carried out as follows, see fig(5.4B).

A scintillator element of width w=2mm, located at distance x from the main beam direction, will collect scattered ions from laboratory scattering angles of,

$$\theta_1 = \tan^{-1}[\, x \,/\, (L_{c.z} + D_{g.s} \,.\, [E/(E + EHT)]^{1/2}\,)]$$

$$\text{to,}\quad \theta_2 = \tan^{-1}[\, (x + w) \,/\, (L_{c.z} + D_{g.s} \,.\, \{E/(E + EHT)]^{1/2}\,)]$$

$$\text{Hence}\quad \Delta\theta = \theta_2 - \theta_1 = \tan^{-1}[(x + w) \,/\, (L_{c.z} + D_{g.s}.[E/(E + EHT)]^{1/2})] \,.$$

$$- \tan^{-1}[x \,/\, (L_{c.z} + D_{g.s}.[E/E + EHT)]^{1/2})] \qquad (5.21)$$

The solid angle subtended = Area/r^2

$$\text{Solid angle} = (\Delta\theta \,.\, r \,.\, h)/r^2 \qquad \text{where h is the slit height}$$

$$\text{Solid angle} = (\Delta\theta \,.\, h)/r \qquad (5.23)$$

$$\text{and} \qquad r = L_{c.z}/\cos\theta \qquad (5.23)$$

Using equations (5.22) & (5.23) one gets,

$$\text{Solid angle} = \Delta\theta \,.\, h \,.\, \cos\theta/L_{c.z} \qquad (5.24)$$

From equations (5.21) & (5.24) one gets,

$$\text{Solid angle} = [(h.\cos\theta)/L_{c.z}] \,.\, [\tan^{-1}[(x + w) \,/\, (L_{c.z} + D_{g.s}\,[E/(E + EHT)]^{1/2})]$$

$$- \tan^{-1}[x \,/\, (L_{c.z} + D_{g.s}\,[E/(E + EHT)]^{1/2}\,)]] \qquad (5.25)$$

5.6.3 NORMALIZATION

The data require to be normalized for the sensitivity of each scintillator element and the photomultipliers connected to it as well as for the efficiencies of the fiber_optic connections.

The instrumental correction to the data was obtained by heating a tungsten wire of 3cm long and 0.025mm diameter, coated with potassium chloride. The tungsten wire was fixed on the axis of a stainless steel cylinder by spot welding to hypodermic needle at each end. The cylinder had a horizontal slit of 2mm wide and long enough to provide a fan of equal ion intensities to cover the whole scintillators assembly line. The cylinder is mounted on top of a "periscope", see fig(5.5), to level the slit with the entrance slit of the multi_angle particle detector. The correction stages mentioned above are shown in fig(5.6A,B) for 600eV. The corrected values of the rest of energies are shown in fig(5.7).

5.6.4 CORRECTION FOR ANGULAR RESOLUTION

The experimental data which are plotted in reduced coordinates ρ against τ, in fig(5.8), show obvious falloff at small angles. This behaviour is due to deterioration of the angular resolution as θ approaches zero[56]. This is expected when the rectangular slit (detector entrance) intercepts the conical distribution of scattered ions from the collision zone, resulting in decreasing (worsening) the angular resolution.

The corrected values of reduced cross section, fig(5.9,5.10), were obtained by using a form of mathematical correction given by:

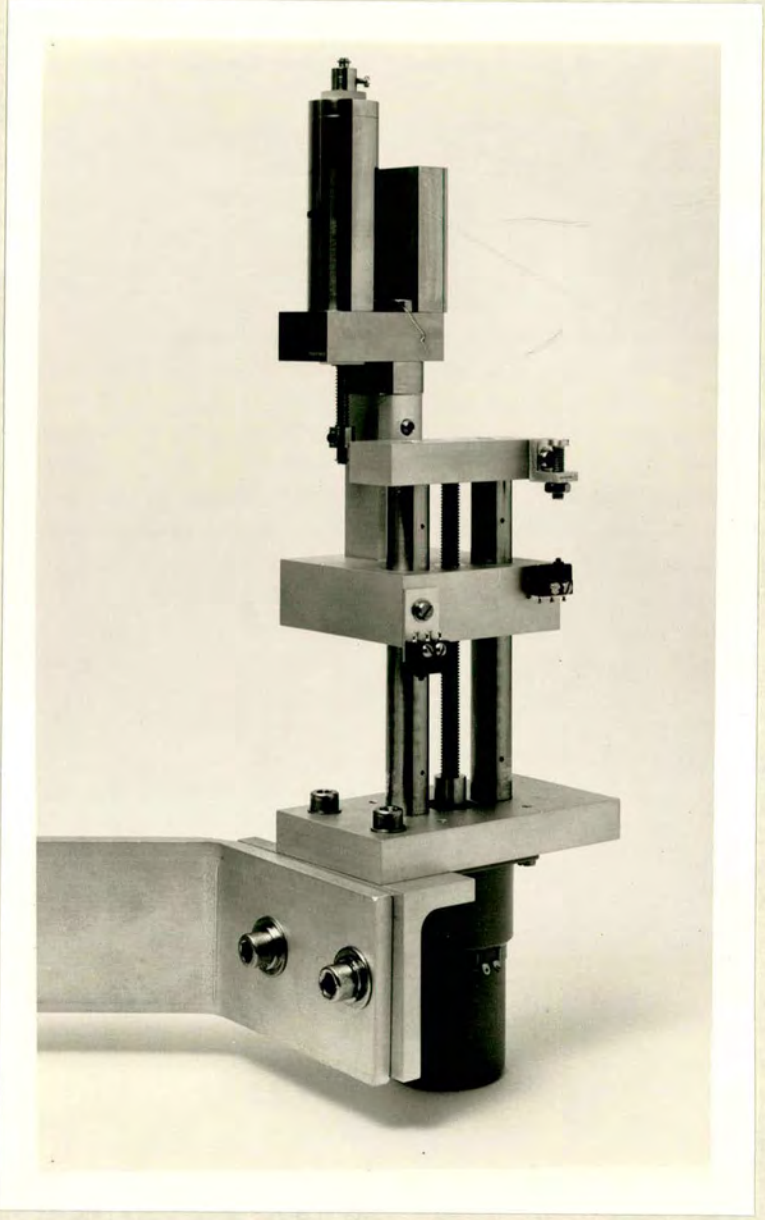

FIG(5.5): Photograph showing the periscope which is located at the c.z . and on top of it the cylinder containing a tungsten wire used in normalizing and calibrating the particle detector.

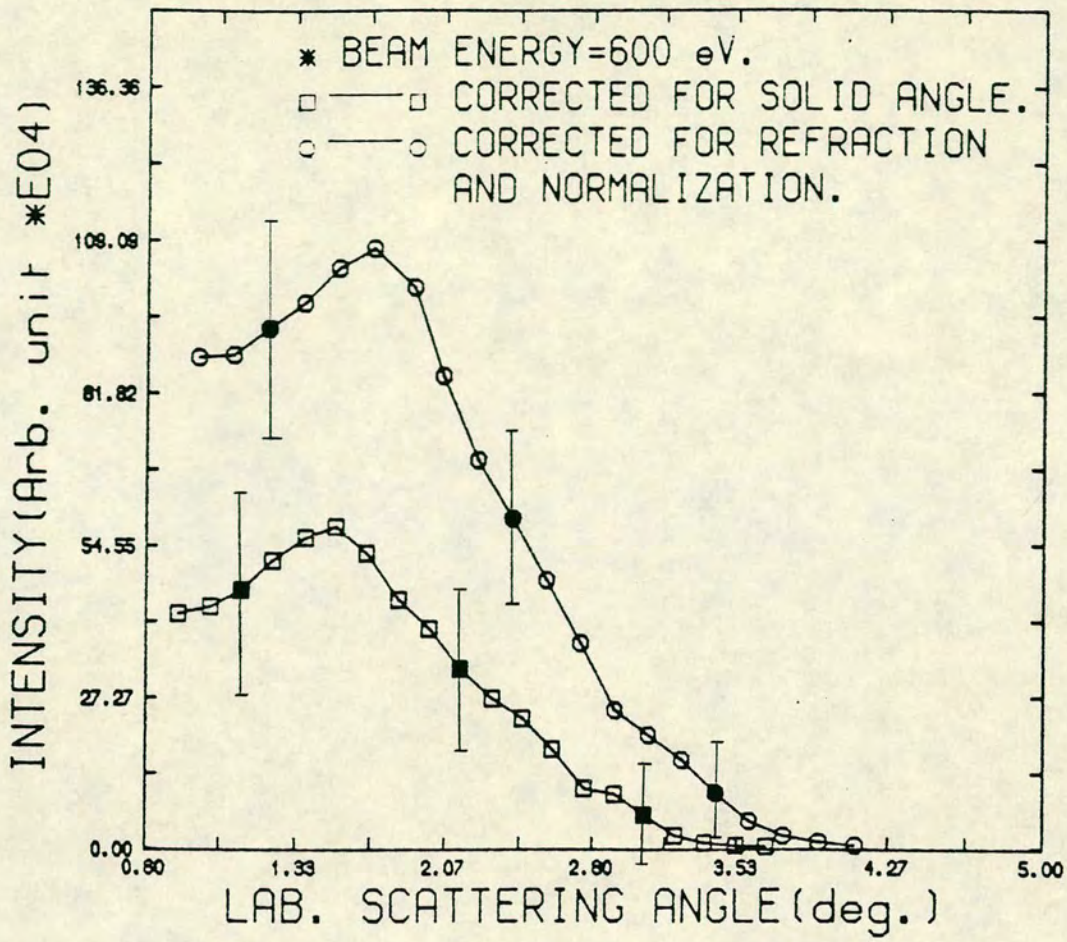

FIG(5.6A)

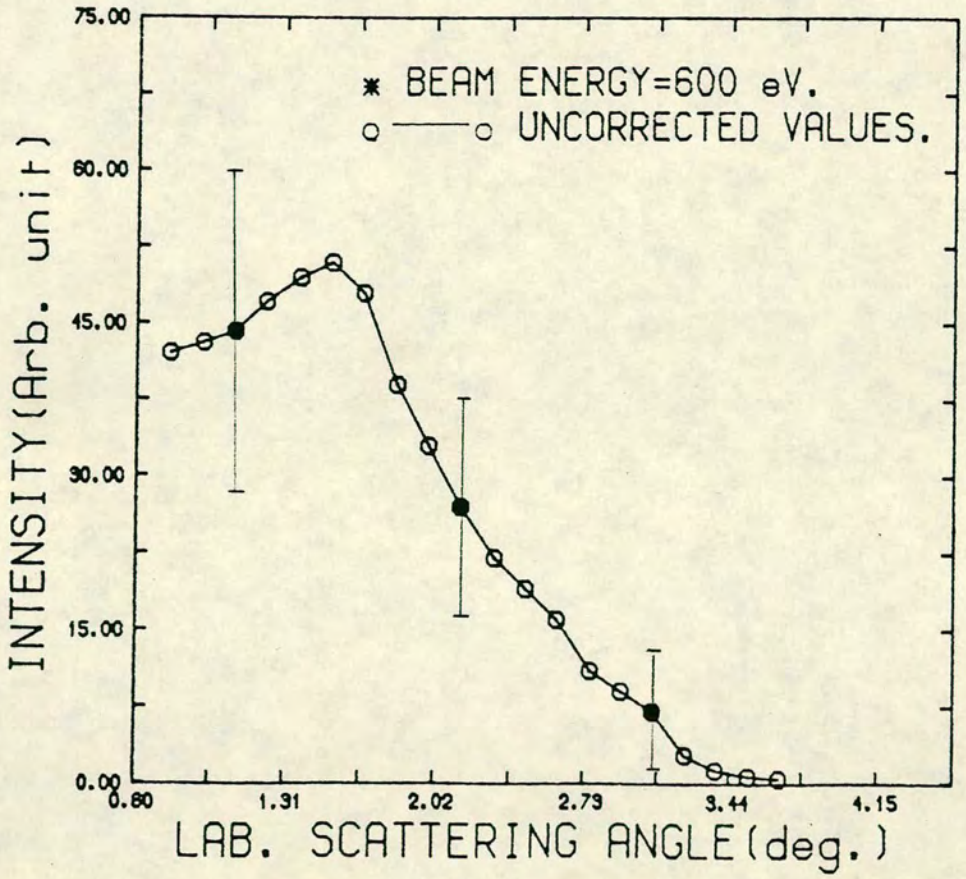

FIG(5.6B)

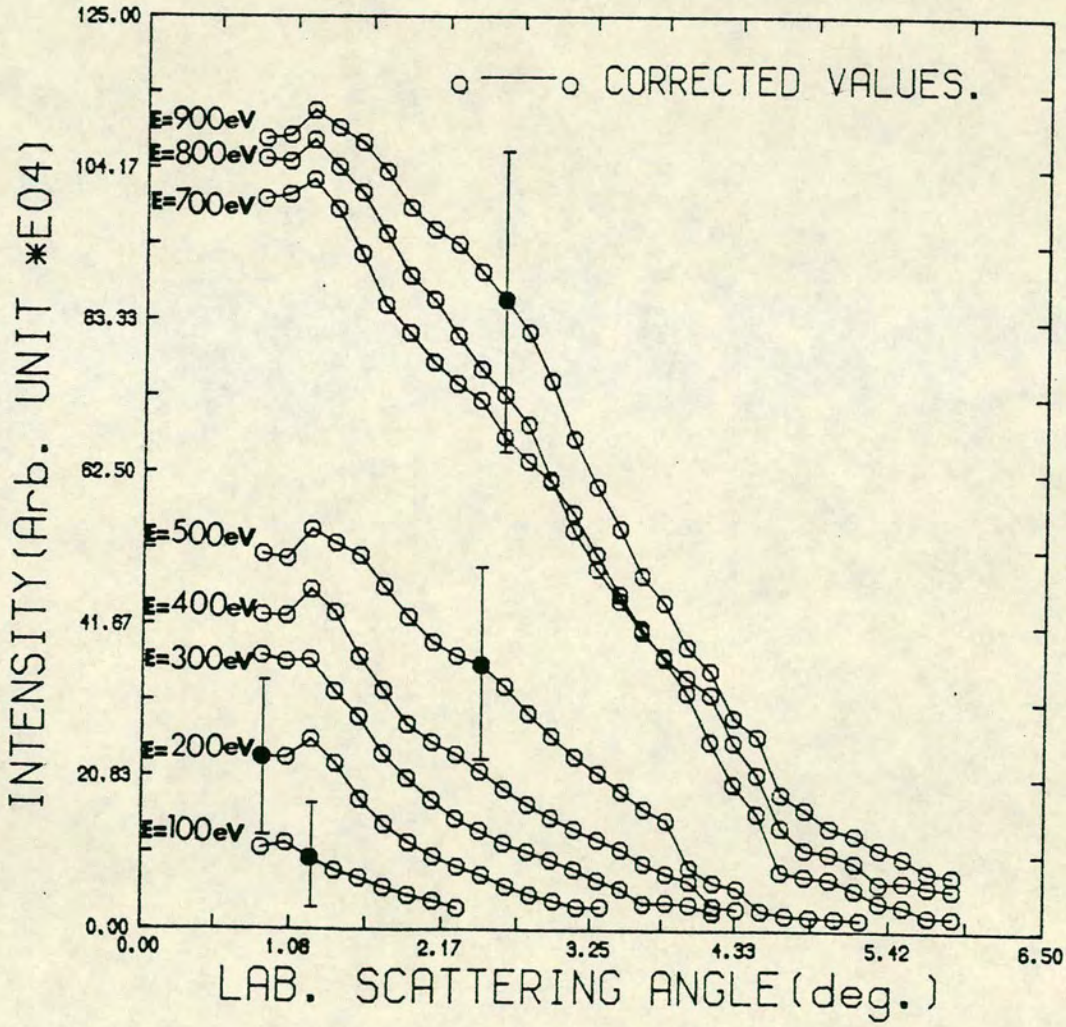
125.00
104.17
83.33
62.50
41.67
20.83
0.00
INTENSITY(Arb. UNIT *E04)
o——o CORRECTED VALUES.
E=900eV
E=800eV
E=700eV
E=500eV
E=400eV
E=300eV
E=200eV
E=100eV
0.00
1.08
2.17
3.25
4.33
5.42
6.50
LAB. SCATTERING ANGLE(deg.)

FIG(5.7)

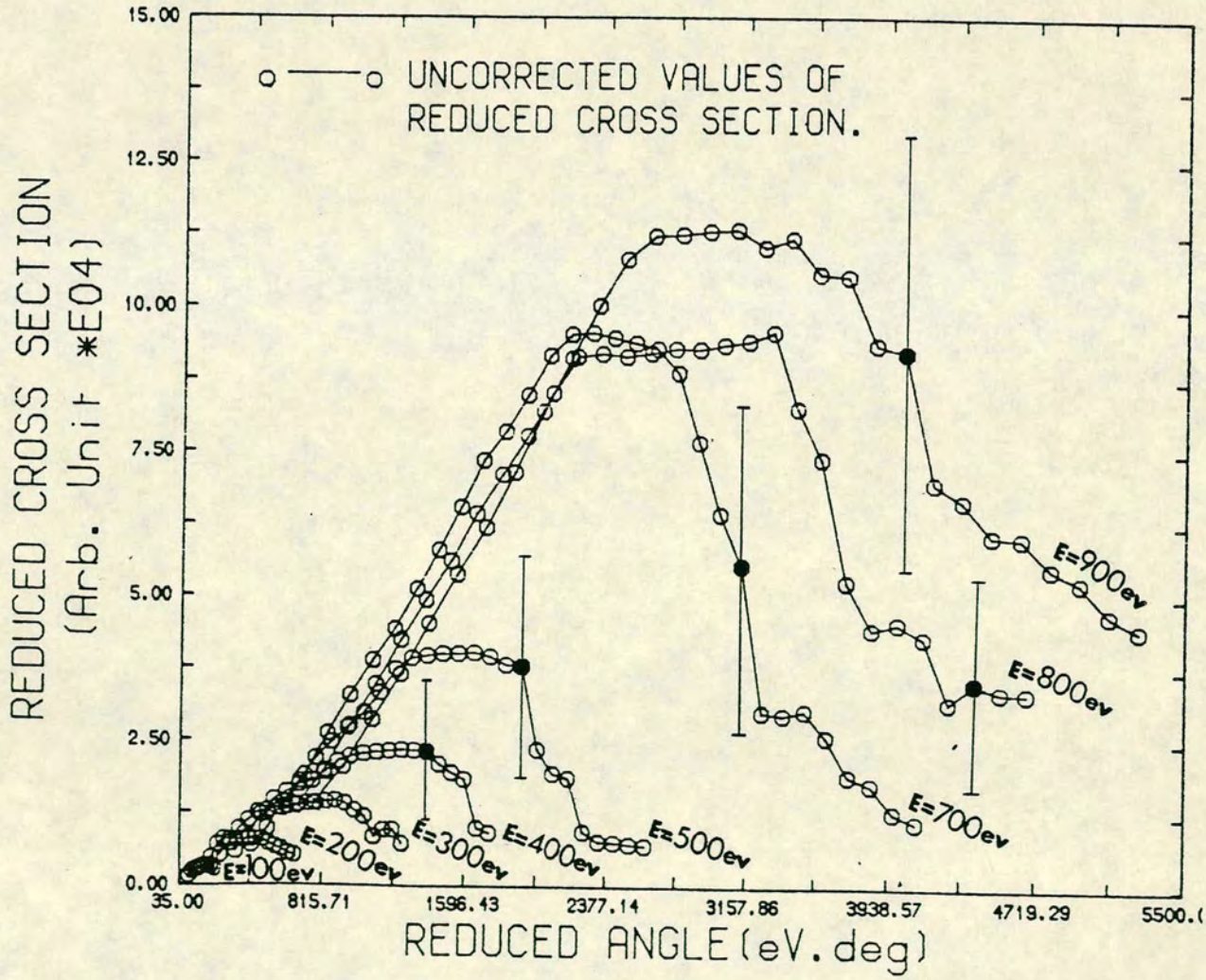
UNCORRECTED VALUES OF
REDUCED CROSS SECTION.
REDUCED CROSS SECTION
(Arb. Unit *E04)
REDUCED ANGLE(eV.deg)
15.00
12.50
10.00
7.50
5.00
2.50
0.00
35.00
815.71
1596.43
2377.14
3157.86
3938.57
4719.29
E=100ev
E=200ev
E=300ev
E=400ev
E=500ev
E=700ev
E=800ev
E=900ev

FIG(5.8)

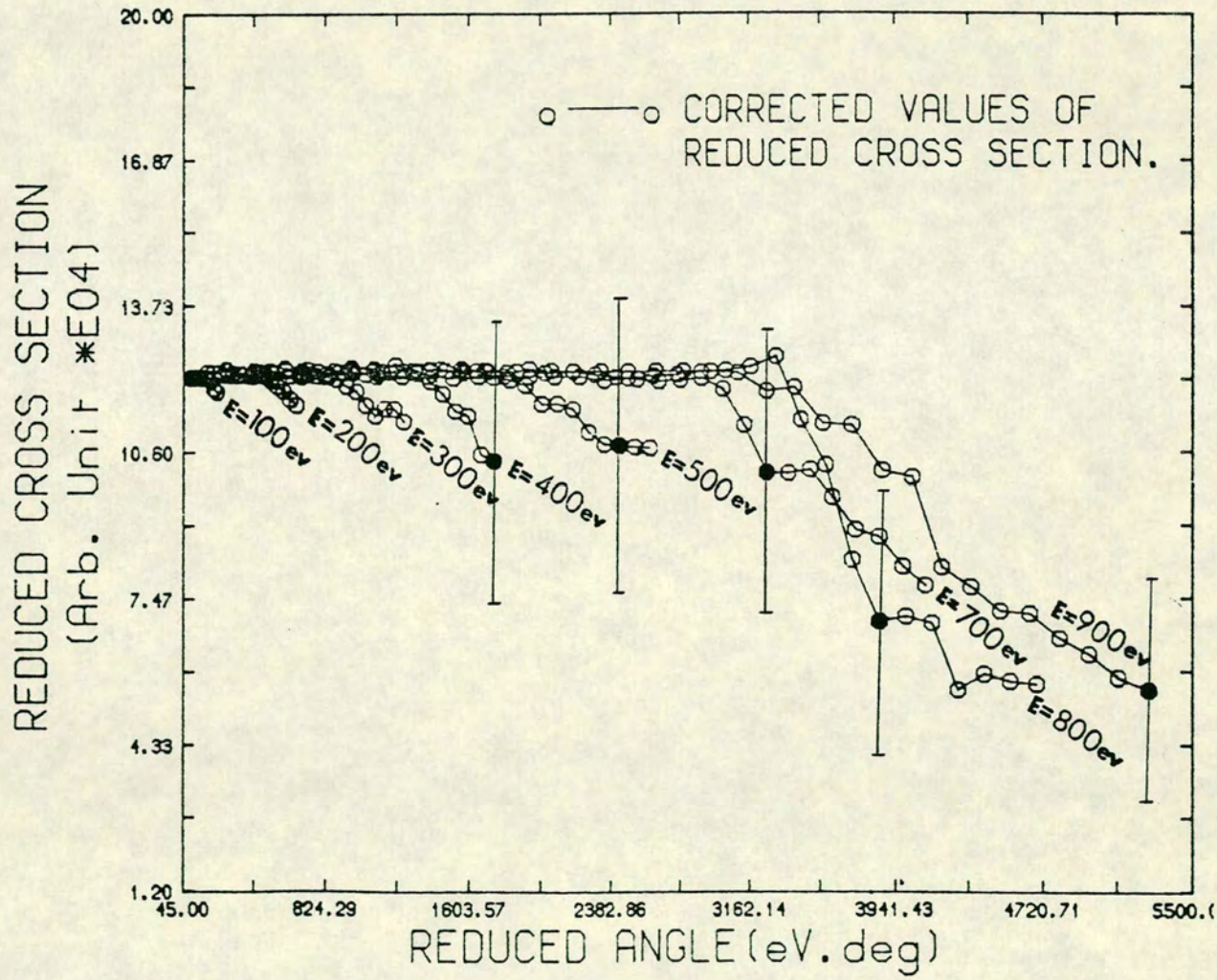
20.00
16.87
13.73
10.60
7.47
4.33
1.20
REDUCED CROSS SECTION
(Arb. Unit *E04)
o——o CORRECTED VALUES OF
REDUCED CROSS SECTION.
E=100ev
E=200ev
E=300ev
E=400ev
E=500ev
E=700ev
E=800ev
E=900ev
45.00
824.29
1603.57
2382.86
3162.14
3941.43
4720.71
5500.(
REDUCED ANGLE(eV.deg)

FIG(5.9)

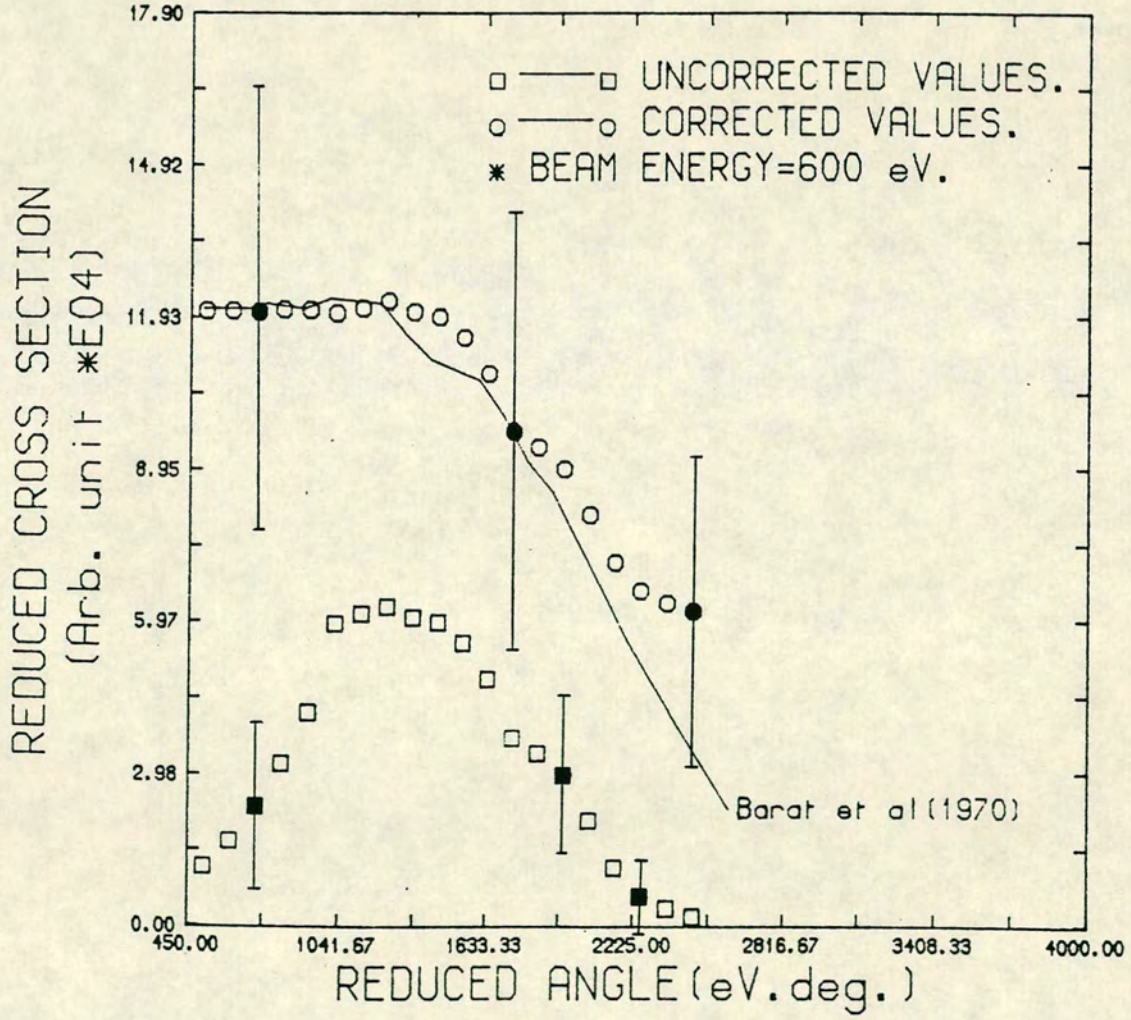
UNCORRECTED VALUES.
CORRECTED VALUES.
BEAM ENERGY=600 eV.
Barat et al(1970)
REDUCED CROSS SECTION
(Arb. unit *E04)
REDUCED ANGLE(eV.deg.)
17.90
14.92
11.93
8.95
5.97
2.98
0.00
450.00
1041.67
1633.33
2225.00
2816.67
3408.33
4000.00

FIG(5.10)

$$\text{Log}\rho_0(\tau,E) = \text{Log}\rho(\tau,E_j) + (B.E_j)/\tau - N + \text{Log}C_{Ej} \qquad (5.26)$$

where $\rho_0(\tau,E)$ is the corrected values of reduced cross section, $\rho(\tau,E_j)$ is the uncorrected value of reduced cross section, B is the correction factor, which takes the value of θ at $\rho_{max.}$, C_{Ej} is an arbitrary factor, varying with the energies (i.e for N energies, $C_{Ej},\ldots,C_{EN}$), and N is the sensitivity factor, limited by the difference between $\text{Log}\rho_{max.}$ and the corrected values. The values of $\log\rho_0(\tau,E)$ was fitted by a polynomial expansion function given by,

$$\text{Log}\rho_0(\tau,E) = a_0 + a_1.\tau + a_2.\tau^2 \qquad \text{where } a_0 \simeq \rho(\tau_{\text{at largest angle}},E)$$

5.6.5 CONVERSION TO C.M SYSTEM

The collision between a particle moving with respect to the laboratory and a particle initially fixed with respect to the laboratory is usually decribed in term of the laboratory system. To reduce and simplifiy the kinematics of the collision from two_particle problem to a one_particle problem, the laboratory energy, scattering angle and angular differential cross section were transferred to the center_of_mass system. Several reviews have considered this conversion[59,60,61], and appropriate algorithms have been selected from these as necessary .

The corrected values of reduced cross sections were read from a file and a Chebyshev polynomial (degree 10) was fitted to allow interpolation between the data points. Then the integral of equation (5.9) was performed to calculate the impact parameter and the deflection function using NAG library routine D01AGF. The results were written to a file and are shown in fig(5.11). The interaction

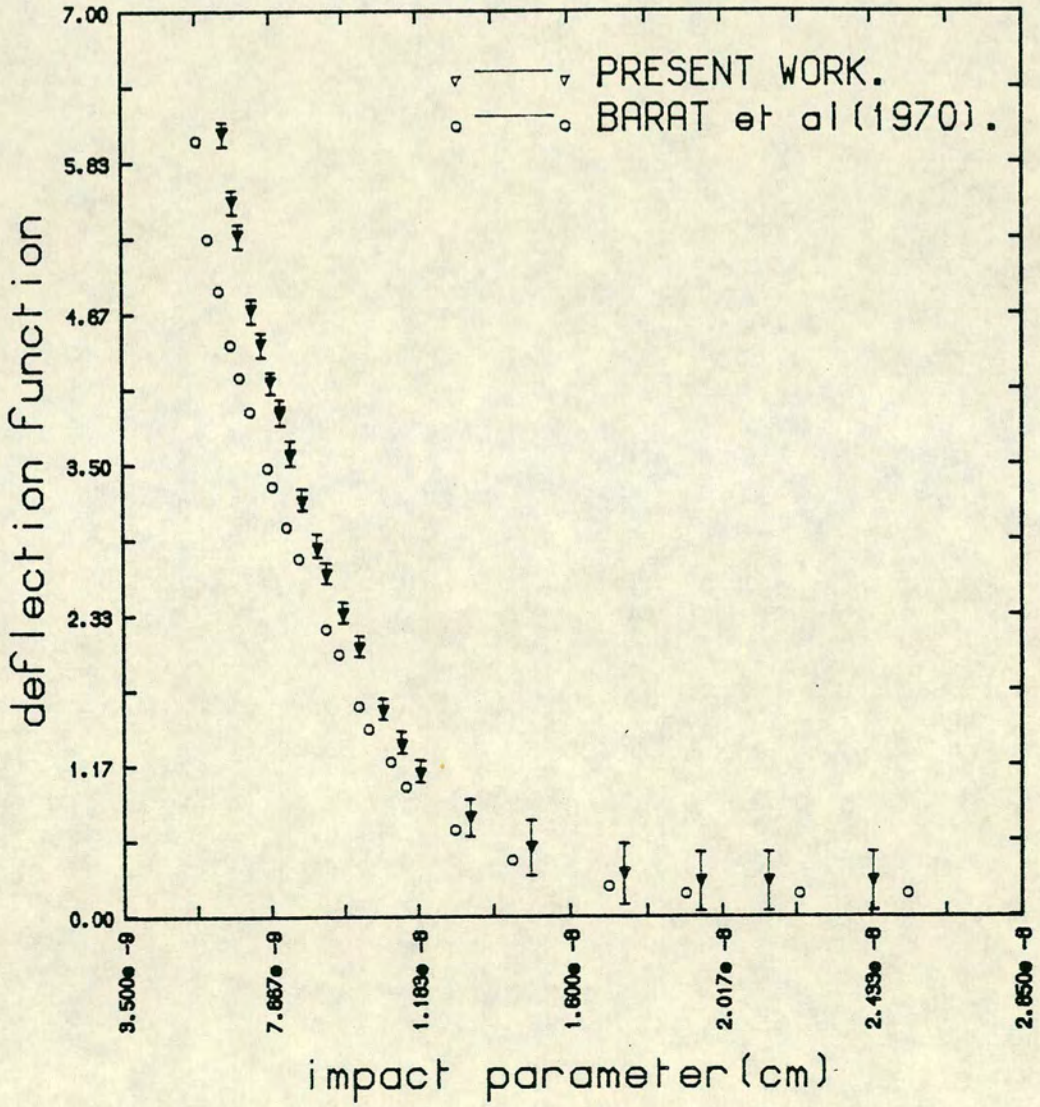
PRESENT WORK.
BARAT et al(1970).
deflection function
impact parameter(cm)
7.00
5.83
4.67
3.50
2.33
1.17
0.00
9.500e -9
7.667e -9
1.183e -8
1.600e -8
2.017e -8
2.433e -8
2.850e -8

FIG(5.11)

potential was calculated by carrying out the integration of equation (5.10). The deflection function was read from the file and fitted to a Chebyshev polynomial (degree 10) to allow for interpolation. Then the evaluation of the integral was performed by NAG library routine D01AGE. The result is shown in fig(5.12).

In obtaining the interaction potential for elastic processes, the collisions were assumed to be purely elastic; however the reduced cross sections showed a pronounced drop at large angles, which we attributed to the onset of some inelastic processes. The bumps seen on the reduced cross section in the region of large angles must be caused by some perturbing forces[56]. These become effective at the distance of closest approach because the radial motion of the nuclei is slowest at this point and thus the time available for the perturbing forces to act is longer.

Our values of reduced cross sections $\rho(\tau,E)$ at 600eV were compared with data extracted from Barat et al(1970)[62]. The agreement is good in the region of pure elastic scattering (small scattering angles), as shown in fig(5.10). Then the values of reduced cross section from Barat et al work were processed to calculate the deflection function and impact parameter in the same method used in processing our data. The comparison with our data showed reasonable agreement at large impact parameter but as $b(\tau)$ decreases and the deflection function becomes progressively more positive the drift between the compared values increases as shown in fig(5.11). The interaction potential was calculated for Barat data and compared with our interaction potential. The comparison showed

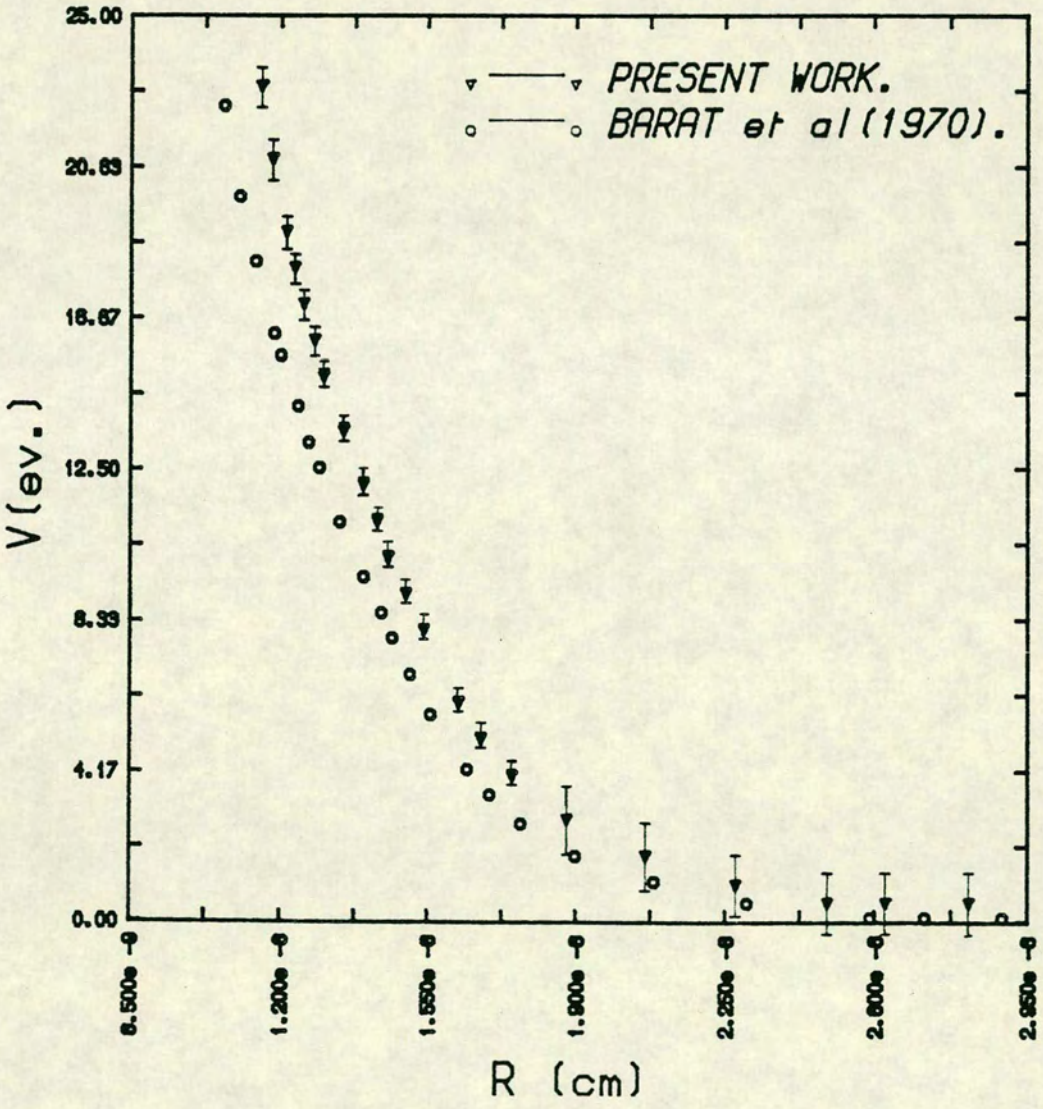
PRESENT WORK.
BARAT et al (1970).
V(ev.)
R (cm)
25.00
20.83
16.67
12.50
8.33
4.17
0.00
8.500e-0
1.200e-0
1.550e-0
1.900e-0
2.250e-0
2.600e-0
2.950e-0

FIG(5.12)

almost similar behaviour noticed between the deflection function and the impact parameter, with obvious increasing the influence of the repulsive force as the internuclear distance decreases, as shown in fig(5.12).

Chapter 6
COINCIDENCE TECHNIQUE

Until the beginning of the 1970's experimental work was largely restricted to the determination of collision cross_sections, and measurements of the polarization of light emitted from the radiative decay of excited states. But in the past few years much work has been channeled on refining methods to reach the ideal experiment which gives a clear picture of the collision dynamics. The coincidence technique is regarded as one of these refining methods and a very new generation of studying the collision dynamics.

6.1 OBJECTIVE

The objective of this work is to study the evolution of the electron configuration (excitation), during ion_molecule collisions. This type of study requires the coincident detection of a photon emitted from an excited state of a molecule formed in the collision and of an exit particle (ion) as a function of the final scattering angle. This scheme links a spectroscopic level of details concerning the transition with the dynamical information available from the scattering angle.

6.2 HISTORICAL REMARKS

It is quite interesting to note the important improvements in the coincidence technique which came in the early 1960's, when Fedorenko and co_workers[63,64] and Everhart and co_workers[65,66], constructed their coincidence apparatus. Based on a simultaneous determination of the emission angles of the scattered particles, the new technique made it possible to measure the charge states of the two scattered particles in the same collision event. This allowed a more complete mapping of the collision event than did the earlier techniques .

The early coincidence studies were restricted to rare gas ion_atom collisions in symmetric combinations such as $Ne^{+}\rightarrow$ Ne[67,68], $Kr^{+}\rightarrow$ Kr[69] and $Ar^{+}\rightarrow$ Ar. These observations published between 1965_1968, marked a turning point in the study of ion_atom collisions. The data revealed very valuable detailed information about the charge states of the two particles involved in the collision. This new information gave the inspiration to the molecular_orbital model and the starting signal to a series of inner shell excitation studies in various ion_atom collision systems.

In 1970 Afrosimov and co_workers[70,71], went farther in improving the technique by installing two ion spectrometers in their coincidence apparatus, allowing a simultaneous determination of all three kinetic energies E_0, E_1 and E_2 . Thus,

$$Q = E_0 - (E_1+E_2)$$

where E_0, E_1 and E_2 are the kinetic energy of the incident, scattered

and recoil particles respectively, Q is the inelastic energy loss.

Q also represent the total excitation energy of the collision system, thus

$$Q = U + T_e + \Sigma_j h\nu_j$$

where U is the ionisation potential of the electron, T_e is the kinetic energy of the electron and $h\nu_j$ is the energy of the j_{th} photon.

6.3 ADVANTAGES OF THE TECHNIQUE

(1) Energy analysis methods such as time of flight techniques are limited in resolution and are frequently unable to distinguish individual quantum channels, and in general do not approach the optical spectroscopy in resolution.

(2) Eliminates any contribution to the signal arising from cascade population of the excited states. Only ion_photon pairs arising from the same excitation event are correlated in time and therefore can contribute to the real coincidence signal.

(3) Distinguishes unambiguously between the molecular target and ion projectile excitation.

(4) Optical polarization measurements in coincidence with scattered particles can give information on the orientation (alignment) of the excited states produced in the collision.

(5) The ability of recording the fluorescence wavelength, the scattered angle and the arrival time simultaneously, which serves to determine the exit channels and the characteristic nature of the collision via information from differential and emission cross_sections.

6.4 APPARATUS

Measurements of this type are experimentally challenging, because at least four major areas of technique have to be brought to a high degree of perfection and then combined so that they all

work simultaneously over observation times of many hours. These areas, fig(6.1), are:

(i) Ion beam.

(ii) Target beam.

(iii) Optical system.

(iv) Multi_angle particle detector.

(i) Ion beam:

The plasma ion source produces a He^+ beam of intensity 2_2.5 μA, depending on source operating conditions (see chapter 3). The ions are then extracted and focused through a spherical energy analyser. A series of lenses then focuses and transports the beam to the collision region to yield a ribbon beam of 0.3x10mm in cross_ section.

(ii) Target beam:

The target beam is generated by a pulsed nozzle and then a skimmer arrangement collimates a beam of 0.3x10mm in cross_section. To obtain 10% attenuation of the ion beam a target density of ~0.3 $.10^{17}$ $mol.cm^{-3}$ is required. This beam intensity has been produced using up to 8 bar gas_line pressure at pulse rates of up to 45Hz and a nozzle open time of 1.5ms.

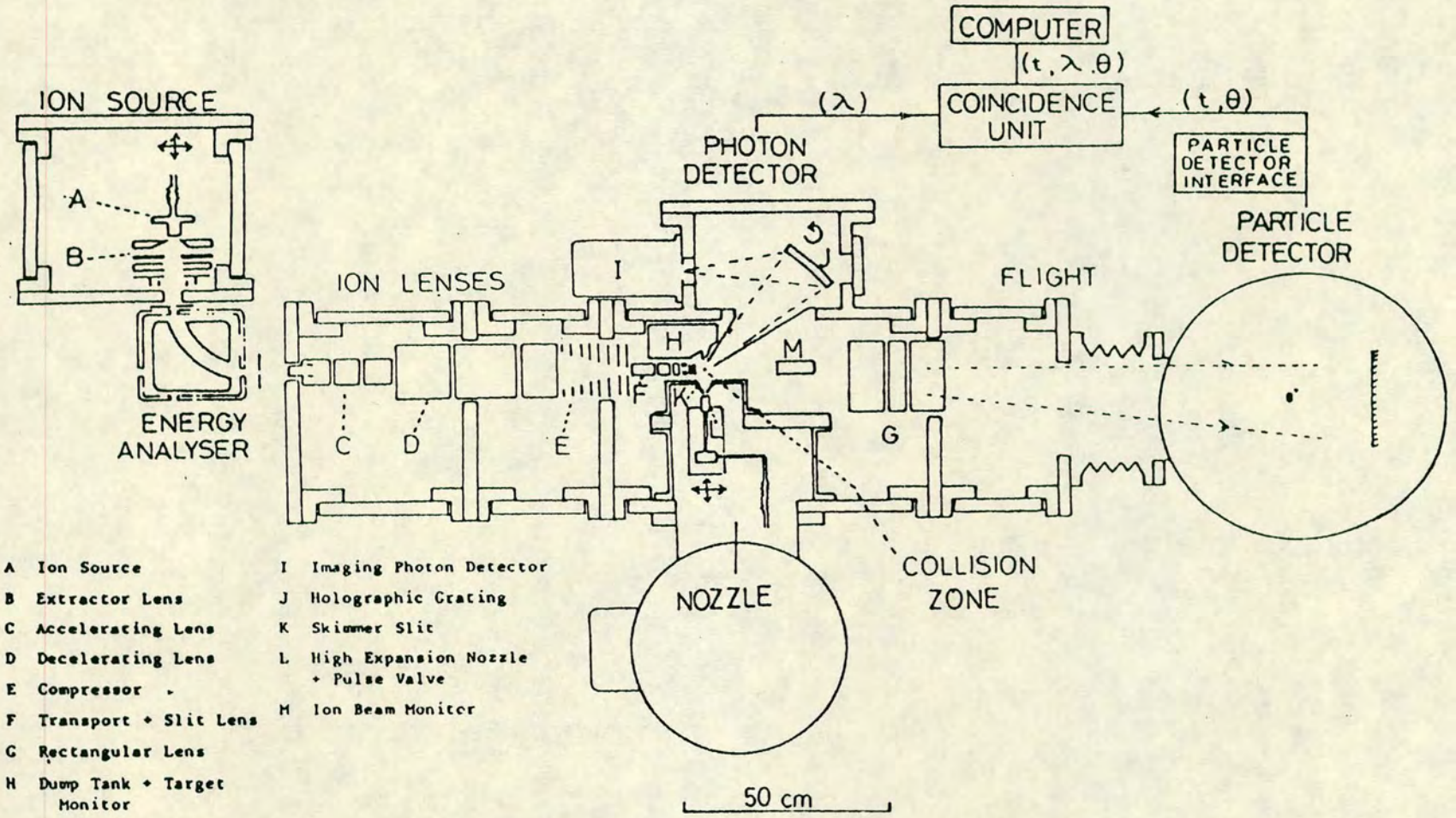

FIG(6.1): Schematic diagram of the experimental setup.

(iii) Optical system:

The photons which are emitted from the collision volume (0.3x0.3x10mm), are focused and dispersed by an f/2 concave holographic grating (1484 grooves/mm), on to an imaging photon detector (I.P.D). Photon fluxes between 60_100 per second have been observed from He^{+}(900eV) → N_2 system, due to transition of $N_2C\ ^3\pi_u$ → $N_2B\ ^3\pi_u$[72] with wavelength of 337.1nm (lifetime 40ns.). The optical system provides a wavelength resolution of better than 1nm.

(iv) Multi_angle particle detector:

This detector uses a novel optical fibre technique (see chapter 4), with an angular resolution of ~0.1° over a range of 8°. This detector is interfaced to a mini_computer PDP_11 for data collection purposes.

6.5 FEASIBILITY CALCULATIONS

The feasibility calculation was carried out to get information about some statistical considerations which limit the experiment and to find ways of improving the performance and establish a satisfactory operation with some usefully controlled parameters.

Consider the counting rates and statistics of the experiment, defining relevant quantities as follows :

I = Beam flux (particle.s^{-1}.cm^{-2})

V = Volume of the collision zone (cm^{-3})

n = Target gas density (particle.cm^{-3})

q = Photon detection efficiency (including solid angle factor)

N = Production rate of excited molecular states (s^{-1})

Γ_s=Probability of a scattered ion being detected in the particle detector

Γ_{ph} = Probability of a photon being detected in the I.P.D

N_s = Count rate of the scattered ions at θ (c/s)

N_{ph} = Photon count rate (c/s)

T = Total running time to accumulate a spectrum

The number of ions and photons that will be counted in a channel i are:

$$N_s(\theta) = \Gamma_s \cdot N \qquad (6.1)$$

and $$N_{ph} = \Gamma_{ph}.N = I \cdot n \cdot v \cdot q \cdot \sigma_i(Tot.) \qquad (6.2)$$

where σ_i(Tot.) is the total cross_section for emission of radiation in channel i. Suppose that the real coincidences are restricted to a range Δt and superimposed on a background of accidental coincidences arising from the detection of ion_photon pairs resulting from different excitation events.

The rate of real coincidence is,

$$C_{real} = \Gamma_s .\Gamma_{ph} \cdot N$$

$$= I \cdot n \cdot v \cdot q \cdot \eta \cdot \Delta r \cdot \sigma_i(\theta) \qquad (6.3)$$

where η is the particle detection efficiency, Δr is the solid angle subtended by a detector element and $\sigma_i(\theta)$ is the differential cross_section of channel i.

Equation (6.2) can be written as ,

$$N_{ph}/\sigma_i(Tot.) = I \cdot n \cdot v \cdot q \qquad (6.4)$$

Using equations (6.4) & (6.3) one gets ,

$$C_{real} = N_{ph}/\sigma_i(Tot.) \cdot \eta \cdot \Delta r \cdot \sigma_i(\theta) \qquad (6.5)$$

For total experimental time T, equation (6.5) can be written as ,

$$C_{real} \cdot T = \Gamma_s \cdot \Gamma_{ph} \cdot N \cdot T$$

$$= N_{ph}/\sigma_i(Tot.) \cdot \eta \cdot \Delta r \cdot \sigma_i(\theta) \cdot T \qquad (6.6)$$

Equation (6.6) can be written as ,

$$\sigma_i(\theta) = (C_{real} \cdot T \cdot \sigma_i(Tot)) / (N_{ph} \cdot T \cdot \eta \cdot \Delta r)$$

$$\text{or} \quad \sigma_i(\theta)/\sigma_i(Tot) = C_{real} / (N_{ph} \cdot \eta \cdot \Delta r) \qquad (6.7)$$

The rate of accidental coincidence in the time interval Δt is,

$$C_{acc.} = N_s \cdot N_{ph} \cdot \Delta t \qquad (6.8)$$

Using equation (6.1) & (6.2) one gets,

$$C_{acc.} = (\Gamma_s \cdot N) (\Gamma_{ph} \cdot N) \cdot \Delta t$$

$$= \Gamma_s \cdot \Gamma_{ph} \cdot N^2 \cdot \Delta t \qquad (6.9)$$

The total accidental events are,

$$C_{acc.} \cdot T = \Gamma_s \cdot \Gamma_{ph} \cdot N^2 \cdot \Delta t \cdot T \qquad (6.10)$$

Let us assume that the poissonian statistics apply[73]. One can obtain the following expression for the standard deviation of the real coincidence signal,

$$\sigma = [\ (C_{real} .T) + (C_{acc.} .T)\ ]^{1/2}$$

Using equations (6.6) & (6.10) one gets,

$$\sigma = [\Gamma_s .\Gamma_{ph} .N .T + \Gamma_s .\Gamma_{ph} .N^2 .\Delta t .T]^{1/2} \qquad (6.11)$$

Now the signal to noise ratio can be written as,

$$S_{signal}/S_{noise} = (\Gamma_s.\Gamma_{ph}.N.T) / [\Gamma_s.\Gamma_{ph}.N.T + \Gamma_s.\Gamma_{ph}.N^2.\Delta t.T]^{1/2} \qquad (6.12)$$

$$= (\Gamma_s.\Gamma_{ph}.N.T) / [(\Gamma_s.\Gamma_{ph}.N.T)^{1/2} (1 + N.\Delta t)^{1/2}]$$

$$S_{signal}/S_{noise} = [(\Gamma_s .\Gamma_{ph} .N .T) / (1 + N. \Delta t)]^{1/2} \qquad (6.13)$$

For convenience let us call the signal/noise, the quality factor Q,

$$Q = S_{signal}/S_{noise}$$

The real coincidence signal can be determined from equation (6.5) by guessing some factors,

$$C_{real} = \sigma_i(\theta)/\sigma_i(Tot.) \cdot N_{ph} \cdot \eta \cdot \Delta r$$

From the data of Dowek et al[72] the ratio $\sigma_i(\theta)$ /σ_i(Tot.) can be estimated as ~100. Δr is the solid angle subtended by a detector element and η is the detector efficiency, in our case $\Delta r \simeq 10^{-4}$ steradian and $\eta \simeq 0.6$. The above equation becomes,

$$C_{real} = N_{ph} \cdot 6.10^{-3} \quad c/s \qquad (6.14)$$

Let assume the observed photon rate is ~100c/s, then one gets,

$$C_{real} \simeq 6.10^{-1} \quad c/s$$

Let us assume the rate of the scattered ions at angle θ of 2.1° (1890 eV.deg), is ~290c/s. Then by using equation (6.8) one gets

$$C_{acc.} \simeq 2.9 .10^{4} \cdot \Delta t$$

Δt one can assume roughly to be equal to the lifetime of $C\ ^3\pi_u$ state, which is 40ns, then,

$$C_{acc.} \simeq 11.6 .10^{-4} \quad c/s$$

Now from the estimated values of the real and accidental rates of coincidence, the quality factor Q can be estimated using equation(6.12)

$$Q = (C_{real} \cdot T^{1/2}) / (C_{real} + C_{acc.})^{1/2} \qquad (6.15)$$

$$Q \simeq (6.10^{-2} \cdot T^{1/2}) / (6.10^{-2} + 11.6 .10^{-4})^{1/2}$$

$$Q \simeq 0.24 \cdot T^{1/2}$$

To accumulate a reasonable quality of coincidence spectrum, the experiment need to run for at least half a day and that makes the quality factor Q,

$$Q \simeq 50$$

In our case the quality factor Q after 21.8 hours run should be

$$Q \simeq 68$$

From the equations derived in this section one can point out some limitations of this kind of coincidence experiments. In fact one has to compromise between improving the real coincidence rate and achieving optimum performance. Looking at equation (6.3) one may ask, since $C_{real} \propto N$, why the real coincidence cannot be increased simply by increasing the production rate of the excited molecular states through increasing the target gas density and the ion beam density. The answer is, at the same time that the rate of the real coincidences increases the accidental coincidence rate which is given by equation (6.8) where $C_{acc.} \propto N^2$ will increase faster than the real coincidence rate.

There is some concern as to how far N can be increased based on the probability of some radiation emitted from the excited states being re_absorbed by ground state molecules within the interaction region before reaching the photon detector. This is known as "resonance trapping" (Moiseiwitsch and Smith 1968)[74]. This has insignificant effects in case of transitions between two excited states.

The quality of the coincidence spectrum depends very much on

the quality factor Q, which is given by equation (6.13)

$$Q = [(\Gamma_s \cdot \Gamma_{ph} \cdot N \cdot T) / (1 + N \cdot \Delta t)]^{1/2}$$

In case of N is small (i.e $N \cdot \Delta t \ll 1$), the quality of the spectrum depends on N and T, therefore the ratio can be improved by running the experiment for longer time and increasing the rate of scattering events.

In case of N is large (i.e $N \cdot \Delta t \gg 1$), the accidental coincidence rate becomes dominant and the quality of the spectrum can be given by,

$$Q = [\ (\Gamma_s \cdot \Gamma_{ph} \cdot T) / \Delta t\ ]^{1/2}$$

Therefore the quality of the spectrum depends on increasing the running time T,as well as decreasing the time interval Δt, which can be done by narrowing the TAC opening time to decrease the accidental coincidence coming from different processes and excited states.

6.6 METHOD

Observing delayed coincidences between the inelastically scattered ions and photons from the radiative decay of the excited molecules in crossing a molecular beam with an energy selected ion beam, combines two branches. First the spectroscopic side of the fluorescence, second, the dynamical side of the scattered ions.

The spectroscopic side involves calibrating the concave holographic grating and then setting the grating to diffract the desired wavelength. In calibrating the grating a standard Hg/Zn/Cd lamp was used. The lamp shone through a glass window of 1.5cm diameter. A nylon thread of 0.3mm diameter was lowered by a 12v_DC motor positioned accurately above the collision zone and tensioned by a weight (plumb) to provide uniform reflection. The standard lines (wavelengths) of the Hg/Zn/Cd lamp are listed in table_I_. By rotating the diffraction grating about the vertical axis a good spectrum was formed with well resolved and sharply focused lines in the order listed in table_II_. From the values of the observed wavelengths and grating rotation a dispersion line was plotted, see fig(6.2). From the calibration graph, the desired wavelength ($C\ ^3\pi_u \rightarrow B\ ^3\pi_u \rightarrow$ 337.1nm), was located and the corresponding grating position found (692 steps), and set. Then the spectrum (emission data), of $He^+ \rightarrow N_2$ system for 900eV was collected and are presented in fig(6.3).

The ions which scattered at a particular angle θ_{ion} with an energy loss of $\Delta E_{C.M}$=11.1eV ($\Delta E_{lab.}$= 12.68eV[60]), represent the second branch of the technique. These ions were focused on to the

TABLE-I-

λ (nm.)	ELEMENTS	REMARKS
213.86	Zn	Strong Line
228.8	Cd	Strong Line
253.65	Hg	Weak Line
326.10	Cd	= =
328.20	Zn	Strong Line
330.26	Zn	= =
334.50	Zn	= =
340.4	Cd	= =
346.6	Cd	= =
361.5	Cd	= =
365.0	Hg	Weak Line
365.5	Hg	= =
366.3	Hg	= =
404.66	Hg	Strong Line
435.8	Hg	= =
468.0	Zn	Weak Line
472.2	Zn	= =
480.0	Cd	= =
481.05	Zn	= =
508.6	Cd	Strong Line
546.1	Hg	= =
577.0	Hg	= =
579.0	Hg	Weak Line
609.9	Cd	= =
636.2	Zn	= =
643.8	Cd	= =

TABLE -II-

λ (nm.)	GRATING ROTATION (STEPS)	PHOTON COUNTS (C/S)	ELEMENTS
340.4	704	4000	Cd
346.6	720	4080	Cd
361.5	760	4015	Cd
365.0	781	1809	Hg
366.3	794	2006	Hg
404.7	914	4086	Hg
435.8	1008	3992	Hg
468.0	1110	2508	Zn
472.2	1124	2108	Zn
480.0	1147	1283	Cd
508.6	1236	3906	Cd
546.1	1357	4101	Hg
577.0	1457	3009	Hg
579.0	1463	2766	Hg

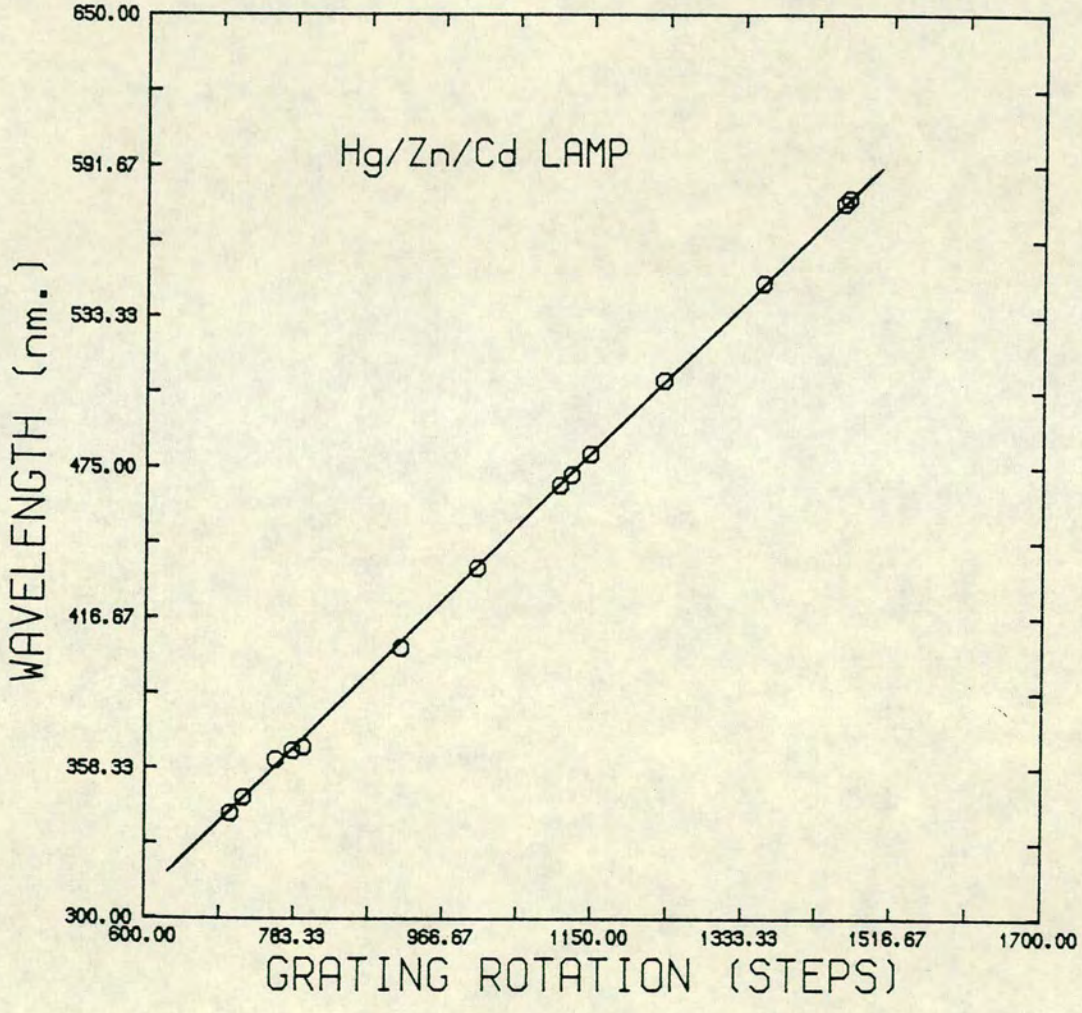

FIG(6.2): Dispersion line was used to calibrate the grating movements.

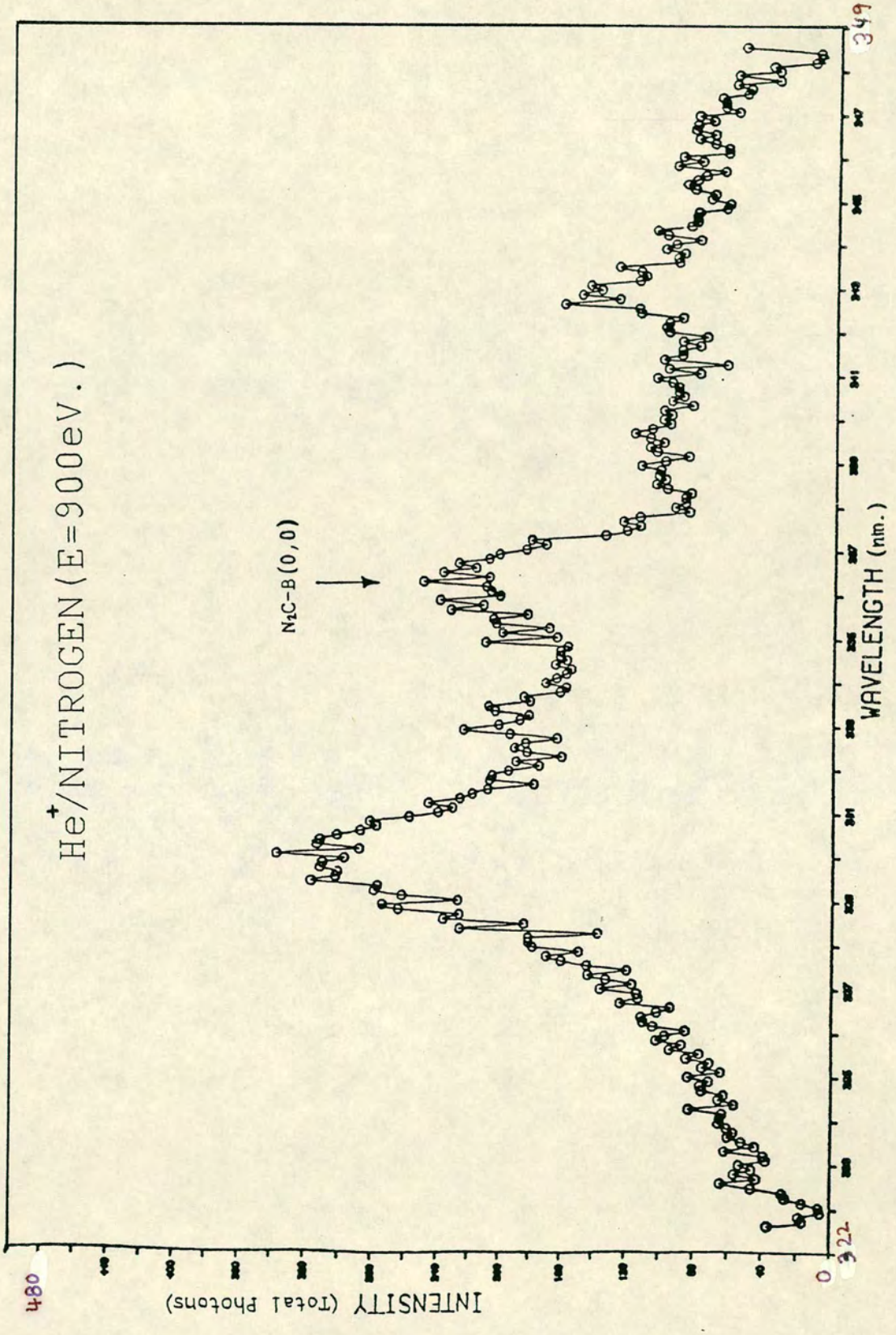

FIG(6.3): Photon emission spectrum of He^+/N_2 system.

entrance of the particle detector which uses a binary coincidence method using optical fibres to code the arrival position.

A preliminary experiment was arranged by using a single detector element (angle 2.1°), out of the 45 elements, to detect the scattered ions, and a multi_channel analyser (MCA) to record and display the coincidence events. The electronic arrangement for the experiment is shown in fig(6.4). The signals from each branch (photon side and scattered ion side), were amplified by a fast amplifier type NE4683, which is designed for use in fast timing systems, featuring very low noise of the output signal and fast risetime (less than 1.5ns), to facilitate precise timing measurements, the amplified signal coming from the particle detector was passed to a discriminator type NE4684_OCTAL of input threshold −0.02_−1V and output pulse width 6_50ns. The amplified signal from the I.P.D was fed into a constant fraction discriminator type ORTEC 473, which set the level of signal input discrimination within the range 0.05_5V. The photon pulse was suitably delayed by a delay generator type ORTEC 416A, which provided a logic pulse delay from 0.1μs to 110μs. The delay time imposed on the photons was 4.67μs to allow enough time for the ions which suffered energy loss (12.68eV) in the collisions to travel to the particle detector.

The photon timing pulse was passed to a Time_to_Amplitude Converter (TAC) type ORTEC 567, to start the ramp with input gate set on coincidence mode, and wait 5μs for the scattered ion of energy $E_{lab}-\Delta E_{lab.}$=887.32eV, after flight time 6.594μs (including 32ns the propagation delay in the electronic units), to reach the particle

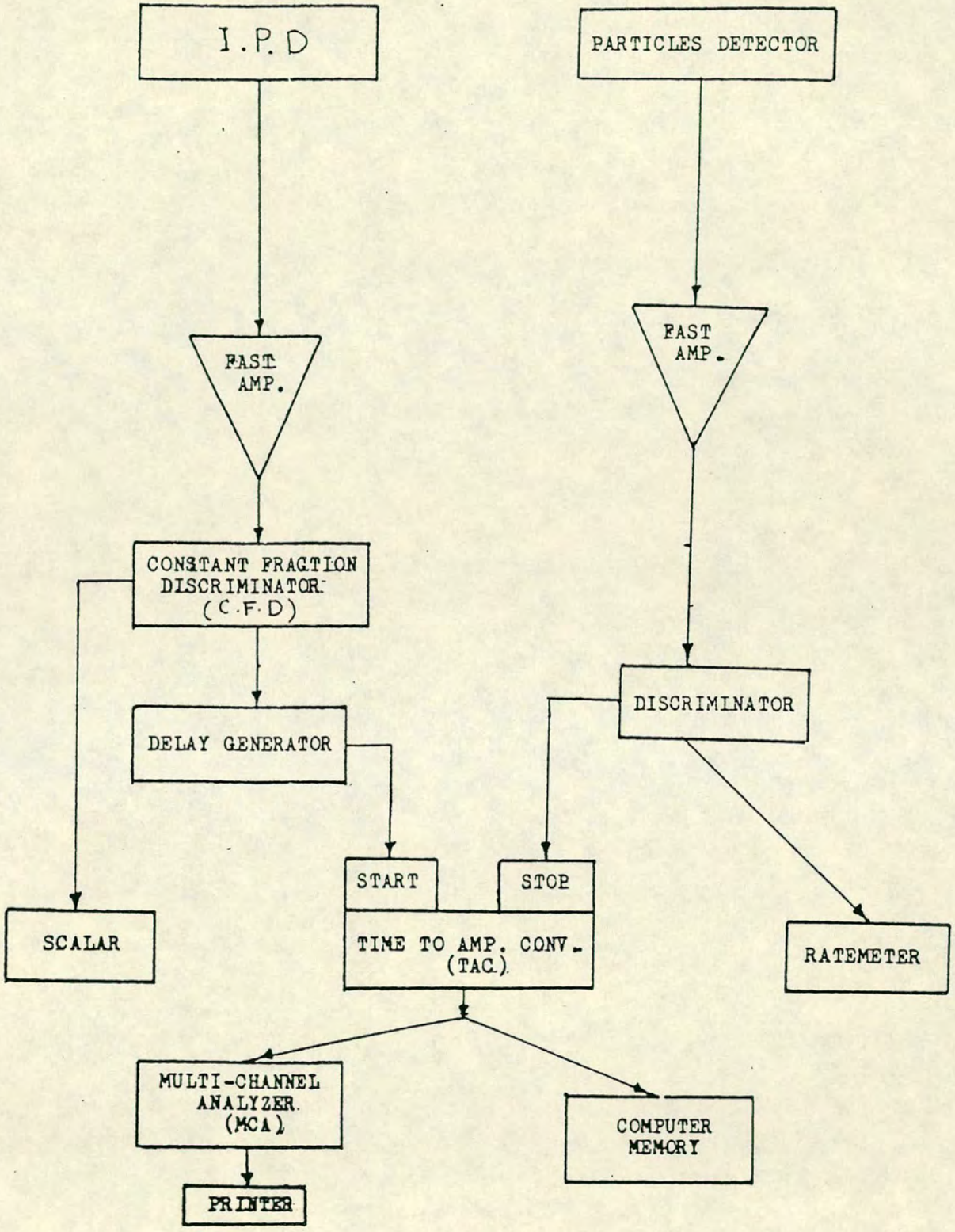

FIG(6.4): Schematic diagram of the electronics arrangement for the coincidence experiment

detector and stop the ramp (input gate of the stop circuit set on anti_coincidence mode). The start_to_stop time conversion is accomplished only after a valid start has been identified and after a stop pulse has arrived within the selected time range (5μs). The start input is disabled during the busy interval to prevent pileup. The stop input is disabled after the first accepted stop signal. The amplitude of the TAC output signal was then proportional to the time difference between start and stop pulses. A multi_channel analyser (MCA) was used to record the resulting pulse height spectrum from the TAC. The whole MCA screen of 1024 channel was set to 10μs (9.76ns per channel).

To perform the experiment which was planned and set as an ultimate objective, the multi_angle particle detector should be used to its full capacity by employing the 45 angle elements to allow a bigger range of scattering angle and processes to be investigated, as well as enhancing the signal_to_noise ratio. In order to coordinate the arriving data from all 45 angles simultaneously with emission data arriving from the I.P.D, a sophisticated software is required, which is almost ready, and a multiplexer unit, now under test, to interface the 45 angles, wavelength of the emission and the flight time to a mini_computer type PDP_11, see fig(6.5).

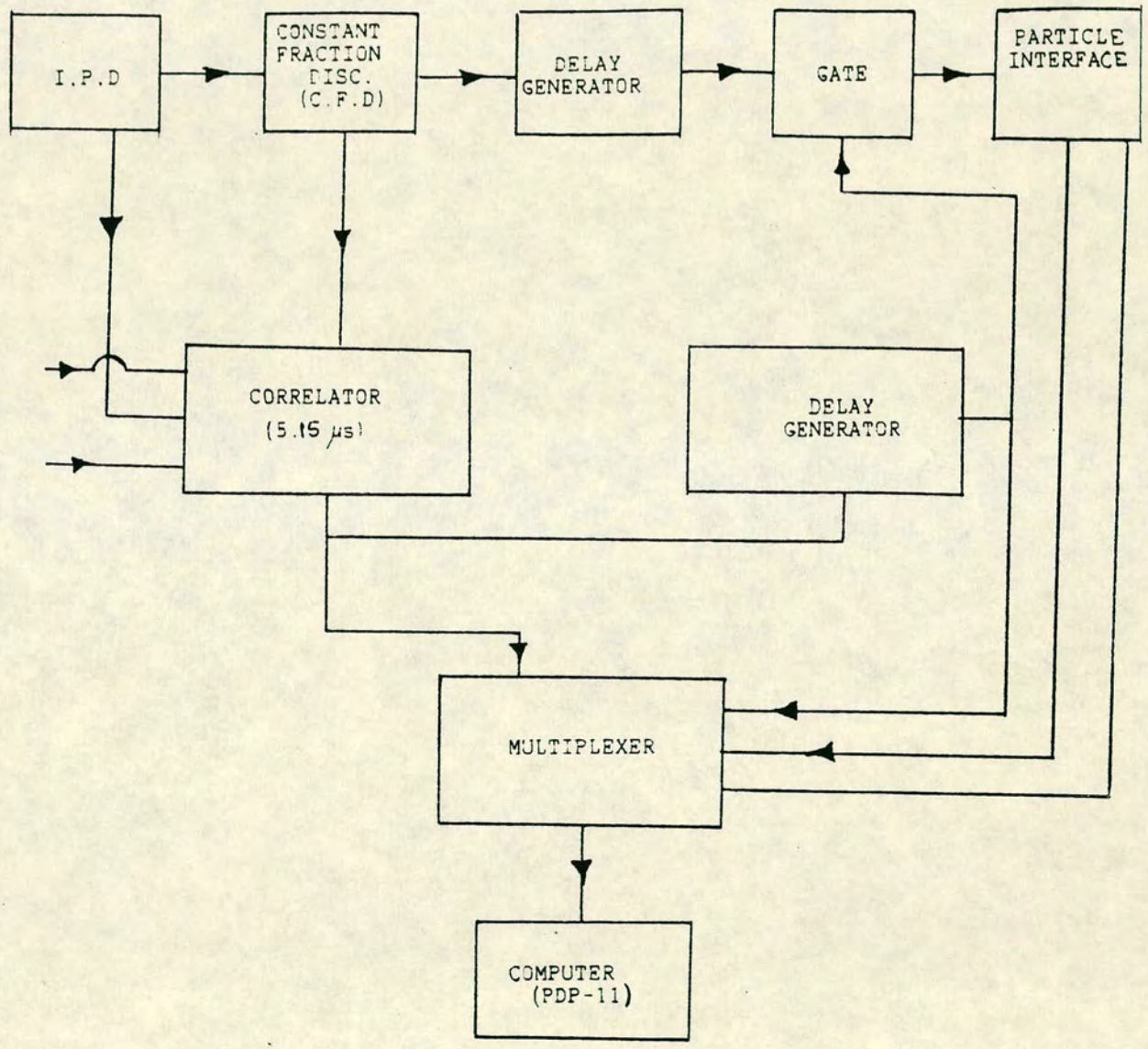

FIG(6.5): Schematic diagram of the objective electronics arrangement for the coincidence experiment.

6.7 RESULT AND DISCUSSION

Since the coincidence method provides much more detailed information about the collision process than conventional methods, it is not suprising that these experiments are far more difficult than the conventional cross_section experiments. In these experiments signals are usually weak, and long integration times must be invested before data of reasonable quality can be obtained. In some cases data collection times extending to several weeks[75], have been reported.

The coincidence spectrum which is shown in fig(6.6) represents detection of ion_photon pairs of $He^{+} \rightarrow N_2$ system, arising from real and accidental coincidence signals correlated in time, from the same and different excitation states. This data was accumulated for 21.8 hours of operation. During the experiment $6.763 \ .10^{6}$ valid starts were recorded, and the total number of scattering ions was $1.8873 \ .10^{7}$. The arrival times of the first and last correlated pairs contributing to the real coincidence were 1.913μs and 1.952μs respectively. It is obvious from the spectrum that the coincidence signal is very weak, while the background is very high.

The rate of the real coincidence signal can be determined from the spectrum,

C_{real} = Total real coincidence events / Total running time

$C_{real} = 58/7.864 \ .10^{4}$

$= 7.3 \ .10^{-4}$ c/s

From the experimental valid starts (number of total photons), one can obtain the observed photon rate as follows.

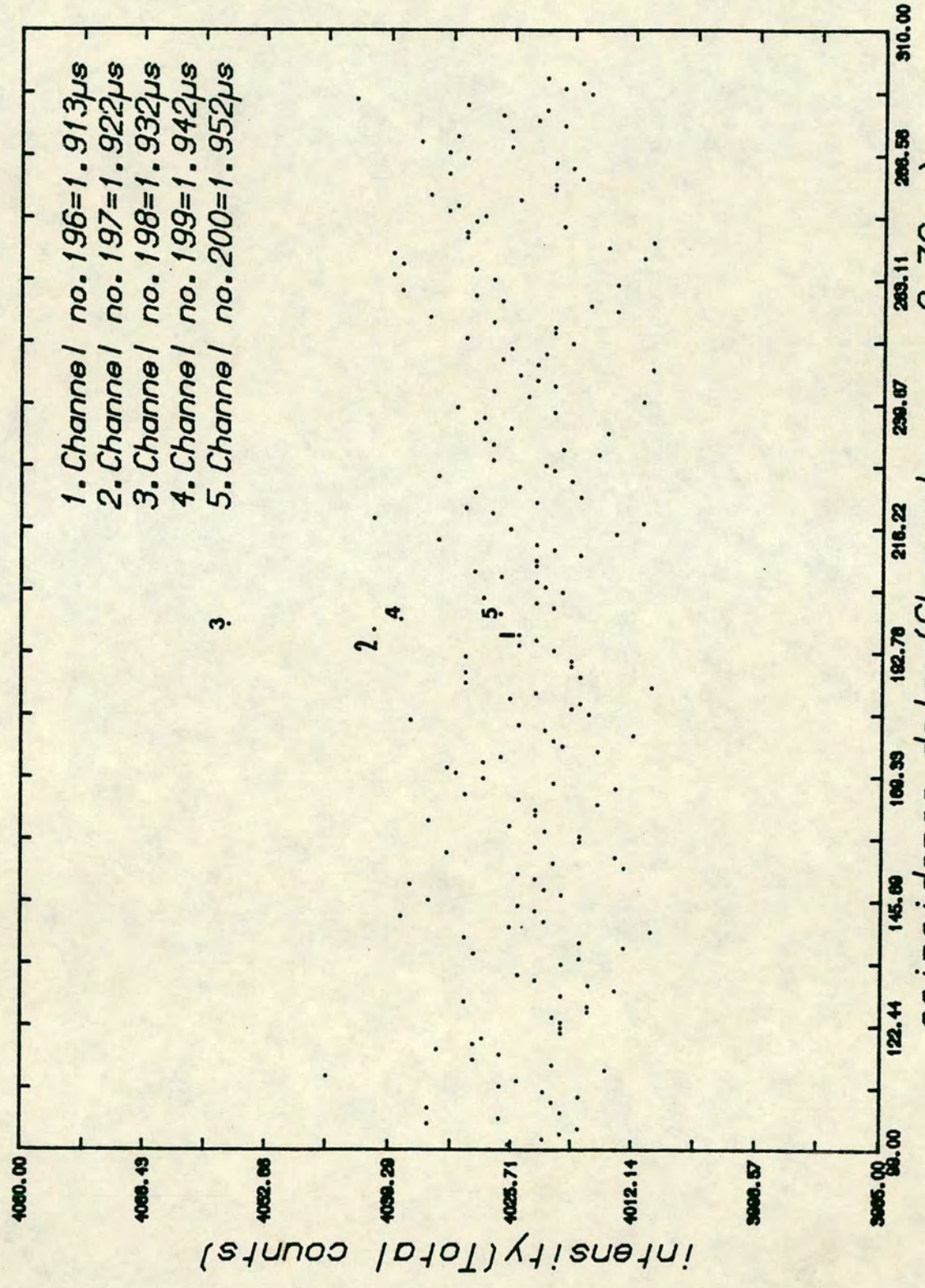

FIG(6.6): Ion_photon correlations spectrum.

N_{ph} = Valid starts / Total running time

= $6.763\ 10^6$ / $7.864\ .10^4$

= 86 c/s against background ~9c/s

From the total number of scattered ions, one can obtain the count rate of the ion as,

N_s = Total number of scattered ions / Total running time

= $1.8873\ .10^7$ / $7.864\ .10^4$

= 240 c/s against background ~120c/s

Now the accidental coincidence rate can be determined by using equation (6.8) as following,

$C_{acc.} = N_s \cdot N_{ph} \cdot \Delta t$

= $240 \times 86 \times 4\ .10^{-8}$

= $8.256\ .10^{-4}$ c/s

The quality of the coincidence spectrum (quality factor Q), can be determined from equation (6.15),

$Q = C_{real}\ T^{1/2} / (C_{real} + C_{acc.})^{1/2}$

= 5.2

The ion's time of flight can be calculated by dividing the flight path into four regions, fig(6.7), as following,

Region I :

$E_I = E_{lab.} - \Delta E_{lab.} \Rightarrow E_I = 900 - 12.68 = 887.32eV$

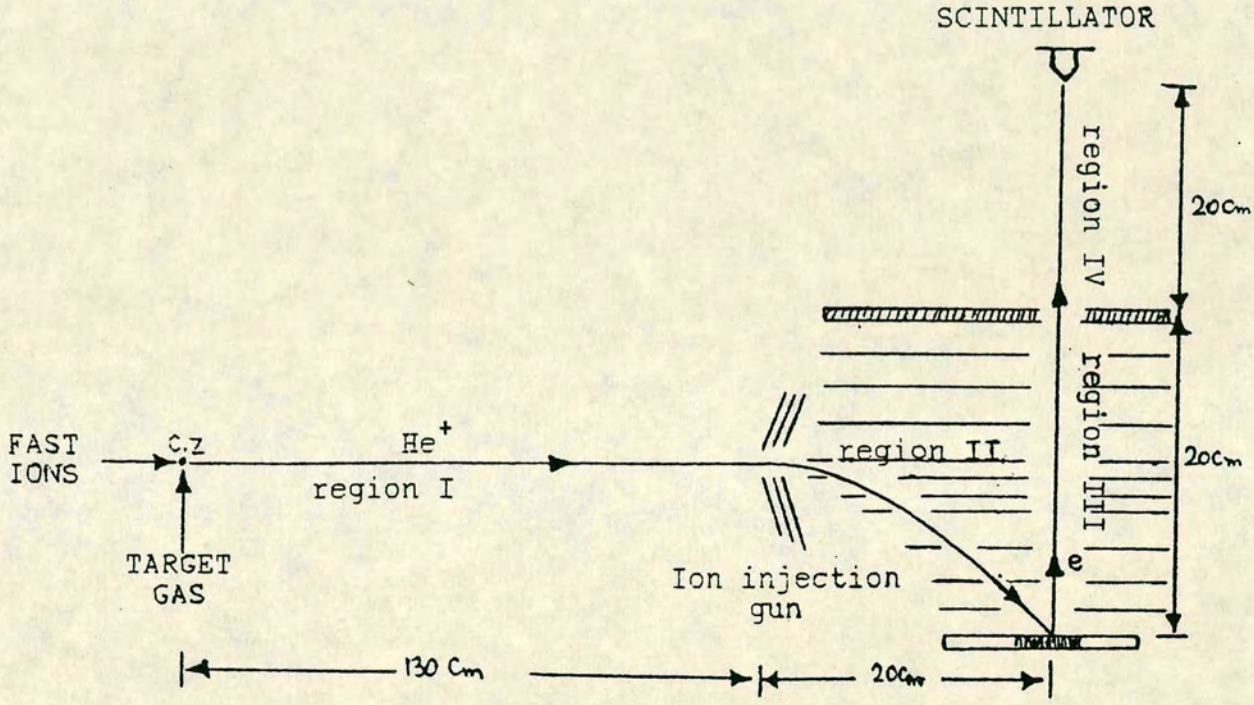

FIG(6.7): Regions of the flight of time calculations.

$$V_I = (2\ E_I/m)^{1/2}$$

$$= (2 \times 1.602 .10^{-19} \times E_I/1.66056 .10^{-27} \times M)^{1/2}$$

$$= 1.389 .10^4 (E_I/M)^{1/2} = 20.68 .10^4 \text{ m/s} \Rightarrow \text{or } V_I = 2.068 .10^7 \text{cm/s}$$

and $t_I = d_I/V_I = 130.26/2.068 .10^7$

$t_I = 6.298\mu s$

130.26cm represent the length of the flight path after angle correction.

Region II :

$$V_{II} = 1.389 .10^4 [(E_I - EHT)/M]^{1/2} \qquad \text{where EHT=25kv}$$

$$= 111.74 .10^4 \text{ m/s} \Rightarrow \text{or } V_{II} = 11.174 .10^7 \text{cm/s}$$

and $t_{II} = d_{II}/V_{II} = 20/11.174 .10^7$

$t_{II} = 0.178\mu s$

Region III :

The secondary electrons released from Al_2O_3 surface undergo acceleration upwards, towards the scintillators. The time required for the electron to reach the end of acceleration field can be found as following:

$$S = 1/2 . a . t^2$$

where a is the uniform acceleration and S is the acceleration distance.

$$a = F/m_e = e \cdot E/m_e = e \cdot V/m_e \cdot S$$

$$a = 1.602 \cdot 10^{-19} \times 5 \cdot 10^{4}/0.2 \times 9.109 \cdot 10^{-31}$$

$$= 4.39 \cdot 10^{16} \text{ m/s}^2$$

$$t^2 = 2 \cdot S/a = 2 \times 20/4.39 \cdot 10^{18}$$

$$= 9.11 \cdot 10^{-18} \text{ s}^2$$

then $t_{III} = 3.018\ 10^{-9}$ s $\Rightarrow$or $t_{III} = 3.018$ns

$$V_{III} = V_0 + a \cdot t$$

$$= a \cdot t = 4.39 \cdot 10^{18} \cdot 3.018 \cdot 10^{-9} = 13.24 \cdot 10^{9} \text{ cm/s}$$

Region IV :

The electrons emerge into a region of free of acceleration possessing velocity $13.4 \cdot 10^9$cm/s, and has to travel 20cm to reach the scintillators.

$$t_{IV} = d_{IV}/V_{IV} = 20/13.24 \cdot 10^{9}$$

$$t_{IV} = 1.51 \cdot 10^{-9} \text{ s} \Rightarrow \text{or } t_{IV} = 1.51\text{ns}$$

Now T.O.F = $t_I + t_{II} + t_{III} + t_{IV} = 6.480\mu$s.

There are two additional factors to be add to the T.O.F, first, a factor of 17mm, the distance that the ions travel inside the ion injection gun (27mm path length), before undergoing the additional acceleration, which makes 82.1ns. Second, a factor of 32ns represent the propagation delay time produced in the electronic units.

Then T.O.F (Total) = 6.480 + 0.114 = 6.594μs

The expectant location of the coincidence peak can be found as

following,

Peak location (calculated) = T.O.F − Emission time

= 6.594 − 4.73 = 1.864μs

where the emission time is equal to the lifetime of C $^3\pi_u$ + the time delay imposed on the photon signal + the propagation delay time(20ns).

From the experimental result the peak location was found at channel number 198(1.932μs). The time difference in the location is given by,

Time difference in the peak location=Experimental loca.−calculated loca.

= 1.932 − 1.864 =0.068μs

Time difference in the peak location = 68ns

It is obvious from the comparison between the experimental and expected (feasibility calculation) signal_to_noise ratio that the accidental coincidences are the dominant events a with small number of real coincidences. this could be related to the following factors:

(1) The C $^3\pi_u$ state is populated from other states by cascade leading to a larger time difference between the ion's arrival time and photon emission. This was observed by J.H.Birley[76] where the C $^3\pi_u$ of N_2 was seen to be populated by E $^3\Sigma^+_g$ state, but in general the total effect was found to be small.

(2) The coincidence window (TAC open time = 5μs) opened for a longer time than was required to accumulate the useful events (real coincidence), which increased the probability of recording accidental coincidences.

(3) The long integration time required to accumulate a reasonable quality of spectrum is probably the main disadvantage of this technique, because it is difficult to keep the experiment running for about 22 hours or more as required without any beam fluctuation, which ultimately results in spreading the useful events (real coincidences) over a wide number of channels as well as increasing the level of accidental events.

REFERENCES

1. V.W.HUGHES and H.L.Schultz, "Methods of experimental physics, Vol.4, Part A, p.256 (1967).
2. M.A.D.Fluendy and K.P.Lawley, "Chemical Applications Of Molecular Beam Scattering" Chapman and Hall _London (1973).
3. J.B.Hasted, Proc. Roy. Soc. (London), A, **212**, 235 (1952).
4. J.Strong, H.V.Neher, C.H.Cartwright, A.E.Whitford and R.Hayward, "Modern Physical Laboratory Practice" Blackie & son limited (London) 1944, p116 .
5. J.B.Hasted, "Physics of atomic collisions" London_Butterworths (1964), p.87
6. M.Menzinger and R.Wolfgang, J. Amer. Chem. Soc., **89**, 5992 (1967).
7. C.A.McDowell, "Mass Spectrometry" McGraw_Hill book Co., NewYork (1963).
8. C.J.Davisson and C.J.Calbick, Phys. Rev., **38**, 585 (1931).
9. C.J.Davisson and C.J.Calbick, Phys. Rev., **42**, 580 (1932).
10. E.Harting and F.Read, "Electrostatic Lenses" Amsterdam (1976).
11. Weber,C. "Focusing of charged particles" NewYork_Academic press (1967), p.45_100.
12. Lanczos,C. "Applied analysis" London_Pitman (1957), p.15_38.
13. Paszkowski,B. "Electron Optics" Iliffe books (1968), p.25_53.
14. Weder,E. "Electromagnetic fields" NewYork_Wiley (1950), Vol.I.
15. Southwell,R.V. "Relaxation Methods In Theoretical physics" Oxford (1946).
16. Fox,L. Proc. Roy. Soc. A, **190**, 31 (1947).
17. Christopherson,D.G. and Southwell,R.V. Proc. Roy. Soc. A, **168**,

317 (1938).

18. Motz,H. and Klanfer,L. Proc. Phys. Soc., **58**, 30 (1946).
19. Rowland,Mrs.A.C. T.R.C. Program Specification MRS/RC.70/96, july 1969.
20. G.J.Schulz, Phys. Rev. Letters, **10**, 104 (1963).
21. C.E.Kuyatt, J.A.Simpson and S.R.Mielczarek, Phys. Rev. A, **138**, 385 (1965).
22. C.E.Kuyatt, J.A.Simpson and S.R.Mielczarek, J. Chem. Phys., **44**, 437 (1966).
23. G.J.Schulz and J.W.Philbrick, Phys. Rev. Letters, **13**, 477 (1964).
24. G.E.Chamberlain, Phys. Rev. Letters, **14**, 581 (1965).
25. G.E.Chamberlain and H.G.M.Heideman, Phys. Rev. Letters, **15**, 337 (1965).
26. J.A.Simpson, G.E.Chamberlain and S.R.Mielczarek, Phys. Rev. A, **139**, 1039 (1965).
27. E.M.Purcell, Phys. Rev., **54**, 818 (1938).
28. F.T.Rogers, Rev. Sci. Instr., **22**, 723 (1951).
29. R.H.Ritchie, J.S.Cheka and R.D.Birkhoff, Nucl. Inst. Methods, **6**, 157 (1960).
30. R.D.Birkhoff, J.M.Kohn, H.B.Eldridge and R.H.Ritchie, Nucl. Instr. Methods, **8**, 313 (1960).
31. H.H.Hubbell, W.J.McConnel and R.D.Birkhoff, Nucl. Instr. Methods, **31**, 18 (1964).
32. C.P.Brown, D.S.Craig and R.M.Willamson, Rev. Sci. Instr., **22**, 952 (1951).
33. George,N and Matthews,J.W, Appl. phys. Lett., **9**, 212 (1966).
34. Rigler,A.K and Vogl,T.P, Appl. Opt., **5**, 1086 (1966).
35. Rosen,L. Rev. Sci. Instr., **38**, 438 (1967).

36. Labeyrie,A. Proc. Conf. On Optics, (1967), Marseille, Centre National d'Etudes Spatiales, No.00015/PR/ED.
37. J.B.Anderson, R.R.Andres and J.B.Fenn, Advan. Chem. Phys., **3**, 275 (1966).
38. K.Bier and O.Hagena, "Rare field gas dynamics" Vol.2, Academic Press, NewYork 1966, p.260
39. Daley,N.R, Rev. Sci. Instr., **31**, 264 (1960).
40. Peirce,J.R, J. Appl. Phys., **11**, 548 (1940).
41. Curran,S.C., "Luminescence and the Scintillation Counts" Butterworths, London (1953).
42. Amdur,I. and Pearlman,H., J. Chem. Phys. **9**, 503 (1941).
43. Amdur,I. J. Chem. Phys. **28**, 987 (1958).
44. Simons,J.H. and Fryburg,G.C. J. Chem. Phys. **13**, 216 (1945).
45. Simons,J.H. and McAllister, J. Chem. Phys. **20**, 1431 (1952).
46. R.B.Bernstein and J.T.Muckermann, Advan. Chem. Phys. **12**, 389 (1967).
47. H.Pauly and L.P.Toennies, Advan. At. Mol. Phys. **1**, 195 (1965).
48. H.Pauly, "Physical Chemistry, an advanced treaties" Academic press, NewYork, (1974), chap.8, p.553.
49. Firsov,O.B., J. Exp. Theor. Phys. **24**, 279 (1953).
50. M.Rosen and D.R.Yennie, J. Math. Phys. **5**, 1505 (1964).
51. K.W.Ford and J.A.Wheeler, Ann. Phys. (N.Y.), **7**, 259 (1959).
52. P.E.Siska, J.M.Parson, T.P.Schafer and Y.T.Lee, J. Chem. Phys. **55**, 5762 (1971).
53. R.Gegenbach and Ch. Hahn, Chem. Phys. Lett. **15**, 604 (1972).
54. Felix T.Smith, R.P.Marchi and Kent G.Dedrick, Phys. Rev. **150**, 79 (1966).
55. G.H.Lane and E.Everhart, Phys. Rev. **120**, 2064 (1960).

56. F.T.Smith, R.P.Marchi, W.Aberth and D.C.Lorents, Phys. rev. **161**, 31 (1967).
57. C.Lehmann and G.Leibfried, Z. Physik **172**, 465 (1962).
58. G.Leibfried and T.Plesser, Z. Physik, **187**, 411 (1965).
59. B.Bederson and W.Fite, "Methods of experimental physics", (Academic press), Vol.7, part A, (1976) p.308
60. F.A.Morse and R.B.Bernstein, J. Chem. Phys. **37**, 2019 (1962).
61. G.W.Black, "Vibronic excitation in atom_molecule collisions", Ph.D thesis_ University of Edinburgh (1981).
62. J.Baudon, M.Barat and M.Abignoli, J. Phys. B, **3**, 207 (1970).
63. V.V.Afrosimov, Y.S.Gordeev, M.N.Panov and N.V.Fedorenko, Soviet Phys. Tech. Phys. **9**, 1248 (1965).
64. V.V.Afrosimov, Y.S.Gordeev, M.N.Panov and N.V.Fedorenko, Soviet Phys. Tech. Phys. **11**, 89 (1966).
65. E.Everhart and Q.C.Kessel, Phys. Rev. Letter **14**, 247 (1965).
66. Q.C.Kessel and E.Everhart, Phys. Rev. **146**, 16 (1966).
67. Q.C.Kessel, M.P.McCaughey and E.Everhart, Phys. Rev. Letter **16**, 1189 (1966).
68. Q.C.Kessel, M.P.McCaughey and E.Everhart, Phys. Rev. **153**, 57 (1967).
69. M.P.McCaughey, E.Knystants and E.Everhart, Phys. Rev. **175**, 14 (1968).
70. V.V.Afrosimov, Yu.S.Gordeev, A.M.Polyanskii and A.P.Shergin, J. Expt. Theot. Phys. (JETP), **30**, 441 (1970).
71. V.V.Afrosimov, Yu.S.Gordeev, A.M.Polyanskii and A.P.Shergin, Sovit Phys. Tech. Phys. **17**, 96 (1972).
72. D.Dowek, D.Dhuicq, J.Pommier, Vu Ngoc Tuan, V.Sidis and M.Barat, Phys. Rev. A, **24**, 2445 (1981).

73. R.G.Cooks, "Collision spectroscopy", Plenum Press (1978), p.203

74. Moiseiwitsch,B.L and Smith,S.J Rev. Mod. Phys., **40**, 238 (1968).

75. Sutcliff,V.C, Haddad,G.N, Steph,N.C, and Golden,D.E, Phys. Rev. A, **17**, 100 (1978).

76. John H.Birley, Phys. Rev. A, **10**, 550 (1974).

ACKNOWLEDGEMENTS

I wish to express my sincere thanks to my research supervisors Dr.M.A.D.Fluendy and Dr.A.G.A.Rae for their help, constant guidance and patience during the research,which make it possible for me to complete this work.

I would also like to thank the other members of the group who have helped me in many ways, and in particular Dr.George Keenan. I am greatly indebted to our technician Mr.Jimmy McKemmie for his technical assistance. I also wish to thank the electronics workshop of the Chemistry Department for construction the detector interface and other electronics work involved in this research. My thanks also to the University of Edinburgh for the provision of laboratory, library and computing facilities.

I am very greatful to my parents for their constant support and encouragement. Finally I am very thankful to the Government of Iraq to provide me the oppertunity in the form of scholarship to complete this work.

APPENDIX _I_

```
**EMAS EMAS-A EMAS** EDCD03 I. Abbas                    COWAN-JCMB
**EMAS EMAS-A EMAS** EDCD03 I. Abbas                    COWAN-JCMB
**EMAS EMAS-A EMAS** EDCD03 I. Abbas                    COWAN-JCMB
**EMAS EMAS-A EMAS** EDCD03 I. Abbas                    COWAN-JCMB
**EMAS EMAS-A EMAS** EDCD03 I. Abbas                    COWAN-JCMB
**EMAS EMAS-A EMAS** EDCD03 I. Abbas                    COWAN-JCMB
**EMAS EMAS-A EMAS** EDCD03 I. Abbas                    COWAN-JCMB
**EMAS EMAS-A EMAS** EDCD03 I. Abbas                    COWAN-JCMB
```

```
      PROGRAM TO FIT REDUCE cross SECTION DATA
      double precision rhot,fvecc(270),y(270),fsumsq,w(9950),x(15)
      common k,rhot(3,4000,10)
      do 50,k=1,9
      call input
      print*,'input complete'
50    continue
      call fit
      print*,'fitting complete'
      stop
      end


      subroutine input
      double precision rhot,fvecc(270),y(270),fsumsq,w(9950),x(15)
      common k,rhot(3,4000,10)
      goto(1,2,3,4,5,6,7,8,9),k
1     open(unit=201,file='rw100')
      goto 20
2     open(unit=202,file='rw200')
      goto 20
3     open(unit=203,file='rw300')
      goto 20
4     open(unit=204,file='rw400')
      goto 20
5     open(unit=205,file='rw500')
      goto 20
6     open(unit=206,file='rw600')
      goto 20
7     open(unit=207,file='rw700')
      goto 20
8     open(unit=208,file='rw800')
      goto 20
9     open(unit=209,file='rw900')
20    do 10,j=1,30
      read(k+200,*) rhot(1,j,k),rhot(2,j,k),rhot(3,j,k)
10    continue
      close(unit=k+200)
      return
      end


      subroutine fit
      double precision rhot,fvecc(270),y(270),fsumsq,w(9950),x(15)
      common k,rhot(3,4000,10)
      integer ifail,j,liw,lw,m,n
      integer iw(1)
      k=k-1
      n=4+k
      m=270
      liw=1
```

```
      lw=9950
      ifail=1
      print*,'values for A0 is taken arbitarily as 1'
      print*,'value for A1'
      read*,x(1)
      print*,'values for A2'
      read*,x(2)
      print*,'correction factor B'
      read*,x(3)
      print*,'value for N'
      read*,x(4)
      do 50,kt=1,k
      print*,'sensitivity factors,C,for each energy scan'
      read*, x(3+kt)
   50 continue
      call E04FDF(m,n,x,fsumsq,iw,liw,w,lw,ifail)
      print*,'fitted values for x(1),x(2),x(3),x(4),x(5)'
      print*,x(1)
      print*,x(2)
      print*,x(3)
      print*,x(4)
      DO 45 kt=1,9
      print*, x(3+kt)
 45   CONTINUE
      PRINT*,IFAIL
      print*,fsumsq
      open(unit=70,file='calibration')
      do 10,kt=1,k
      do 20,j=1,30
      rhot(2,j,kt)=rhot(2,j,kt)*10.**(((x(3)*rhot(3,j,kt))/rhot(1,
     #)))*(1/10.**(x(3+kt)))
      write(70,*)rhot(1,j,kt),rhot(2,j,kt)
   20 continue
   10 continue
      close(unit=70)
      end
        subroutine LSFUN1(m,n,xc,fvecc)
      double precision rhot,fvecc(270),y(270),fsumsq,w(9950),x(14)
       double precision xc(n)
      common k,rhot(3,4000,10)
      jt=0
      do 10,kt=1,k
      do 20,j=1,30
      JT=JT+1
      IF(RHOT(2,J,Kt).LT.0.0001) THEN
      FVECC(JT)= 0.0
      GO TO 20
      ENDIF
      IF(RHOT(1,J,Kt) .GT. 1500) THEN
      FVECC(JT)=0.0
      GO TO 20
      ENDIF
      Q=1.0+(xc(1)*rhot(1,j,kt))+(xc(2)*rhot(1,j,kt)**2)
      Z=10**((xc(3)*rhot(3,j,kt))/rhot(1,j,kt))
      fx=Q-Z-(xc(4)-rhot(2,j,kt))+10.**(xc(3+kt))
      fvecc(jt)=fx**2
   20 continue
   10 continue
      return
      end
```

200310 APPENDIX1 3K LISTED T15 LP15

EMAS EMAS-A EMAS EDCD03 I. Abbas COWAN-JCMB

```
**EMAS EMAS-A EMAS** EDCD03 I. Abbas                                    COWAN-JCMB
**EMAS EMAS-A EMAS** EDCD03 I. Abbas                                    COWAN-JCMB
**EMAS EMAS-A EMAS** EDCD03 I. Abbas                                    COWAN-JCMB
**EMAS EMAS-A EMAS** EDCD03 I. Abbas                                    COWAN-JCMB
**EMAS EMAS-A EMAS** EDCD03 I. Abbas                                    COWAN-JCMB
**EMAS EMAS-A EMAS** EDCD03 I. Abbas                                    COWAN-JCMB
**EMAS EMAS-A EMAS** EDCD03 I. Abbas                                    COWAN-JCMB
**EMAS EMAS-A EMAS** EDCD03 I. Abbas                                    COWAN-JCMB
```

```
      PROGRAM TO CORRECT SCATTERING ANGLE
      double precision sig,corr(1,4000)
      COMMON E,EHT,LCZ,DGS,SW,SIG(3,4000,10),A(4000,10),rhot(3,400(
      do 10,k=1,9
      CALL INPUT
      PRINT*,'INPUT COMPLETE'
      CALL SCANGLE
      PRINT*,'CORRECTED FOR TRUE SCATTERING ANGLE COMPLETE'
      CALL SOLIDANG
      PRINT*,'CORRECTED FOR SOLID ANGLE COMPLETE'
      CALL CORN
      PRINT*,'CORRECTION COMPLETE'
      call Labreduc
      print*,'Labreduc complete'
10    continue
      STOP
      END


      SUBROUTINE INPUT
      DOUBLE PRECISION SIG,corr(1,4000)
      common k,eht,lcz,dgs,sw,sig(3,4000,10),a(4000,10)
      common rhot(3,4000,10)
      goto(1,2,3,4,5,6,7,8,9),k
 1    open(unit=21,file='e100')
      goto 20
 2    open(unit=22,file='e200')
      goto 20
 3    open(unit=23,file='e300')
      goto 20
 4    open(unit=24,file='e400')
      goto 20
 5    open(unit=25,file='e500')
      goto 20
 6    open(unit=26,file='e600')
      goto 20
 7    open(unit=27,file='e700')
      goto 20
 8    open(unit=28,file='e800')
      goto 20
 9    open(unit=29,file='e900')
 20   do 10,j=1,30
      read(k+20,*) sig(1,j,k),sig(2,j,k),sig(3,j,k)
 10   continue
      close(unit=k+20)
      return
      end
      SUBROUTINE SCANGLE
      DOUBLE PRECISION SIG,corr(1,4000)
      COMMON E,EHT,LCZ,DGS,SW,SIG(3,4000,10),A(4000,10)
      common rhot(3,4000,10)
```

```
      REAL E,EHT
      EHT=25000
       Pi=3.1415
      LCZ=130
      DGS=20
      sw=0.2
      DO 10,i=1,35
      X=14.0-(i*0.4)
      L=LCZ+DGS*(SQRT(sig(3,i,k)/(sig(3,i,k)+EHT)))
      A(i,k)=(X/L)
      B=atan((x-sw)/L)-atan(A(i,k))
 10   CONTINUE
      RETURN
      END


      SUBROUTINE SOLIDANG
      DOUBLE PRECISION SIG,corr(1,4000)
      COMMON E,EHT,LCZ,DGS,SW,SIG(3,4000,10),A(4000,10)
      common rhot(3,4000,10),x(35)
      SW=0.2
      Pi=3.1415
      DO 10,i=1,30
      T=COS(A(i,k))/Lcz
      FACT=(T*B)
      sig(2,i,k)=sig(2,i,k)/fact
      SIG(1,i,k)=atan(A(i,k))
 10   CONTINUE
      RETURN
      END


     SUBROUTINE CORN
     DOUBLE PRECISION SIG,CORR(1,4000)
      common k,eht,lcz,dgs,sw,sig(3,4000,10),a(4000,10)
      common rhot(3,4000,10)
     OPEN(UNIT=12,FILE='RESULT')
     OPEN(UNIT=15,FILE='NORMALZ')
     DO 10,i=1,30
     READ(15,*)CORR(1,i)
     SIG(2,i,k)=SIG(2,i,k)*CORR(1,i)
     WRITE(12,*)SIG(1,i,k),SIG(2,i,k)
10   CONTINUE
     RETURN
     END
      subroutine Labreduc
      double precision sig,corr(1,4000)
      common e,eht,lcz,dgs,sw,sig(3,4000,10),a(4000,10)
      common rhot(3,4000,10)
      goto(1,2,3,4,5,6,7,8,9),k
 1    open(unit=101,file='newrw100')
      goto 20
 2    open(unit=102,file='newrw200')
      goto 20
 3    open(unit=103,file='newrw300')
      goto 20
 4    open(unit=104,file='newrw400')
      goto 20
 5    open(unit=105,file='newrw500')
      goto 20
 6    open(unit=106,file='newrw600')
      goto 20
 7    open(unit=107,file='newrw700')
      goto 20
 8    open(unit=108,file='newrw800')
      goto 20
```

```
 9    open(unit=109,file='newrw300')
 20   do 10,j=1,30
      rhot(1,j,k)=sig(3,j,k)*sig(1,j,k)
      rhot(2,j,k)=sig(1,j,k)*sin(sig(1,j,k))*sig(2,j,k)
      write(k+100,*) rhot(1,j,k),rhot(2,j,k),sig(3,j,k)
 10   continue
      close(unit=k+100)
      return
      end

)0311 APPENDIX2 4K LISTED T15 LP15

(EMAS EMAS-A EMAS** EDCD03 I. Abbas                    COWAN-JCMB
(EMAS EMAS-A EMAS** EDCD03 I. Abbas                    COWAN-JCMB
(EMAS EMAS-A EMAS** EDCD03 I. Abbas                    COWAN-JCMB
(EMAS EMAS-A EMAS** EDCD03 I. Abbas                    COWAN-JCMB
(EMAS EMAS-A EMAS** EDCD03 I. Abbas                    COWAN-JCMB
(EMAS EMAS-A EMAS** EDCD03 I. Abbas                    COWAN-JCMB
(EMAS EMAS-A EMAS** EDCD03 I. Abbas                    COWAN-JCMB
(EMAS EMAS-A EMAS** EDCD03 I. Abbas                    COWAN-JCMB
```

```
**EMAS EMAS-A EMAS** EDCD03 I. Abbas                                    COWAN-JCMB
**EMAS EMAS-A EMAS** EDCD03 I. Abbas                                    COWAN-JCMB
**EMAS EMAS-A EMAS** EDCD03 I. Abbas                                    COWAN-JCMB
**EMAS EMAS-A EMAS** EDCD03 I. Abbas                                    COWAN-JCMB
**EMAS EMAS-A EMAS** EDCD03 I. Abbas                                    COWAN-JCMB
**EMAS EMAS-A EMAS** EDCD03 I. Abbas                                    COWAN-JCMB
**EMAS EMAS-A EMAS** EDCD03 I. Abbas                                    COWAN-JCMB
**EMAS EMAS-A EMAS** EDCD03 I. Abbas                                    COWAN-JCMB
```

```
      Program FIRSOV
      Implicit double precision(a-h,o-z)
      Double precision x(31),y(31),w(31),work1(3,31),work2(2,11)
     #,ak(11)
      Double precision a(11,11),s(11),rhot(2,31),
     #taurh(2,59),defln(2,31),pot1(2,44)
      Common delta
      data w/31*1/
      Call intrp(taurh,w)
      print*,'Interpolation complete'
      Call fstint(taurh,defln)
      print*,'Deflection function calculated'
      Stop
      End

      Subroutine intrp(taurh,w)
      Implicit double precision(a-h,o-z)
      Double precision x(30),y(30),w(30),work1(3,30),work2(2,11)
     #,ak(11)
      Double precision a(11,11),s(11),rhot(2,30),
     #taurh(2,59)
      Common delta
      open(unit=3,file='cofm')
      read(3,*)((rhot(1,j),rhot(2,j)),j=1,30)
      do 1,j=1,30
      x(j)=log(rhot(1,j))
1     y(j)=rhot(2,j)
      Call E02ADF(30,11,11,x,y,w,work1,work2,
     #a,s,ifail)
      print*,'Polynomial computed'
      do 2,i=1,11
2     ak(i)=a(11,i)
      X1=X(1)
      XM=X(30)
      d=xm-x1
      dx=d/59.
      do 3,i=1,59
      xv=i*dx+x1
      xbar=((xv-x1)-(xm-xv))/d
      Call E02AEF(11,ak,xbar,val,ifail)
      taurh(1,i)=xv
3     taurh(2,i)=val
       delta=taurh(2,59)*((taurh(2,59)-taurh(2,58))/
     # (taurh(1,59)-taurh(1,58)))
      return
      end
      Subroutine Fstint(taurh,defln)
      Implicit Double precision(a-h,o-z)
      Double precision taurh(2,59),defln(2,32),ab(59),dep(59)
      Common delta
```

```
      do 2,j=1,32
      i=0
      do 1,k=j,59
      i=i+1
      ab(i)=taurh(1,k)
 1    dep(i)=taurh(2,k)
      n=60-j
      Call D01GAF(ab,dep,n,ans,er,ifail)
      defln(1,j)=exp(ab(1))
      ans=abs(ans)+delta
      ans=dsqrt(2*ans)
      defln(2,j)=ans
 2    write(4,*)ans,defln(1,j)
      return
      end
```

```
200315 FIRSOV2 2K LISTED T15 LP15

**EMAS EMAS-A EMAS** EDCD03 I. Abbas                    COWAN-JCMB
**EMAS EMAS-A EMAS** EDCD03 I. Abbas                    COWAN-JCMB
**EMAS EMAS-A EMAS** EDCD03 I. Abbas                    COWAN-JCMB
**EMAS EMAS-A EMAS** EDCD03 I. Abbas                    COWAN-JCMB
**EMAS EMAS-A EMAS** EDCD03 I. Abbas                    COWAN-JCMB
**EMAS EMAS-A EMAS** EDCD03 I. Abbas                    COWAN-JCMB
**EMAS EMAS-A EMAS** EDCD03 I. Abbas                    COWAN-JCMB
**EMAS EMAS-A EMAS** EDCD03 I. Abbas                    COWAN-JCMB

P
```

```
**EMAS EMAS-A EMAS** EDCD03 I. Abbas                                    COWAN-JCME
**EMAS EMAS-A EMAS** EDCD03 I. Abbas                                    COWAN-JCME
**EMAS EMAS-A EMAS** EDCD03 I. Abbas                                    COWAN-JCME
**EMAS EMAS-A EMAS** EDCD03 I. Abbas                                    COWAN-JCME
**EMAS EMAS-A EMAS** EDCD03 I. Abbas                                    COWAN-JCME
**EMAS EMAS-A EMAS** EDCD03 I. Abbas                                    COWAN-JCME
**EMAS EMAS-A EMAS** EDCD03 I. Abbas                                    COWAN-JCME
**EMAS EMAS-A EMAS** EDCD03 I. Abbas                                    COWAN-JCME
```

```
      Implicit Double precision(a-h,o-z)
      Double precision taub(2,30),taus(2,30),ak(11),w(30)
     #,vr(2,50)
      Common taul,sm,sl,ak
      Data w/30*1./
      pi=3.1415
      Call nput(taub)
      Call ntrp(w,taub,taus,ak)
          step=(taus(1,30)-taus(1,1))/50
          j=50
          do 1,s=taus(1,1),taus(1,30),step
      if(j.eq.0) go to 1
             Call igrate(s,res)
             potl=tau(s)-2/pi*res
             vr(1,j)=1./s
             vr(2,j)=potl
1         j=j-1
      Call output(vr)
      stop
      end
      Subroutine nput(taub)
      Implicit Double precision(a-h,o-z)
      Common taul,sm,sl
      Double precision taub(2,30)
      open(unit=3,file='defin')
      do 1,j=1,30
1     read(3,*)taub(1,j),taub(2,j)
      return
      end
      Subroutine ntrp(w,taub,taus,ak)
      Implicit double precision(a-h,o-z)
      Double precision x(30),y(30),w(30),work1(3,30),work2(2,11)
     #,ak(11)
      Double precision a(11,11),s(11),taub(2,30),
     #taus(2,30)
      Common taul,sm,sl
      do 1,j=1,30
        taus(1,j)=1./taub(1,j)
        taus(2,j)=taub(2,j)
        x(j)=taus(1,j)
1     y(j)=taus(2,j)
      sm=taus(1,30)
      sl=taus(1,1)
      taul=taus(2,1)
      Call E02ADF(30,11,11,x,y,w,work1,work2,
     #a,s,ifail)
      do 2,i=1,11
2     ak(i)=a(11,i)
      return
      end
```

```
      Implicit Double precision(a-h,o-z)
      Double precision uintg(100),du(100)
      Real h
      ifail=0
      h=s/99.
      do 2,i=2,99
      u=(i-1)*h
      a=tau(s)*u/s-tau(u)
      b=u*dsqrt(1-(u**2)/(s**2))
      du(i)=u
      uintg(i)=a/b
      du(1)=0.0
      du(100)=s
      uintg(1)=tau(s)/s
      uintg(100)=0.0D+00
      Call D01GAF(du,uintg,100,res,er,ifail)
      return
      end
      Subroutine output(vr)
      Implicit Double precision(a-h,o-z)
      Double precision vr(2,50)
      Open(unit=4,file='Vofr')
      do 1,j=1,50
      write(4,*)vr(1,j),vr(2,j)
      return
      end
      Function tau(s)
      Implicit Double precision(a-h,o-z)
      Common taul,sm,sl,ak
      Double precision ak(11)
      if(s.le.sl) then
      tau=s*taul/sl
      else
      xbar=((s-sl)-(sm-s))/(sm-sl)
      Call E02AEF(11,ak,xbar,val,ifail)
      tau=val
      endif
      return
      end
```

```
0312 POTL 3K LISTED T15 LP15

EMAS EMAS-A EMAS** EDCD03 I. Abbas                    COWAN-JCME
EMAS EMAS-A EMAS** EDCD03 I. Abbas                    COWAN-JCME
EMAS EMAS-A EMAS** EDCD03 I. Abbas                    COWAN-JCME
EMAS EMAS-A EMAS** EDCD03 I. Abbas                    COWAN-JCME
EMAS EMAS-A EMAS** EDCD03 I. Abbas                    COWAN-JCME
EMAS EMAS-A EMAS** EDCD03 I. Abbas                    COWAN-JCME
EMAS EMAS-A EMAS** EDCD03 I. Abbas                    COWAN-JCME
EMAS EMAS-A EMAS** EDCD03 I. Abbas                    COWAN-JCME
```

```
**EMAS EMAS-A EMAS** EDCD03 I. Abbas                                    COWAN-JCM
**EMAS EMAS-A EMAS** EDCD03 I. Abbas                                    COWAN-JCM
**EMAS EMAS-A EMAS** EDCD03 I. Abbas                                    COWAN-JCM
**EMAS EMAS-A EMAS** EDCD03 I. Abbas                                    COWAN-JCM
**EMAS EMAS-A EMAS** EDCD03 I. Abbas                                    COWAN-JCM
**EMAS EMAS-A EMAS** EDCD03 I. Abbas                                    COWAN-JCM
**EMAS EMAS-A EMAS** EDCD03 I. Abbas                                    COWAN-JCM
**EMAS EMAS-A EMAS** EDCD03 I. Abbas                                    COWAN-JCM
```

```
      Program Potnl
      Implicit Double precision(a-h,o-z)
      Double precision taub(2,30),taus(2,30),ak(11),w(30)
     #,vr(2,50)
      Common taul,sm,sl,ak
      Data w/30*1./
      pi=3.1415
      Call nput(taub)
      Call ntrp(w,taub,taus,ak)
      Call igrate(s,res)
      potl=tau(s)-2/pi*res
      vr(1,j)=1./s
      vr(2,j)=potl
      Call output(vr)
      stop
      end
      Subroutine nput(taub)
      Implicit Double precision(a-h,o-z)
      Common taul,sm,sl
      Double precision taub(2,30)
      Open(unit=3,file='defln')
      do 1,j=1,30
1     read(3,*)taub(1,j),taub(2,j)
      return
      end
      Subroutine ntrp(w,taub,taus,ak)
      Implicit double precision(a-h,o-z)
      Double precision x(30),y(30),w(30),work1(3,30),work2(2,11
     #,ak(11)
      Double precision a(11,11),s(11),taub(2,30),
     #taus(2,47)
      Common taul,sm,sl
      do 1,j=1,30
      taus(1,j)=1./taub(1,j)
      taus(2,j)=taub(2,j)
      x(j)=taus(1,j)
1     y(j)=taus(2,j)
      sm=taus(1,30)
      sl=taus(1,1)
      taul=taus(2,1)
      Call E02ADF(30,11,11,x,y,w,work1,work2,
     #a,s,ifail)
      do 2,i=1,11
2     ak(i)=a(11,i)
      return
      end
      Subroutine igrate(s,res)
      Implicit Double precision(a-h,o-z)
      Double precision uintg(100),du(100)
      Real h
```

```
      do 2,i=1,100
      u=(i-1)*h
      a=tau(s)*u/s-tau(u)
      b=u*dsqrt(1-(u**2)/(s**2))
      du(1)=u
2     uintg(i)=a/b
      du(1)=0.0
      du(100)=s
      Call D01GAF(du,uintg,100,res,er,ifail)
      return
      end
      Subroutine output(vr)
      Implicit Double precision(a-h,o-z)
      Double precision vr(2,50)
      Open(unit=4,file='Vofr')
      do 1,j=1,30
1     write(4,*)vr(1,j),vr(2,j)
      return
      end
```

200314 FUNCTION 2K LISTED T15 LP15

```
**EMAS EMAS-A EMAS** EDCD03 I. Abbas                    COWAN-JCM
**EMAS EMAS-A EMAS** EDCD03 I. Abbas                    COWAN-JCM
**EMAS EMAS-A EMAS** EDCD03 I. Abbas                    COWAN-JCM
**EMAS EMAS-A EMAS** EDCD03 I. Abbas                    COWAN-JCM
**EMAS EMAS-A EMAS** EDCD03 I. Abbas                    COWAN-JCM
**EMAS EMAS-A EMAS** EDCD03 I. Abbas                    COWAN-JCM
**EMAS EMAS-A EMAS** EDCD03 I. Abbas                    COWAN-JCM
**EMAS EMAS-A EMAS** EDCD03 I. Abbas                    COWAN-JCM
```

APPENDIX _II_

ION_PHOTON CORRELATION DATA
OF He^+/N_2 SYSTEM.

Ch.no., Ints.	Ch.no., Ints.
24,4070	75,4061
25,4052	76,4053
26,4059	77,4039
27,4091	78,4029
28,4053	79,4056
29,4030	80,4042
30,4052	81,4045
31,5002	82,4015
32,4059	83,4056
33,4075	84,4042
34,4054	85,4048
35,4078	86,4043
36,4058	87,4038
37,4085	88,4078
38,4048	89,4050
39,4084	90,4047
40,4059	91,4045
41,4085	92,4056
42,4090	93,4047
43,5009	94,4045
44,4031	95,4070
45,4059	96,4054
46,4036	97,4037
47,4061	98,4011
48,4059	99,4028
49,4073	100,4026
50,4016	101,4022
51,4059	102,4020
52,4054	103,4018
53,4053	104,4035
54,4069	105,4027
55,4031	106,4020
56,4044	107,4035
57,4035	108,4021
58,4058	109,4018
59,4005	110,4022
60,4018	111,4027
61,4058	112,4025
62,4044	113,4046
63,4067	114,4015
64,4027	115,4021
65,4044	116,4030
66,4017	117,4027
67,4039	118,4034
68,4058	119,4030
69,4032	120,4029
70,4056	121,4020
71,4052	122,4020
72,4061	123,4020
73,4029	124,4021
74,4044	125,4017

126,4017
127,4031
128,4020
129,4014
130,4017
131,4023
132,4025
133,3027
134,4020
135,4018
136,4030
137,4013
138,4018
139,4031
140,4010
141,4026
142,4022
143,4038
144,4023
145,4025
146,4035
147,4020
148,4022
149,4037
150,4023
151,4025
152,4013
153,4021
154,4014
155,4033
156,4023
157,4018
158,4018
159,4022
160,4026
161,4035
162,4023
163,4023
164,4016
165,4025
166,4031
167,4014
168,4021
169,4029
170,4032
171,4033
172,4029
173,4027
174,4016
175,4020
176,4021
177,4012
178,4022
179,4025
180,4037
181,4017
182,4019
183,4018
184,4026
185,4023
186,4010
187,4031
188,4018
189,4031
190,4019
191,4019
192,4031
193,4021
194,4025
195,4023
196,4025
197,4041
198,4057
199,4038
200,4027
201,4021
202,4023
203,4029
204,4020
205,4022
206,4023
207,4027
208,4030
209,4023
210,4023
211,4018
212,4021
213,4023
214,4034
215,4014
216,4026
217,4011
218,4041
219,4028
220,4031
221,4023
222,4018
223,4030
224,4025
225,4019
226,4034
227,4021
228,4022
229,4028
230,4016
231,4020
232,4028
233,4029
234,4015
235,4026

236,4030
237,4029
238,4021
239,4032
240,4011
241,4024
242,4028
243,4021
244,4023
245,4025
246,4010
247,4023
248,4027
249,4022
250,4026
251,4019
252,4031
253,4021
254,4021
255,4028
256,4035
257,4014
258,4017
259,4027
260,4030
261,4038
262,4014
263,4028
264,4039
265,4030
266,4038
267,4011
268,4039
269,4015
270,4010
271,4031
272,4031
273,4020
274,4030
275,4029
276,4033
277,4032
278,4025
279,4035
280,4021
281,4021
282,4018
283,4033
284,4019
285,4021
286,4031
287,4033
288,4026
289,4036
290,4032
291,4026
292,4020
293,4023
294,4027
295,4022
296,4031
297,4043
298,4017
299,4020
300,4018
301,4022

200318 CDINC 2K LISTED T15 LP15

EMAS EMAS-A EMAS EDCD03 I. Abbas
EMAS EMAS-A EMAS EDCD03 I. Abbas
EMAS EMAS-A EMAS EDCD03 I. Abbas
EMAS EMAS-A EMAS EDCD03 I. Abbas
EMAS EMAS-A EMAS EDCD03 I. Abbas
EMAS EMAS-A EMAS EDCD03 I. Abbas
EMAS EMAS-A EMAS EDCD03 I. Abbas
EMAS EMAS-A EMAS EDCD03 I. Abbas

```
      common it(1030),i(1030)
      double precision fvecc(1030),y(1030)
      double precision x(5)
      double precision fsumsq,w(15000)
      integer ifail,j,liw,lw,m,n
      integer iw(1)
      n=5
      m=202
      liw=1
      lw=15000
      ifail=1
      do 60 j=1,m
 60   read(1,100) it(j),i(j)
 100  format(2I6)
      print*,'start values for background'
      read*,x(1)
      read*,x(2)
      print*,'peak height='
      read*,x(3)
      print*,'peak locn. ='
      read*,x(4)
      print*,'peak width='
      read*,x(5)
      call E04fdf(m,n,x,fsumsq,iw,liw,w,lw,ifail)
      print*,'fitted values'
      print*,fsumsq
      print*,x(1)
      print*,x(2)
      print*,'peak height='
      print*,x(3)
      print*, 'peak location='
      print*,x(4)
      print*, 'peak width='
      print*,x(5)
      do 70 k=1,m
      call lsfun1(m,n,x,fvecc)
      y(k)=fvecc(k)+i(k)
 70   write(2,101) it(k),y(k)
 101  format(I6,3x,f8.3)
      end
      subroutine lsfun1(m,n,xc,fvecc)
      common it(1030),i(1030)
      double precision fvecc(m),xc(n),z,q
       do 80 k=1,m
      q=xc(2)*it(k)
      if(q.gt.50.) then
      q=50.
      end if
       fvecc(k)=xc(1)*exp(-q)
      z=0.5*((it(k)-xc(4))/xc(5))**2
      if (z.gt.50.) then
      z=50.
      end if
      fvecc(k)=fvecc(k)+xc(3)*exp(-z)
      fvecc(k)=fvecc(k)-i(k)
  80  continue
      return
      end
```

```
200316 SAM2 2K LISTED T15 LP15

**EMAS EMAS-A EMAS** EDCD03 I.Abbas                    COWAN-JCMB
**EMAS EMAS-A EMAS** EDCD03 I.Abbas                    COWAN-JCMB
**EMAS EMAS-A EMAS** EDCD03 I.Abbas                    COWAN-JCMB
```

PUBLICATION

J. Phys. E: Sci. Instrum. **21** (1988) 1044–1050. Printed in the UK

A position-sensitive particle detector

I Abbas†, E E B Campbell‡, M A D Fluendy†, A King† and C G McGill†
† Department of Chemistry, University of Edinburgh, West Mains Road, Edinburgh EH9 3JJ, UK
‡ Fakultat für Physik, Universität Freiburg, Herman-Herder Strasse 3, 7800 Freiburg, FRG

Received 19 February 1988, in final form 10 June 1988

Abstract. The design, construction and performance of a position-sensitive particle detection system for use in experiments involving the scattering or dispersion of atoms or ions is described. The device may have applications in atomic and molecular scattering, mass spectrometry and other similar fields where the arrival in position and time of particles must be monitored. In the present realisation (designed for use in atomic collision experiments) an angular resolution of 0.1°, a response time ~10 ns and a detection efficiency >90% have been achieved.

1. Introduction

Position-sensitive particle detectors offer several well known advantages, namely the data collection rate in any measurement can be greatly enhanced and noise effects associated with a long series of sequential measurements eliminated.

In the present application the device described is used in conjunction with a crossed molecular beam collision experiment involving the coincident detection of photons and scattered particles (ions or atoms) from molecular collisions. The experimental parameters to be recorded in this experiment are the scattering angle for the particle and the flight time. However, alternative applications to encode other parameters by the use of suitable dispersing elements for mass, spin, etc can be foreseen.

Other techniques have been used to realise position-sensitive particle detection. Some, such as the charge-coupled raster scan devices are too slow for the present application. Devices based upon channel plates are fast enough but as usually constructed depend upon a charge division technique to determine the position: a technique which limits the response time. In the present application, the required energy resolution necessitates flight paths of >1 m length so that to cover the angular range of interest very large channel plates would be needed. The fibre-optic technique to be described, in contrast, permits the geometry of the detector to be tailored specifically for the task and in the present device provides 45 separate angular channels for particle detection.

1.1. Specific performance requirements

The scientific objectives of the programme led to the following requirements in the particle detector.

(i) An angular range of approximately 0–10°.

(ii) An angular resolution of 0.1° (or ~ 2.5 mm at the expected scattering distance of 1.5 m).

(iii) The capability of detecting particles scattering with an energy in the range 10–1000 eV.

(iv) A time resolution adequate to resolve energy losses of 0.2 eV throughout the initial collision energy range and to

0022-3735/88/111044+07 $02.50

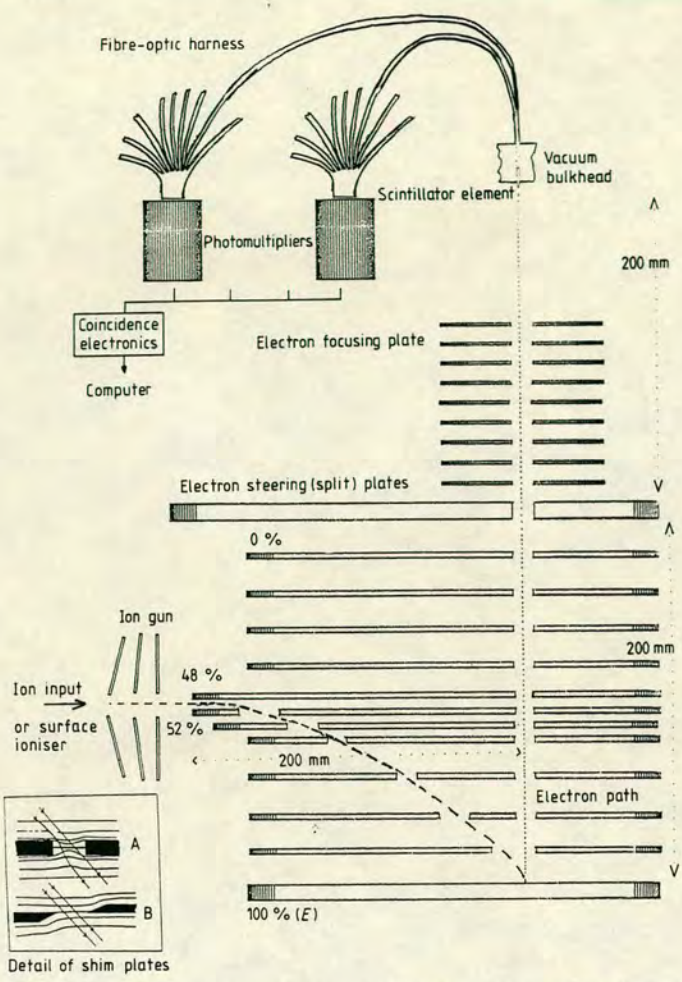

Figure 1. Outline design of the detector showing a vertical section along the direction of the input signal ions which enter from the left and are focused by the ion gun. Alternatively, neutral atoms may enter from the right (between the 48% and 52% plates) and can be ionised by a surface ioniser (not shown). The subsequent ion path is shown (– – –). Secondary electron ejection occurs when they strike the bottom (100%) plate and the resulting electron trajectory is shown (.....). The secondary electrons are accelerated to strike small scintillator elements which also serve as a vacuum barrier. The details of the field shimming plates are shown in the inset. The chamfered type (lowest) had a superior performance and was used throughout.

provide coincidence signals with a resolution of $\sim 5 \times 10^{-9}$ s.
(v) To handle a dynamic range between the smallest and widest angles of approximately 10^6 (or as large as possible).
(vi) The first experiments would involve either fast neutral alkali-metal atoms which can be very rapidly ionised on a warm tungsten ribbon or positive atomic ions which would need no initial ionisation.

2. Principles of operation

2.1. Outline

A vertical section through the detector is shown (somewhat schematically) in figure 1. A further vertical section perpendicular to that in figure 1 and also to the input plane for the signal particles is shown in figure 2. The basic detection technique, acceleration of an incident ion to produce secondary electrons from a surface followed by scintillation counting of the secondary electrons, is based upon a single-channel detector designed by Daley (1960). It can be used for either the detection of positive ions or the detection of energetic alkali atoms, the latter being detected as ions following their collision with a warm tungsten surface. (In principle, any other ionisation technique could be used at this point.) The ions enter a Pierce gun designed to produce a parallel sheet of ions. The entrance slit of this gun is arranged to encompass a wide range of scattering angles of ions/atoms coming from the collision region of a crossed-beam experiment. The scattered ions are injected into a region of strong uniform vertical electric field. This field is produced by applying a voltage, E, to the bottom (100% E) plate and appropriate percentages of E to the other shimming plates in the stack. In this field focused ions fall in a parabola, through appropriately positioned slits in the shimming electrodes, to strike the bottom plate which is coated with a thin Al_2O_3 film. Secondary electrons ejected from this region are accelerated upwards by the field through a further region where they may be steered or focused to form an image of the initial scattering pattern on an array of scintillators. The location of a scattering event in angle and time is then coded via a bank of photomultipliers multiplexed via optical glass fibres to individual elements in the scintillator array. If each scintillator element is connected to two photomultipliers an arrival event, signalled by an electron burst on a specific element, then produces simultaneous signals in both photomultipliers. If this coincidence is detected, the arrival time can be determined directly while the angular location of the event is coded by noting which

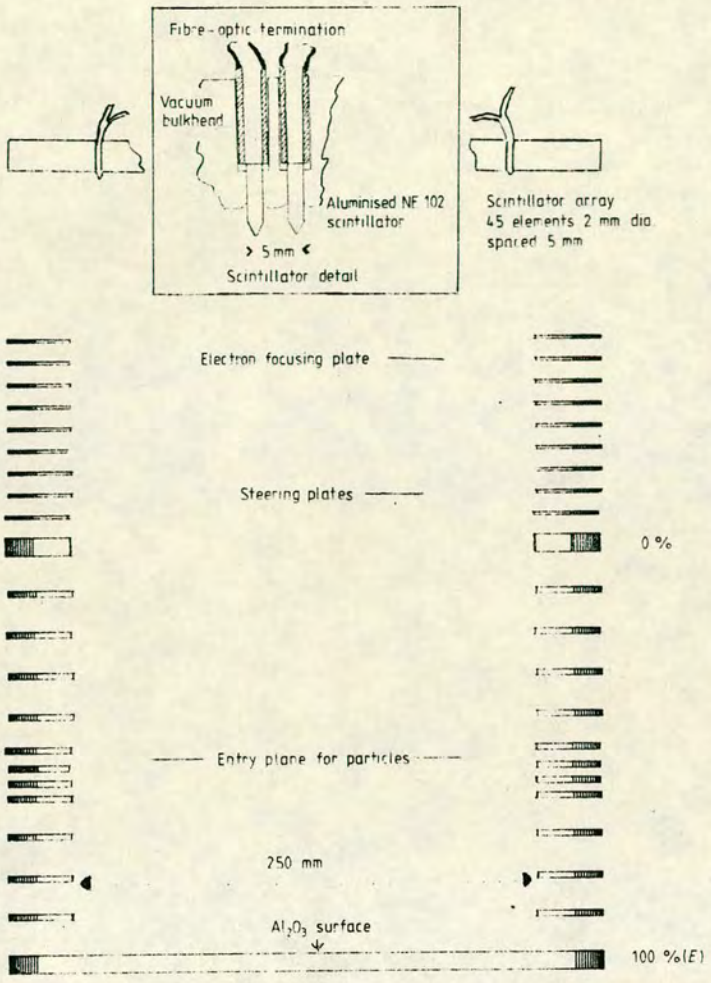

Figure 2. Vertical section through the detector perpendicular to the incoming ions (and the view in figure 1). The inset shows the detail of the conically ended scintillator elements and the fibre-optic terminations.

specific pair of photomultipliers are involved in the coincidence. Thus a bank of ten photomultipliers could encode by this binary coincidence method $^{10}C_2$, i.e. 45 individual angular elements.

The final section of the apparatus thus consists of a network of fibre-optic bundles which connect the individual scintillator elements to a bank of photomultipliers, each multiplier being connected to nine different scintillators. The signals from these multipliers are processed by a high-speed electronic interface (10 ns) which detects coincidences between the photomultiplier signals, determines the address of the scintillator element responsible and outputs both time and angular information to a microcomputer.

2.2. Predicted performance – detection sensitivity

The probability of recording an event signalled by a burst of a photons arriving at a photomultiplier tube is approximately:

$$\text{Probability} \simeq 1-(1-q)^a \tag{1}$$

where q is the counting efficiency of the tube.

For the coincident detection of events signalled by the arrival of a and b photons in two PM tubes the probability is now:

$$\text{Probability} = [1-(1-q)^a][1-(1-q)^b] \tag{2}$$

In the present device the distribution of the photons available from the scintillator is stochastically determined. The probability of detecting the event will then be

$$\text{Probability} = \sum \text{Probability of partitioning } [1-(1-q)^a][1-(1-q)^b] \tag{3}$$

where the sum extends over all possible partitionings of the photons, 2^N, with $N=a+b$ in this case. Thus:

$$\text{Probability} = \frac{1}{2^N}\sum_{a=0}^{a=N}\frac{N!}{(N-a)!a!}[1-(1-q)^a][1-(1-q)^{N-a}]. \tag{4}$$

At the desirable operating regime for the detector – near unit efficiency – N will be large†. The most probable partitioning with $a=N/2$ will then be dominant and it can be seen by differentiation of (4) that this is also the most sensitive arrangement. In the operational region the probability will

† Equation (4) can be evaluated exactly using the binomial theorem to obtain:

$$\text{Probability} = 1+(1-q)^N-\frac{1}{2^N}[2(2-q)^N].$$

then be approximately:

$$\text{Probability} \approx [1-(1-q)^{N/2}]^2 \qquad (5)$$

In the device as constructed the detailed parameters contributing to the sensitivity are: P_c, the probability of producing an ion from each neutral incident atom (~0.9 in the case of energetic alkali atoms); t, the transmission probability for the ion to the Al_2O_3 surface (~0.95 from trajectory calculations); l, the transmission probability for an electron from the Al_2O_3 surface to the scintillator (~0.9); P, the number of photons produced per electron in the type 102 A scintillator (manufacturer's data, Nuclear Enterprise Ltd and Curran (1953) suggest ~100 eV required per photon, i.e. ~3% efficiency; Hasted (1964) suggests 200–400 eV per photon); conservative estimate ~250 photons at 50 kV; j, the number of secondary electrons produced per ion (measured as 11 at 50 kV); r, the photomultiplier counting efficiency (0.2); d, the fibre transmission (0.5); and e, the collection efficiency from scintillator to fibre (0.02).

Thus equation (5) becomes:

$$\text{Probability} = P_c t[1-(1-rd)^{jlPe}]^2. \qquad (6)$$

Using these central estimates a detection probability (at an operating voltage of 50 kV) of 0.86 $P_c t$ can be calculated, the main uncertainties in this calculation being the optical collection efficiency, e, and the number of photons produced. The numbers of photons arriving at the scintillator is Pjl. Since both the number of secondary electrons and the number of photons produced are approximately linear functions of the collision energy, which is the operating voltage E in this case, we obtain:

$$\text{Number of photons} \approx (E/\text{kV})^2.$$

The expected performance, around the operational range, is shown in figure 3. It is obviously desirable to operate in the saturated region where the sensitivity of the device will be most stable.

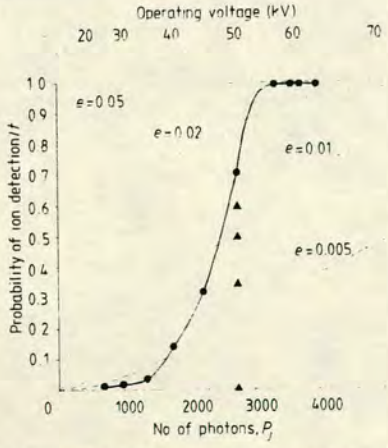

Figure 3. The estimated performance, the sensitivity against number of photons produced in the scintillator per incident atom or ion (approximately scaled to operating voltage of detector) is shown by the broken curves. The actual performance at a number of stages in the development of the instrument is also plotted (full triangles), together with the present performance (full curve)

2.2. Noise

The random noise due to dark-current fluctuations in the photomultipliers, B (~20 Hz), will produce a noise count of $B^2\tau$. The coincidence width, τ, will be ~10^{-8} s so that the dark-noise rate, even at the single-photon discriminator level will be ~4×10^{-6} Hz and quite negligible.

A more important noise source will arise from stray ions originating from thermal or photoionisation processes in the detector. Experience with the single channel detector has shown that this is a strong function of the background pressure and cleanliness of the system. It can also be minimised by using tight-focusing conditions to eliminate noise sources which are not very close to the designed ionising region. A total noise rate of less than 0.01 Hz can be expected.

2.3. Angular and time resolution

The angular resolution is determined by the uniformity of the fields achieved in the detector and is a matter of detailed design. The response time of the device will depend upon the scintillator and discriminator performance: with NE102A plastic scintillator no difficulties should arise in achieving the design target of ~10 ns.

3. Detailed design

3.1. Electrostatic ion and electron optics

The electrostatic design can be seen in figure 1. The ion injection gun which focuses the newly formed ions onto the Al_2O_3 plate is based upon the Pierce geometry (Pierce 1940). The geometry was optimised by numerically calculating ion and electron trajectories through the field as digitised from an analogue field plotter. It was found that the focusing could be significantly improved by tapering and offsetting the field shim plates as shown in the inset to figure 1.

The whole lens system has to be wide enough to ensure, there are no end effects and mechanical tolerances in the plates (±0.1 mm) are such that field inhomogeneities cannot lead to a reduction in performance. It has been estimated that the earth's magnetic field in the worst case will cause a deviation of 2 mm eastward (i.e. along the scintillator axis) at 50 kV accelerating voltage. This can be compensated for by fitting Helmholtz coils or by taking the effect into account when assigning angles of deflection to the different scintillator elements since all the electrons will be affected equally.

At a nominal operating voltage (E) of 50 kV it was found that the optimum design could focus the detector 'object' to a line with a standard deviation = 0.5 mm, i.e. 95% of ion trajectories were found to strike in a 2 mm wide strip on the Al_2O_3 film. The dispersion in flight time then had a standard deviation of 1 ns.

The electron optics were designed to produce a real diminished image ($M=0.4$) of this illuminated strip on the scintillator elements. The design tables of Harting and Read (1976) were used for this purpose. The 95% electron image was predicted to be ~1 mm wide (after considering aberration effects).

Various steering and auxiliary focusing plates were incorporated in the design to allow any necessary corrections to be made to the ion and electron trajectories. In the construction care was taken to ensure the stability and precision of the structure and in particular to preserve a constant geometry and uniform field over the entire length of the device.

The angular resolution of the system is limited by the spacing of the scintillator elements. In the present device there are 45 elements, 2 mm in diameter spaced at 5 mm between centres over a 250 mm length, equivalent to an angular resolution in the molecular beam apparatus of 0.1°. (This scale follows from the requirements for time-of-flight resolution.)

The majority of secondary electrons produced at the Al_2O_3 surface have very small initial energies (~2.5 eV) and

are emitted dominantly normal to the surface (Curran 1953). Taking the worst case of electrons with 2 eV energy given off parallel to the surface, and an accelerating voltage of 50 kV, the deflection of the electrons at the scintillator will be 3 mm. Only electrons given off parallel to the line of scintillators will affect the angular resolution and the effect will be negligible.

3.2. Optical system

The requirement in designing the optical coupling components was to collect the maximum fraction of the photons formed in the scintillator as a result of each electron burst. It was also convenient for them to function as a vacuum barrier. The collected photons are then divided into two parts and routed with minimum loss to two different photomultipliers. The photomultiplier tubes were of the fast linear focused type, EMI 9826B, with a 19 mm diameter bialkali photocathode, and had a rise time of ~ 2 ns.

The scintillator design finally adopted is shown in figure 2. Each element in the array is constructed from a 10 mm length of 2 mm diameter NE102A plastic scintillator rod. One end is cut and polished perpendicular to the axis of the rod and mates with a fibre-optic termination. The other end is carefully shaped to a 60° full angle cone, chosen so as to maximise reflection into the (rather narrow) acceptance cone of the optical fibre. The sides of each element were thinly coated with white reflective paint. The completed element was then glued, using an epoxy resin, into the stainless steel mounting plate using the small chamfer in the plate around each element to 'puddle' the resin and ensure a vacuum-tight seal. The protruding conical ends of the scintillator were finally aluminised by vacuum sputtering to improve reflectivity and provide electrical grounding.

In our initial work commercially available **Y** optical fibre bundles were used to join each scintillator element to its two photomultipliers. However, it was found that substantial differences in sensitivity across the front face of the multiplier produced unacceptable variations in the sensitivity of the individual angle detection elements. Accordingly in the final instrument a special harness was constructed (Eurotec Optical Fibres Ltd), having the same logic connections, but in which the fibres from individual scintillator elements were randomly mixed across the surface of the photocathode.

3.3. Electronics

The coincidence and decoding interface was built using fast MECL logic to perform the following functions:

(i) A coincidence event, CE, in photomultipliers M and N, signalling an arrival in angle element i, is detected logically as:

$$\text{CE} = MN\overline{(O+P+Q+R)}\,\overline{(S+T+U+V+\text{Hold})} \qquad (7)$$

where M, N, O, P, etc are the logical signals developed from the separate photomultipliers and 'Hold' is an external logic signal for experimental control purposes. As can be seen from (7) coincidence events are *not* accepted and decoded if more than two photomultiplier signals are asserted simultaneously (as can happen randomly, especially at very high signal rates). In this situation confusion would exist as to the angular location of the event. The width in the coincidence window is determined by adjustment of the pulse width from the photomultiplier discriminators (typically 10 ns).

(ii) A detected event, CE, is used to generated a time signal by stopping a 100 MHz clock. This clock is synchronised either to an external logic signal, e.g. for time-of-flight experiments, or may be triggered by a prior event from another experimental parameter. This facility will allow photon/scattered-particle coincidence experiments to be performed.

(iii) The event, MN, is also decoded to determine the angular location i of the signal, this position then being encoded as a parallel 6 bit address.

(iv) The arrival time (eight bits), scattered angle (six bits), and two further bits coding other experimental information are finally output to a further device – at present rather slowly to a microcomputer. A dedicated buffer store is being developed for more rapid processing.

(v) During the operations (ii)–(iv) a 'busy' signal is generated. Any coincidence events arriving in this period are counted separately in an overflow channel but are not further processed. Events arriving during the 40 ns long detection period of a previous ion are not recorded in any way. The data rates in any experiment must thus be suitably adjusted, by observation of the overflow count rate, to ensure unbiased sampling. The interface is shown schematically in figure 4.

The maximum data rate through the interface is determined by the coincidence resolution time τ ($\simeq$10 ns) and the

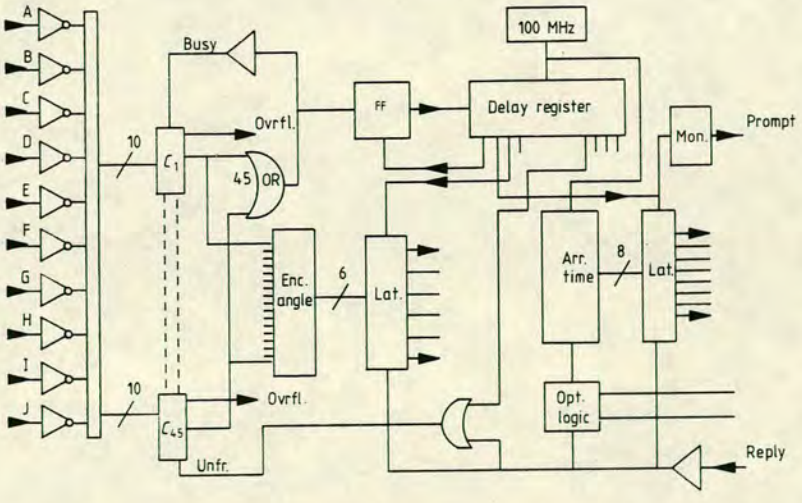

Figure 4. Schematic of the decoding/encoding electronic interface. The coincidence detectors C_1–C_{45}, the six-bit angle encoder and eight-bit arrival time scaler are shown. The delay register controls the sequence of operations in the interface.

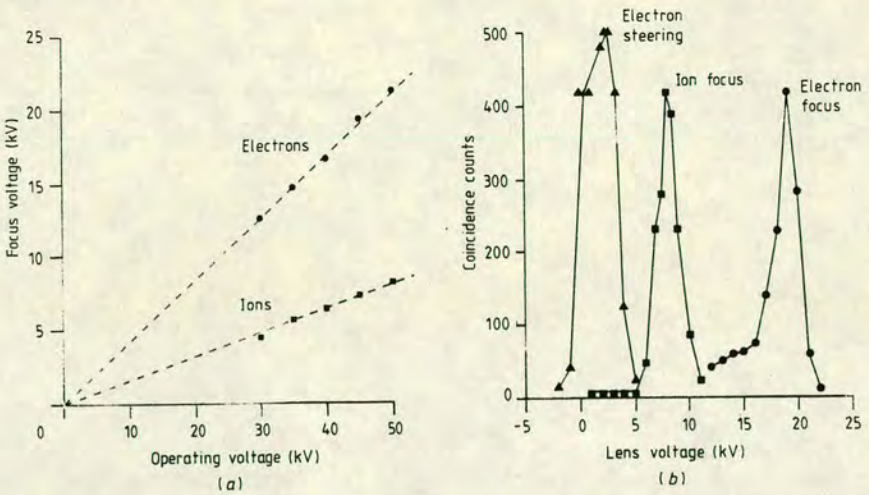

Figure 5. Ion and electron focusing characteristics. (*a*) The optimum focusing voltages for the electron focusing plate and the ion gun (centre electrode of gun). (*b*) The final observed number of counts per second are plotted against the voltage applied to the ion gun and electron focusing plates showing the sharpness of focus achieved. The effect of varying the voltage difference on the split electron steering plate is also shown.

dead time in the decoding interface, following receipt of a coincidence signal, τ_i (40 ns). The *maximum* rate, at 5% dead time, will be:

$$S_{max} \simeq 0.05(\tau + \tau_1)^{-1}\ \text{Hz} = 10^7\ \text{Hz}. \qquad (8)$$

In practice the average rate of collection will be determined by the service time of the computer connected to the coincidence interface. This will set a *much* lower average arrival rate.

4. Performance

The performance of the device was investigated using various test sources (Campbell 1985). These comprised a fast collimated neutral alkali-metal beam source, an alkali ion emitter designed to produce a uniform angular distribution of M^+ ions across the entire detector and a fast collimated He^+ ion beam. The fast neutral atom source was rather inconvenient in operation and since the surface ionisation process is rather well investigated (McCall and Fluendy 1978, Fluendy *et al* 1979) for most purposes the ion sources were employed.

4.1. Electron and ion optics

The electrostatic focusing properties were confirmed using the test sources. The observed coincidence rate in the angular channels was then optimised with respect to the focusing voltages. The focusing conditions for the ion test source are shown in figure 5. As expected the optimum focus voltages increase linearly with operating voltage. The sharpness of the focus obtained is illustrated in figure 5(*b*). With the atom test source it was found that the focusing conditions were sharper since the neutrals are ionised in a localised region in the injection gun.

Experiments with a variable deflection voltage between the Al_2O_3 surface and the scintillators (electron steering voltage) showed the expected behaviour (figure 5(*b*)) and indicated that the electron image was of sufficient size that small differences in the geometry of these elements would not strongly affect the sensitivity.

The effectiveness of this aspect of the design was also checked by inserting a plane sheet of plastic scintillator in place of the separate elements and their fibre-optic couplings. Modest atom/ion fluxes into the detector produced sufficient fluorescence to be seen by the naked eye. The focusing conditions could then be observed directly.

It was also possible to confirm the angular resolution in the same way by inserting a slotted mask in the ion gun. Observations by the naked eye of a 2 mm wide slot showed no apparent loss of resolution in the electron image as revealed by the initial fluorescence. More quantitative measurements using photomultipliers coupled to the scintillator plate by 2 mm diameter fibres spaced 4 mm apart showed some cross talk, as can be seen in figure 6. This was almost entirely due to the thickness of the scintillator plate which allowed some fluorescence emission from below one fibre, emitted through 2π sr, to enter an adjacent fibre. This effect is, of course, eliminated in the discrete element design used in the actual detector.

4.2. Sensitivity

The secondary electron gain arising from ion impact on the Al_2O_3 surface was measured by comparing a measured ion

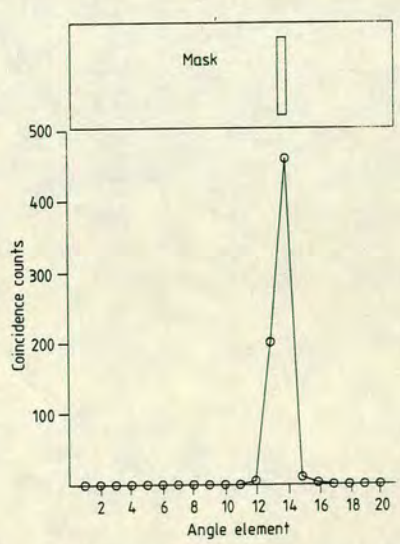

Figure 6. Signal rate plotted against fibre-optic angle number for a slit masked signal.

flux input with the current collected on a plate temporarily mounted in place of the scintillator elements. A current gain of 10 -11 was observed.

The overall sensitivity was checked in two ways, most directly by comparing current measurements of the input ion flux from a collimated beam with the coincident count rate under the same conditions. These measurements were somewhat inconvenient due to the low ion currents involved.

Alternatively measurement of the ratio, R, between the normal coincidence derived count rate, P_2, at any angle and the *non-coincidence* count rate, P_1, under the same conditions also yielded the sensitivity. Since from equation (6):

$$R = P_2/P_1 = 1 - (1 - \varepsilon d)^{\eta\varepsilon} \tag{9}$$

Hence

$$P_2 = K P_1 \tag{10}$$

Comparison of the two methods showed satisfactory agreement and the second method was normally employed.

Measurements performed in this way on the final system are shown as a function of the device operating voltage in figure 3. A number of similar measurements performed at different stages during the detector's development are also plotted. The improvements in sensitivity seen arose entirely from changes in the photon collection efficiency. The initial measurements, of lowest sensitivity, were made using a plane scintillator sheet and a locally constructed and polished optical fibre harness. Subsequent improvements corresponded to the use of commerical **Y** optical fibre connectors; the use of discrete, shaped, scintillator elements and finally the installation of the commercially fabricated harness. It can be seen that the desired operating region on the 'plateau' can be established at voltages greater than ~53 kV.

Measurements of the efficiency were repeated for a number of different angle elements. For scintillators using the same photomultipliers the sensitivities were approximately randomly distributed with a standard deviation of ~4% at 50 kV operating voltage. More significant differences, however, were apparent between different photomultiplier tubes and some selection/rejection of PM tubes was required to obtain an approximately balanced performance.

The remaining differences in sensitivity were finally compensated by a calibration operation. In this process an ion flux, uniform in intensity at all angles was input to the detector and appropriate correction factors deduced.

4.3. Stability

Repeated measurements of the correction factors over a long period of time again showed a random variation but with a rather larger standard deviation, 8%, than was seen without the spread in photomultiplier performance. It is probable that further improvements in stability could be obtained by more careful selection of the PM tubes and this is in hand. The stability of the device was further explored by measuring the autocorrelation functions for the correction factors. This was calculated from the expression:

$$\text{Autocorrelation (at time } k) = \frac{\sum_{i=1}^{i=N-k} (C_i - \bar{C})(C_{i+k} - \bar{C})}{\sum_{i=1}^{i=N} (C_i - \bar{C})^2}$$

where the correction factors $C_1, \ldots C_i, \ldots C_N$, were measured at regular intervals during an experimental run of three days duration. From the results in figure 7 it can be seen that the major drift mechanisms have a period of a few hours or less. The considerable improvement produced by higher operating voltages which push the sensitivity further into the saturation region can also be seen.

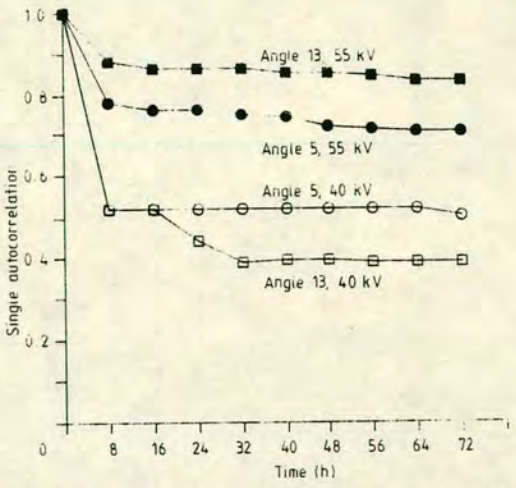

Figure 7. Autocorrelation function for the sensitivity showing the improved performance at high voltages.

5. Conclusion

The device described offers a useful alternative to detectors using channel plates. It is particularly advantageous when high speed (<10 ns) operation is required and where the geometry is extended or requires to be particularly tailored to the needs to the application.

Acknowledgment

Support from the Paul Fund of the Royal Society is gratefully acknowledged.

References

Campbell E E B 1985
PhD thesis University of Edinburgh

Curran S C 1953 *Luminescence and the Scintillation Counter* (London: Butterworths)

Daley N R 1960 Scintillation type mass spectrometer ion detector
Rev. Sci. Instrum. **31** 264–7

Fluendy M A D, Lawley K P, McCall J, Sholeen C and Sutton D 1979 Electronic excitation in potentially reactive atom–molecule collisions
Faraday Disc. Chem. Soc. **67** 41–56

Harting E and Read F H 1976 *Electrostatic Lenses* (Amsterdam: Elsevier)

Hasted J B 1964 *Physics of Atomic Collisions* (London: Butterworths)

McCall J M and Fluendy M A D 1978 Signal enhancement by velocity modulation in time of flight analysis of atomic and molecular beam scattering
J. Phys. E: Sci. Instrum. **11** 631–4

Pierce J R 1940 Rectilinear electron flow in beams
J. Appl. Phys. **11** 548–54